Examining the Relationship Between Lignocellulosic Biomass Structural Constituents and Its Flow Behavior

A Dissertation Presented for the

Doctor of Philosophy

Degree

The University of Tennessee, Knoxville

Ekramul Haque Ehite

August 2023

DEDICATION

To my dearly departed mother.

ACKNOWLEDGEMENTS

I want to thank my advisor, Dr. Nourredine Abdoulmoumine, for his invaluable leadership, support, and advice throughout my doctoral journey. Dr. Nour showed me the utmost empathy and kindness and guided me in developing as a researcher, academic, and individual.

I would also like to thank Drs. Julie Carrier, Hao Gan, Oluwafemi Oyedeji, and Hamparsum Bozdogan for being part of my dissertation committee and providing their guidance. Special thanks to Dr. Oluwafemi Oyedeji for conducting additional analysis at the Oak Ridge National Laboratory. My colleagues at the BEAM Lab – Ross Houston, Skye Li, and Conner Pope have been a great source of support, and I am grateful for their encouragement throughout. Finally, my sincere thanks go out to Scott Tucker, David Smith, Sandy Marine, and Sarah Mobley for their help in designing, constructing, and operating experimental systems necessary to conduct my research.

My late mother, Hosna Ara Begum Rina, has been a beacon in my life, pointing me toward the correct path. The morals and values she instilled in me made me the man I am today. Since her untimely demise, my two aunts, Mili and Nilu, have acted as my surrogate mothers and supported me throughout. Thank you, my dear *Khalas*!

I will never find enough words to show gratitude to my siblings, Emon and Era, and their partners, Sandra and Mamun, for their limitless encouragement. I am thankful to all my family and friends, both near and far, who have supported me in finishing this project.

Thanks to the Foundation for Food and Agriculture Research for selecting me as one of the 2020-2023 FFAR Professional Development Fellows, contributing immensely to my professional growth. Thank you to the American Society of Agricultural and Biological Engineering (ASABE) community, especially my Young Professionals Community (YPC) peers, and all my Alpha Kappa Psi Professional Business Fraternity brothers for their support. My sincere love and gratitude go to the Myers siblings – Payton and Justin, and their wonderful parents Drs. Linda and James Myers for helping me through a most challenging time. I am grateful to Alice Daer and Michele Eodice from Quick Brown Fox Consulting for their valuable writing advice. Finally, my friends David Phelps, Emily Robinson, Maria Baker, and Savannah Fries – this journey would be a lot less fun if you were not around!

I want to thank my former advisors and mentors, the late Drs Eric Drumm and Stuart Law, who unfortunately left the mortal plain during my doctoral studies. Similarly, my young aerospace engineer friend Serena Wednesday Smith left us too early. I miss you all and will be forever grateful for your support.

Music has always been a big inspiration for me, personally and academically. I want to thank my musical heroes Michael Schenker, Robin McAuley, Steve Mann, Bodo Schopf, Rocky Newton, Al Stewart, Derek William Dick (Fish), Jason Bieler, and all members of the band Iron Maiden (especially Bruce Dickinson and Steve Harris) for motivating me throughout the years.

During the hundreds of hours during the experiments and writing of my dissertation, I was inspired by listening to the dulcet voices of podcast hosts such as Big Gross Movies (Dave Atkinson and Meg Mackay), Talk from Superheroes (Andrew Ivimey and Diana McCallum), The Villain Was Right (Craig Fay and Rebecca Reeds), and I Hate It but I Love It (Kat Angus and Jocelyn Geddie). Thank you, my friends!

I will always be grateful to the University of Tennessee community for welcoming me with open arms. Knoxville will always be home sweet home to me. Rest assured, I am a Vol for Life and will carry the Volunteer Creed forever.

Go Vols!

ABSTRACT

Lignocellulosic biomass material sourced from plants and herbaceous sources is a promising substrate of inexpensive, abundant, and potentially carbon-neutral energy. One of the leading limitations of using lignocellulosic biomass as a feedstock for bioenergy products is the flow issues encountered during biomass conveyance in biorefineries. In the biorefining process, the biomass feedstock undergoes flow through a variety of conveyance systems. The inherent variability of the feedstock materials, as evidenced by their complex microstructural composition and non-uniform morphology, coupled with the varying flow conditions in the conveyance systems, gives rise to flow issues such as bridging, ratholing, and clogging. These issues slow down the conveyance process, affect machine life, and potentially lead to partial or even complete shutdown of the biorefinery. Hence, we need to improve our fundamental understanding of biomass feedstock flow physics and mechanics to address the flow issues and improve biorefinery economics.

This dissertation research examines the fundamental relationship between structural constituents of diverse lignocellulosic biomass materials, i.e., cellulose, hemicellulose, and lignin, their morphology, and the impact of the structural composition and morphology on their flow behavior.

First, we prepared and characterized biomass feedstocks of different chemical compositions and morphologies. Then, we conducted our fundamental investigation experimentally, through physical flow characterization tests, and computationally through high-fidelity discrete element modeling. Finally, we statistically analyzed the relative influence of the properties of lignocellulosic biomass assemblies on flow behavior to determine the most critical properties and the optimum values of flow parameters. Our research provides an experimental and computational framework to generalize findings to a wider portfolio of biomass materials. It will help the bioenergy community to design more efficient biorefining machinery and equipment, reduce the risk of failure, and improve the overall commercial viability of the bioenergy industry.

KEYWORDS: Lignocellulosic biomass, flow mechanics, shear strength, angle of repose, discrete element modeling.

PREFACE

The majority of the work presented in this dissertation was conducted by the author, including the design and implementation of the research, the analysis of the results, and the writing of the manuscript.

TABLE OF CONTENTS

LIST OF TABLES

LIST OF FIGURES

CHAPTER 1.

INTRODUCTION

1.1. Introduction and Problem Statement

The rise in the global population and associated energy demand, exacerbation of the climate change crisis, decreasing reserves of fossil fuel sources, and socio-political concerns about the existing inequities in the fossil fuel markets have increased the need for clean, sustainable, and renewable energy [1-3]. Among renewable energy sources, plant biomass material, also commonly known as lignocellulosic biomass material, has emerged as a promising substrate of natural, inexpensive, potentially carbon-neutral energy. Sources of lignocellulosic biomass include agricultural and forestry residues, dedicated energy crops, and biowaste products [4]. Since lignocellulosic biomass comes from non-edible sources, they do not compete with human and animal food [5, 6]. Additionally, certain bioenergy crops can be potentially grown in marginal lands without competing with croplands, which is especially relevant for countries with limited land and forest resources [7, 8]. Thus, lignocellulosic biomass materials act as sources of bioenergy and fuel without affecting the global food-energy nexus [9].

The key to expanding bioenergy usage and making it more commercially viable involves addressing the major cost drivers affecting the overall bioenergy economics. The conversion of lignocellulosic biomass into bioenergy, biofuel, and biochemical products occurs in a biorefinery [10, 11]. The biorefinery separates the biomass feedstock using necessary technologies into different chemical compounds, recovers the inherent energy, and generates value-added products [12, 13]. A unique challenge of lignocellulosic biomass materials used in the biorefinery industry is its inherent variability [14]. Biomass feedstock varies in composition due to seasonal, chemical, species, and spatiotemporal conditions, making the design and construction of biorefinery equipment for handling such materials difficult [15]. The highly non-uniform biomass feedstock poses challenges both in upstream processes like feedstock collection, handling, and preprocessing and downstream processes like the thermochemical conversion processes (i.e., pyrolysis, gasification, combustion) [16, 17]. For example, during the feedstock handling and preprocessing stage, the biomass material passes through a number of conveyance systems, such as hopper conveyor, screw-feed conveyor, screener-feeder conveyor, and vibratory conveyor [18]. The feedstock material experiences flow issues unique to each conveyor, such as bridging and ratholing in hopper conveyors and material clogging in screw-feed conveyors [19-21]. The feedstock flow issues in the conveyor systems have highly detrimental effects on biorefinery economics [10, 22]. They slow down the conveyance and conversion process, affect machine life, and potentially lead to partial or even complete shutdown of the biorefinery [23, 24]. Hence, we need to improve our fundamental understanding of biomass feedstock flow physics and mechanics to design more efficient machinery and equipment, reduce the risk of failure and shutdowns, and improve the overall commercial viability of the global biorefinery industry.

Specifically, we need to understand the impacts of biomass cell wall structure on its bulk flow behavior to address the fundamental flow issues. The lignocellulosic biomass cell wall has a compound, non-uniform, three-dimensional matrix structure comprising three polymers: cellulose and hemicellulose, both polysaccharides, and lignin, a phenolic polymer, with trace amounts of other organic and inorganic constituents [14, 25-27]. The relative composition of biomass constitutive polymers varies between species, harvest locations, and conditions and affects such materials' handling, processing, and conversion [28]. The fundamental relation between the structural composition of the lignocellulosic biomass cell wall and the different macro and micro-scale mechanical behaviors of the biomass feedstock is an area of great interest. However, limited fundamental knowledge is available at the moment [29-31]. Understanding the relationship between structural composition and specific mechanical behaviors, such as frictional behavior under different flow conditions, is essential for favorably enhancing said behaviors [32, 33].

To investigate the structural composition-mechanical behavior relationship, we must account for the granular nature of lignocellulosic biomass particle systems. Granular systems comprise a group of macroscopic particles undergoing numerous microscopic interactions, and system properties at both the particle-scale and bulk-scale depend upon the contacting and non-contacting forces between the particles [34, 35]. Prior research shows that physical and chemical properties at the bulk-scale and particle-scale of granular particulate feedstocks have an outsized influence on their flow behavior in a variety of flow conditions [24, 36, 37]. Accurate analysis and measurement of the system properties are essential for predicting the granular flow and development of handling, feeding, and processing systems [19, 38].

While granular particulate systems can be analyzed either experimentally or computationally, a robust analysis process requires a synergistic balance between experimental and computational approaches. Bulk-scale experimental analyses of granular materials in a laboratory environment can be expensive and impractical for particle-scale investigations because even small particle assemblies easily contain tens of thousands of particles [39, 40]. On the other hand, the application of computational techniques, such as discrete element modeling (DEM), for lignocellulosic biomass is complicated by the non-uniform morphological, material, and mechanical properties of biomass feedstock [16, 41]. The computational model needs to capture the inherently variable biomass properties, simulate the physical flow process using the available computing power, and generate simulation outputs that can be validated with results obtained from physical experiments.

This dissertation project aims to provide a rational approach combining experimental techniques and computational modeling to investigate the relationship between lignocellulosic biomass structural constituents, morphology, and flow behavior. Our approach involves the characterization of lignocellulosic biomass particulates of different structures and morphologies, conducting physical flow tests to determine macroscale flow parameters, and generating computational models that could provide further insights into their microscale flow behavior. The proposed experimental and computational framework allows for examining different biomass feedstock, predicting and addressing flow issues, and developing next-generation conveyance systems.

1.2. Research Objectives

The overall target of this dissertation research is to develop a fundamental understanding of the relationship between structural constituents of lignocellulosic biomass, i.e., cellulose, hemicellulose, and lignin, their, morphology, and the impact of the structure and morphology on their flow behavior. We strive to Investigate experimentally with biomass particles of different structural compositions, followed by classical physical flow characterization tests, and computationally, through high-fidelity discrete element modeling.

We organized the project around the following specific objectives:

Objective 1: To experimentally examine and establish the relationship between lignocellulosic biomass structural components, morphology, and their macro-scale flow behavior.

We hypothesize that the lignocellulosic biomass materials of different structural compositions and morphologies will have significantly different frictional and shear strength characteristics. The central research question we seek to answer in this objective is: How can we relate the variation of structural constituent contents and morphologies between and within lignocellulosic biomass materials with variations in their flow behavior?

To prove the hypothesis and answer the central question, we conduct three different case studies to quantify the effects of different lignocellulosic biomass structural constituents on the frictional parameters and shear strength of herbaceous, softwood, and hardwood feedstocks through a series of standardized tests.

For the first case, we examine the relationship between lignocellulosic biomass materials, namely switchgrass, hybrid poplar, and loblolly pine, with different proportions of principal structural constituents, namely cellulose, hemicellulose, and lignin, and their frictional parameters and shear strength characteristics.

For the second case, we investigate the relationship between the structural compositions of biomass materials of varying cellulosic content but collected from a single source, namely hybrid poplar, and their frictional parameters and shear strength characteristics.

Finally, the third case explores the relationship between lignocellulosic biomass materials, namely switchgrass, hybrid poplar, and loblolly pine, of different particle sizes and their frictional parameters and shear strength.

Objective 2: To computationally generate particle assemblies capturing real biomass morphology and examine their macro-scale flow behavior and micro-scale interactions.

We hypothesize that if we can experimentally determine the necessary particle parameters and combine them with superquadric particle assumptions, we can reasonably represent real particle morphology and model lignocellulosic biomass flow comparable with complex particle approximation. The research question we seek to answer in this objective is: How can we realistically capture the highly variable morphological characteristics of lignocellulosic biomass materials and generate computational models for examining their flow behavior at the macro and micro scale?

To prove the hypothesis and answer the central question, we experimentally determine the appropriate morphological, material, and mechanical properties of switchgrass, loblolly pine, and hybrid poplar feedstock. Then, we develop high-fidelity computational models with suitable particle shapes and size distribution to represent the biomass particle assemblies. Finally, we examine the flow behavior of particle assemblies at both the macro scale and micro scale during an angle of repose test and validate the macro-scale output with experimental measurements.

Objective 3: To evaluate the influence of lignocellulosic biomass assembly's morphological, material, and mechanical properties on their macro-scale flow behavior.

We hypothesize that we can reduce the number of experiments required for the statistical analysis, then use classical and modern model selection criteria to develop simpler models to represent the relation between the flow behavior and biomass properties. The research question we seek to answer in this objective is: How to determine the relative influence of critical biomass properties on flow behavior and develop statistically efficient models to capture their relationship?

To prove the hypothesis and answer the research question, we initially developed a computational simulation plan following a design of experiments

(DoE) principle for the angle of repose discrete element computational model. We then conduct a multiple linear regression to identify the most critical input parameters and interactions. We then conduct an optimization process to determine the optimum value for the angle of repose using the regression model and examine the accuracy and quality of the fitted model using classical and modern statistical analysis criteria.

1.3. Organization of the Dissertation

This dissertation includes the captions adapted for mathematical equations in parentheses, e.g. (1.1). We prefixed the mathematical equations with the chapter number, a dot, and the equation and reaction number in descending order of appearance in the chapter. An illustration of this notation is shown below for the relationship between the shear strength (τ), normal stress (σ), and the coefficient of friction (μ) by Equation 1.1.

$$\tau = C + \mu\sigma, \tag{1.1}$$

We used the American Psychological Association (APA), 6th Edition style guide for in-text citations and bibliographies. Organizationally, we divided this dissertation into six chapters.

Chapter 1 presents a brief introduction to the dissertation project with an overview of the research background, the overall research problem, the research objectives, questions, hypotheses, and the rationale for the proposed research plan. This chapter acts as a quick overview of the document for readers.

Chapter 2 comprehensively reviews previous research on various aspects of lignocellulosic biomass flow in biorefineries. Initially, we detail the state-of-the-art global energy sector and lignocellulosic biomass energy's current and future role. We follow this section by discussing lignocellulosic biomass structural composition and its effect on biomass particulates' flow behavior. Then, we discuss biomass processing in biorefineries and the mechanics and economics of biomass flow issues. We then review the past works on flow analysis techniques for lignocellulosic biomass materials. Finally, we comprehensively overview experimental and computational approaches for analyzing biomass flow.

Chapter 3 captures all activities related to Objective 1 and focuses on the experimental investigation of the role of lignocellulosic biomass structural constituents, namely cellulose, hemicellulose, and lignin on lignocellulosic biomass particulates' flow behavior. The chapter initially shows a case study for relating the proportion of cellulose, hemicellulose, and lignin to the frictional parameters and shear strength characteristics for biomass materials sourced from different feedstocks. The second case study relates the structural compositions of biomass materials from a single source with their frictional parameters and shear strength characteristics. The third study shows the relationship between biomass materials of varied sizes sourced from different feedstocks and their frictional parameters and shear strength characteristics. Finally, we summarize our findings from these case studies in the conclusions section.

Chapter 4 captures all activities related to Objective 2 and presents a framework for capturing lignocellulosic biomass morphology and flow behavior by combining experimental morphological parameter measurement and discrete element computational modeling (DEM). The chapter initially describes the material selection and characterization techniques used to quantify physio-mechanical properties. Then we present the quasi-three-dimensional imaging, image processing, and error minimization used for capturing the morphology of the lignocellulosic particles with a high degree of accuracy. Next, we show the process for generating the superquadric particulate assemblies in the DEM environment to recreate the hollow cylinder angle of repose study. Afterward, we present the outputs from DEM computational models, validate them using experimental outcomes, and explore the microscale behavior using the computational model. Finally, we provide research conclusions based on our experimental and computational analysis.

Chapter 5 describes the evaluation of the relative influence of morphological, material, and mechanical properties of lignocellulosic biomass assembly properties on their macro-scale flow behavior. The chapter initially describes the design of simulations (DoS) process for producing a matrix of DEM simulations for the switchgrass particles by varying selected DEM input parameters and determining the angle of repose for each simulation case study. Then, we present a classical multiple linear regression model to describe the relationship between the response and predictor variables. We follow this step with a factorial analysis to determine the most influential input parameters and their interactions and generate a reduced model. Then, we provide a process optimization technique to determine the lowest value for the angle of repose from the reduced model. Next, we examine the suitability of the reduced model by conducting a residuals analysis, scoring the information criteria for the dataset. Finally, we summarize our findings in the conclusions section.

Finally, chapter 6 details the overall conclusions made from the previous chapters' results, summarizes the contributions made to the field, and makes recommendations for future researchers to continue the contributions made by this work.

References

(1) Datta, A.; Hossain, A.; Roy, S. An overview on biofuels and their advantages and disadvantages. *Asian J. Chem.* **2019**, *31* (8), 1851-1858.

(2) Savvanidou, E.; Zervas, E.; Tsagarakis, K. P. Public acceptance of biofuels. *Energy Policy* **2010**, *38* (7), 3482-3488.

(3) Vassilev, S. V.; Vassileva, C. G.; Vassilev, V. S. Advantages and disadvantages of composition and properties of biomass in comparison with coal: An overview. *Fuel* **2015**, *158*, 330-350.

(4) Rulli, M. C.; Bellomi, D.; Cazzoli, A.; De Carolis, G.; D'Odorico, P. The water-land-food nexus of first-generation biofuels. *Sci. Rep.* **2016**, *6* (1), 1-10.

(5) Carpenter, D.; Westover, T. L.; Czernik, S.; Jablonski, W. Biomass feedstocks for renewable fuel production: a review of the impacts of feedstock and pretreatment on the yield and product distribution of fast pyrolysis bio-oils and vapors. *Green Chem.* **2014**, *16* (2), 384-406.

(6) Havlík, P.; Schneider, U. A.; Schmid, E.; Böttcher, H.; Fritz, S.; Skalský, R.; Aoki, K.; De Cara, S.; Kindermann, G.; Kraxner, F. Global land-use implications of first and second generation biofuel targets. *Energy Policy* **2011**, *39* (10), 5690-5702.

(7) Gopalakrishnan, G.; Cristina Negri, M.; Snyder, S. W. A novel framework to classify marginal land for sustainable biomass feedstock production. *J. Environ. Qual.* **2011**, *40* (5), 1593-1600.

(8) Tang, Y.; Xie, J. S.; Geng, S. Marginal land-based biomass energy production in China. *J. Integr. Plant Biol.* **2010**, *52* (1), 112-121.

(9) Antizar-Ladislao, B.; Turrion-Gomez, J. L. Second-generation biofuels and local bioenergy systems. *Biofuels, Bioprod. Bioref.* **2008**, *2* (5), 455-469.

(10) Amidon, T. E.; Wood, C. D.; Shupe, A. M.; Wang, Y.; Graves, M.; Liu, S. Biorefinery: conversion of woody biomass to chemicals, energy and materials. *J Biobased Mater Bioenergy* **2008**, *2* (2), 100-120.

(11) Kamm, B.; Kamm, M. Biorefinery-systems. *Chem. Biochem. Eng. Q.* **2004**, *18* (1), 1-7.

(12) Octave, S.; Thomas, D. Biorefinery: Toward an industrial metabolism. *Biochimie* **2009**, *91* (6), 659-664.

(13) Taylor, G. Biofuels and the biorefinery concept. *Energy Policy* **2008**, *36* (12), 4406-4409.

(14) Yan, J.; Oyedeji, O.; Leal, J. H.; Donohoe, B. S.; Semelsberger, T. A.; Li, C.; Hoover, A. N.; Webb, E.; Bose, E.; Zeng, Y. Characterizing variability in lignocellulosic biomass-A review. *ACS Sustain. Chem. Eng.* **2020**, *8* (22), 8059–8085. DOI: https://doi.org/10.1021/acssuschemeng.9b06263.

(15) Oyedeji, O.; Gitman, P.; Qu, J.; Webb, E. Understanding the Impact of Lignocellulosic Biomass Variability on the Size Reduction Process: A Review. *ACS Sustain. Chem. Eng.* **2020**, *8* (6), 2327-2343. DOI: https://doi.org/10.1021/acssuschemeng.9b06698.
(16) Williams, C. L.; Westover, T. L.; Emerson, R. M.; Tumuluru, J. S.; Li, C. Sources of biomass feedstock variability and the potential impact on biofuels production. *Bioenergy Res.* **2016**, *9* (1), 1-14.
(17) Liu, L.; Ye, X. P.; Womac, A. R.; Sokhansanj, S. Variability of biomass chemical composition and rapid analysis using FT-NIR techniques. *Carbohydr. Polym.* **2010**, *81* (4), 820-829.
(18) Hess, J. R.; Wright, C. T.; Kenney, K. L. Cellulosic biomass feedstocks and logistics for ethanol production. *Biofuels, Bioprod. Bioref.* **2007**, *1* (3), 181-190.
(19) Miao, Z.; Grift, T. E.; Hansen, A. C.; Ting, K. C. Flow performance of ground biomass in a commercial auger. *Powder Technol.* **2014**, *267*, 354-361.
(20) Olanrewaju, T. O. Design and fabrication of a screw conveyor. *Agric. Eng.* **2017**, *19* (3), 156-162.
(21) Prescott, J. K.; Barnum, R. A. On powder flowability. *Pharm. Technol.* **2000**, *24* (10), 60-85.
(22) Rahimi, V.; Shafiei, M. Techno-economic assessment of a biorefinery based on low-impact energy crops: A step towards commercial production of biodiesel, biogas, and heat. *Energy Convers. Manage.* **2019**, *183*, 698-707.
(23) Miao, Z.; Shastri, Y.; Grift, T. E.; Hansen, A. C.; Ting, K. Lignocellulosic biomass feedstock transportation alternatives, logistics, equipment configurations, and modeling. *Biofuel Bioprod Biorefin* **2012**, *6* (3), 351-362.
(24) Rabinovich, E.; Kalman, H.; Peterson, P. F. Granular material flow regime map for planar silos and hoppers. *Powder Technol.* **2021**, *377*, 597-606.
(25) Sun, Y.; Cheng, J. Hydrolysis of lignocellulosic materials for ethanol production: a review. *Bioresour. Technol.* **2002**, *83* (1), 1-11.
(26) Xu, F.; Yu, J.; Tesso, T.; Dowell, F.; Wang, D. Qualitative and quantitative analysis of lignocellulosic biomass using infrared techniques: a mini-review. *Appl. Energy* **2013**, *104*, 801-809.
(27) Yan, W.; Acharjee, T. C.; Coronella, C. J.; Vasquez, V. R. Thermal pretreatment of lignocellulosic biomass. *Environ. Prog. Sustain.* **2009**, *28* (3), 435-440.
(28) Zhang, K.; Johnson, L.; Nelson, R.; Yuan, W.; Pei, Z.; Wang, D. Chemical and elemental composition of big bluestem as affected by ecotype and

planting location along the precipitation gradient of the Great Plains. *Ind. Crops Prod.* **2012**, *40*, 210-218.
(29) Lee, H. V.; Hamid, S. B. A.; Zain, S. K. Conversion of lignocellulosic biomass to nanocellulose: structure and chemical process. *Sci. World J.* **2014**, *2014*.
(30) Xia, Y.; Stickel, J. J.; Jin, W.; Klinger, J. A review of computational models for the flow of milled biomass I: Discrete-particle models. *ACS Sustain. Chem. Eng.* **2020**, *8* (16), 6142–6156. DOI: https://doi.org/10.1021/acssuschemeng.0c00402.
(31) Jin, W.; Stickel, J. J.; Xia, Y.; Klinger, J. A review of computational models for the flow of milled biomass II: Continuum-mechanics models. *ACS Sustain. Chem. Eng.* **2020**, *8* (16), 6157–6172. DOI: https://doi.org/10.1021/acssuschemeng.0c00412.
(32) Oyedeji, O.; Daw, C. S.; Labbe, N.; Ayers, P.; Abdoulmoumine, N. Kinetics of the release of elemental precursors of syngas and syngas contaminants during devolatilization of switchgrass. *Bioresour. Technol.* **2017**, *244*, 525-533. DOI: 10.1016/j.biortech.2017.07.167.
(33) Wang, S.; Dai, G.; Yang, H.; Luo, Z. Lignocellulosic biomass pyrolysis mechanism: a state-of-the-art review. *Prog. Energy Combust. Sci.* **2017**, *62*, 33-86.
(34) Falk, J.; Berry, R. J.; Broström, M.; Larsson, S. H. Mass flow and variability in screw feeding of biomass powders—Relations to particle and bulk properties. *Powder Technol.* **2015**, *276*, 80-88.
(35) Bouchaud, J. P.; Claudin, P.; Levine, D.; Otto, M. Force chain splitting in granular materials: A mechanism for large-scale pseudo-elastic behaviour. *Eur. Phys. J. E Soft Matter* **2001**, *4* (4), 451-457.
(36) Johnstone, M. W. Calibration of DEM models for granular materials using bulk physical tests. Ph.D., The University of Edinburgh, 2010.
(37) Mustoe, G. G. W.; Miyata, M. Material flow analyses of noncircular-shaped granular media using discrete element methods. *J. Eng. Mech.* **2001**, *127* (10), 1017-1026.
(38) Tumuluru, J. S.; Wright, C. T.; Hess, J. R.; Kenney, K. L. A review of biomass densification systems to develop uniform feedstock commodities for bioenergy application. *Biofuel Bioprod Biorefin* **2011**, *5* (6), 683-707.
(39) Ganesan, V.; Rosentrater, K. A.; Muthukumarappan, K. Flowability and handling characteristics of bulk solids and powders–a review with implications for DDGS. *Biosys. Eng.* **2008**, *101* (4), 425-435.
(40) Ogden, C. A.; Ileleji, K. E. Physical characteristics of ground switchgrass related to bulk solids flow. *Powder Technol.* **2021**, *385*, 386-395.

(41) Zhong, W.; Yu, A.; Liu, X.; Tong, Z.; Zhang, H. DEM/CFD-DEM modelling of non-spherical particulate systems: theoretical developments and applications. *Powder Technol.* **2016**, *302*, 108-152.

CHAPTER 2.

LITERATURE REVIEW

Disclaimer: The author previously included partial results of this chapter's work in the article:

Ehite, E.H., and Abdoulmoumine, N. "Woody and herbaceous biomass feedstocks and their physical, chemical, and thermal properties." Under review for publication in the *Handbook of Biorefinery Research and Technology*, 2023. https://doi.org/10.1007/978-94-007-6724-9.

2.1. The Global Energy Scenario

The global consumption of energy has grown steadily since the 20th century due to the ever-increasing population and corresponding industrialization. The global energy supply ramped up from 6098 Mtoe in 1973 to 14282 Mtoe in 2018 to meet this ever-growing energy demand, with 84.3% of that energy coming from fossil fuel sources [1]. The energy consumption in the United States of America constitutes 25% of the global energy consumption, with about 80% of its energy currently derived from fossil fuels, including petroleum, coal, and natural gas [2]. However, the negative impact on global climate by fossil fuels, the ever-dwindling reserve of crude oils and geopolitical factors affecting their supply chain, and socio-political issues related to extraction technologies like hydraulic fracking have made the proper utilization of renewable energy resources to produce fuel and energy a critical issue for the global energy researchers [3, 4].

2.2. Biomass Energy Sources

In the United States, renewable energy sources, including hydropower, wind, solar, biomass, geothermal, and ethanol, supply 11% of the annual domestic energy consumption [2]. Biomass, including wood, biogenic waste, and biofuels, constitutes nearly 43% of the total renewable energy consumed. Biomass-derived energy and products are widely used in industrial, transportation, residential, and commercial sectors [5]. The first generation of biofuels sourced from biomass substrates focused on food crops like corn, grains, soybean, and sugar beets, and the biofuel derived from such sources is termed first-generation biofuels [6]. However, such biofuels have low energy density and high processing costs, making them a poor substitute for fossil fuels [7]. Moreover, food sources for energy production create competition for land and water, negatively influence the price and availability of food, and exacerbate socioeconomic inequalities [8].

Therefore, biomass researchers have concentrated on energy extraction from inedible feedstock materials and termed them second-generation biofuels [9]. Among the second-generation biofuel sources, lignocellulosic biomass material sourced from plants and herbaceous sources has emerged as an inexpensive, renewable, and abundant energy source. Biomass materials contain biopolymers such as cellulose, hemicellulose, and lignin, which can be converted into their monomer sugars by a succession of thermo-chemical and biological processes to produce a variety of bioproducts. Typical sources of lignocellulosic biomass include agricultural residues (e.g., wheat straw, sugarcane bagasse, corn stover), forest products (hardwood and softwood), dedicated energy crops (switchgrass, Salix, sugarcane, corn), or aquatic plants (water hyacinth) [10]. Specifically, dedicated woody energy crops and herbaceous feedstocks are of interest because they are grown specifically for energy production, often on marginal lands unsuitable for food production [11]. These lignocellulosic materials act as substrates of bioenergy and fuel without affecting human or animal food production [12, 13]. Thus, bioproduct extraction from these agrarian sources is a potential solution for disposing of residual materials while reducing pressures on human-animal food security [14].

In 2017, biomass contributed to 45% of the total renewable energy consumption in the United States [5]. In addition to energy, biomass acts as feedstock for producing liquid transportation fuels and chemical products [15]. The US Department of Agriculture (USDA) and the US Department of Energy (DOE) set down a target to obtain 20% of the total fuel used for transportation purposes and 25% of the chemical products from biomass sources by the year

2030 [16]. Additionally, the USDA agricultural innovation agenda (AIA) has a target of increasing the agricultural industry output (food, fiber, fuel, and feed) by 40% while reducing the environmental footprint by 50% by the year 2050 [17]. The efficient utilization of lignocellulosic biomass materials to produce biofuel, energy, and related chemical products aligns directly with USDA's targets of increasing agricultural productivity, enhancing forest management, reducing food loss and waste, and supporting renewable energy feedstocks [18]. Thus, having a robust understanding of lignocellulosic biomass material's structural composition is essential for maximizing its potential as a crucial component of the US energy and agriculture portfolio.

2.3. Lignocellulosic Biomass Composition

The lignocellulosic biomass cell wall has an anisotropic, three-dimensional matrix structure comprising cellulose, hemicellulose, lignin, and trace amounts of other chemical compounds.

Cellulose is a glucose polymer consisting of linear chains of (1,4)-D-glucopyranose units arranged in a microcrystalline structure and is difficult to dissolve or hydrolyze under natural conditions. The degree of polymerization (DP) for the cellulose chains ranges from 500-25,000 [19, 20]. The agglomeration of cellulose chains by Hydrogen and Van Der Waals bond generates microfibrils, and they bundle together to form cellulose fibers. These fibers provide the biomass matrix its mechanical strength and chemical stability [21, 22]. Cellulose acts as the major constituent of the plant cell wall [23].

Hemicellulose is a heteropolysaccharide. i.e., a mixture of different polysaccharides, and comprises a variety of hexoses (mannose, glucose, galactose), pentoses (xylose, arabinose), and gluconic acids. Xylan is the most predominant hemicellulose for herbaceous and hardwood biomass, and glucomannan is predominant in softwood [22]. Hemicellulose is more readily soluble, and the degree of polymerization for the hemicellulose branches ranges from 100-200 [24, 25]. Hemicellulose links the cellulose fibers and lignin, providing biomass structure rigidity [26, 27].

Lignin is a three-dimensional, highly cross-linked phenolic polymer consisting of phenylpropanoid substrates such as p-hydroxyphenyl (H-type), guaiacyl (G-type), and syringyl (S-type) units [28, 29]. Lignin has an amorphous structure with two parts: the aromatic part and the C3 chain part. Only the OH group is a usable reaction site for the phenolic and alcoholic hydroxyl groups. There are no chains with repeating subunits like cellulose and hemicellulose [30]. As such, the enzymatic hydrolysis of lignin is extremely difficult. Lignin provides structural support to the lignocellulose matrix by filling the space between cellulose and hemicellulose (thus often called a 'glue') and resists microbial intrusions and oxidative stress [31, 32].

The relative proportion of these major constituents varies between species, i.e., herbaceous, woody, and agricultural residues and types, e.g., hardwood and softwood [33]. For example, hardwoods like maple, elm, and poplar typically have a lower cellulose content (38-49%) than softwoods like pine, cedar, and fir (40–45%) but a higher lignin content (hardwood: 26-34%, softwood: 23-30%) [34, 35]. Generally, the proportion of cellulose, hemicellulose, and lignin in the biomass by weight can be 40–60%, 15–30%, and 10–25%, respectively [36].

In addition to the main polymer constituents, the biomass structures contain additional compounds called extractives or volatiles. Extractives consist of water-soluble modules, such as sucrose or amylose, or alcohol-soluble modules, like chlorophyll and waxes. Finally, the biomass structure may include secondary components like alkaloids, resins, triglycerides, pigments, or terpenes [37].

Figure 2.1 shows a detailed view of the structural composition of lignocellulosic biomass materials.

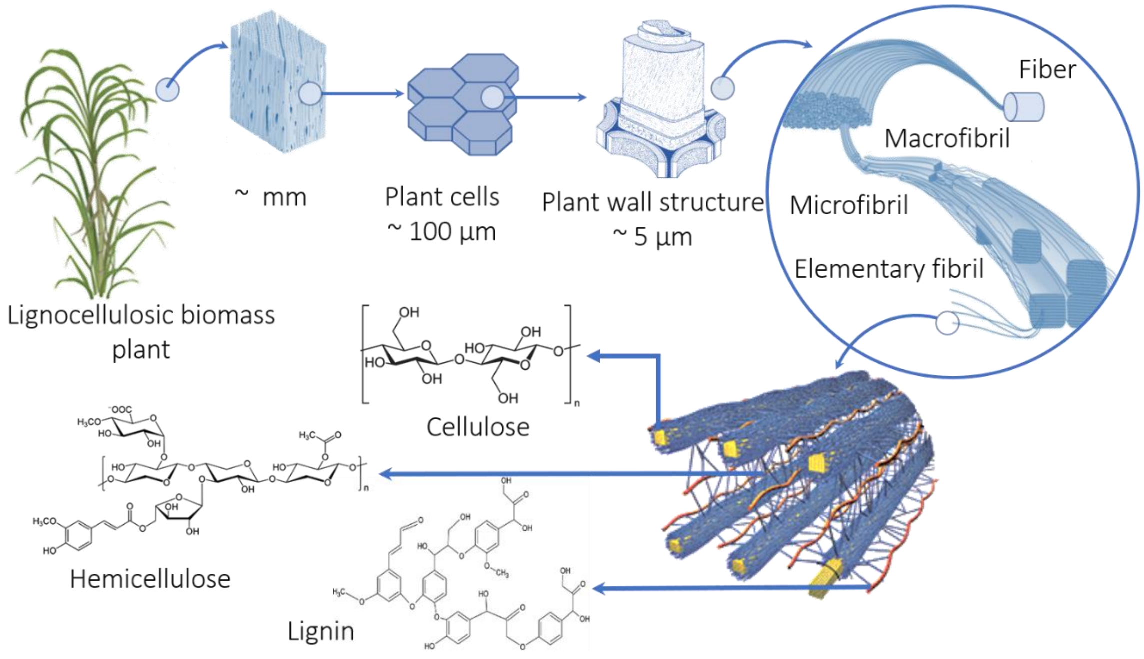

Figure 2.1. Structural composition of lignocellulosic biomass materials, showing the function of the main polymer constituents [38, 39].

2.4. Biomass Processing in Biorefineries

The processing and conversion of biomass materials to produce transitional products for synthesizing energy, liquid fuel, and chemicals happen in biorefineries. The raw biomass feedstock undergoes handling and preprocessing through several transport systems before being fed into the thermochemical conversion platforms. The production of valuable end products from biomass involves deconstructing the lignocellulosic matrix structure into reactive intermediaries by biochemical or thermochemical pathways [40, 41]. Under biochemical conversion processes, the constitutive polysaccharides (cellulose and hemicellulose) are released from lignin using different pretreatment processes, followed by hydrolysis into simple sugar monomers (e.g., xylose and glucose), and finally, fermentation of the released sugars to produce biofuels and chemicals [42, 43]. Under thermochemical conversion processes (pyrolysis, gasification, combustion, co-firing, liquefaction, and carbonization), the biomass feedstock undergoes a controlled heating and thermal transformation into syngas or flue gas, liquid bio-oil, and solid biochar [44-46]. The efficient production of energy products from biomass depends on the correct handling of biomass feedstock materials.

Figure 2.2 shows a simplified diagram of the lignocellulosic biomass refining process in biorefineries.

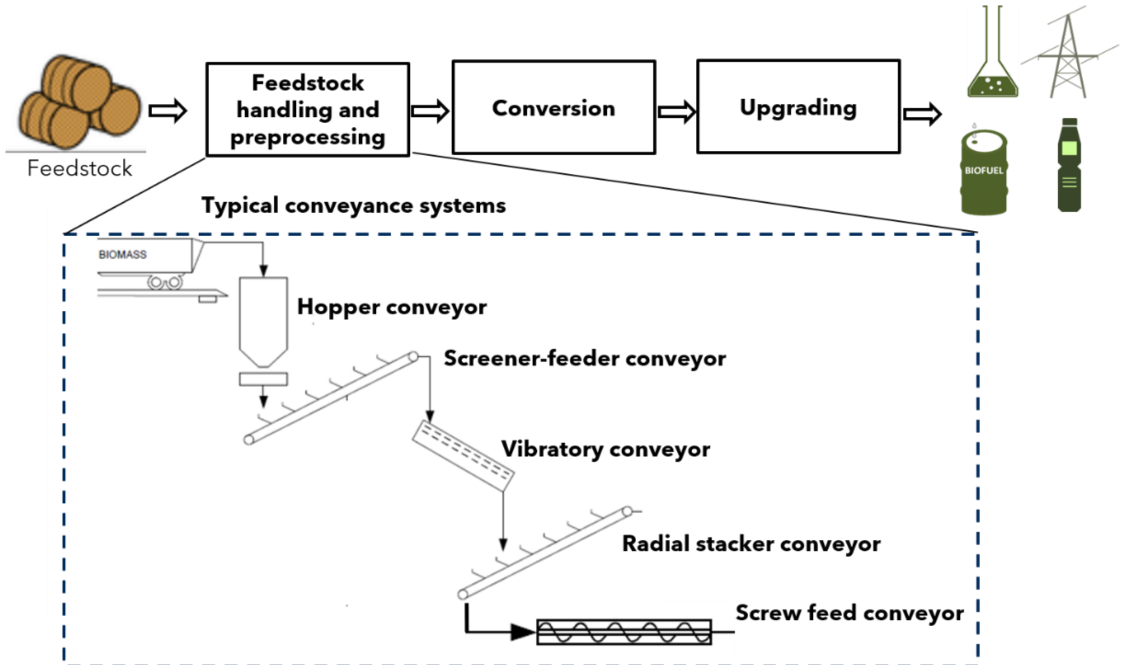

Figure 2.2. A simplified schematic diagram of the lignocellulosic biomass refining process [47].

One of the most overlooked areas in the bioenergy industry is receiving the biomass feedstock material from the raw material sources and transporting it to the conversion equipment, i.e., the conveyance process. During the conveyance process, the lignocellulosic biomass feedstock passes through several conveyance systems, like a hopper conveyor, screw-feed conveyor, screener-feeder conveyor, and vibratory conveyor [48]. The screener-feeder conveyors are preferred for transportation over longer distances, whereas screw conveyors serve as an inexpensive alternative for shorter-distance applications [49].

During feedstock flow through typical conveyance systems in the biorefinery, the biomass material exhibits a range of behaviors owing to the different stress states related to their flow condition, the mechanics of which require further investigation. The biomass conveyor system design involves accounting for the feedstock variability and ensuring reliable and uniform flow characteristics [48].

2.5. Flow Issues in Biorefineries and Their Economic Impact

The feedstock material experiences flow through different conveyance systems issues, and they encounter flow issues unique to each conveyor [50]. Some of the most common flow issues include:

- Bridging (Arching): This is a flow issue encountered in hopper conveyors, in which an arch-shaped obstruction forms above the hopper outlet [51]. The biomass feedstock undergoes mechanical interlocking, and the arch supports the contents of the bin. Thus, feedstock material discharge through the outlet becomes obstructed [52].

- Ratholing: This is another issue endemic to hopper conveyors, in which a pipe-like vertical-cavity forms above the outlets [53, 54]. The feedstock can only flow through the cavity, with any material outside becoming stagnant [55].

- Clogging: This occurs in screw conveyors (augers) when the buildup of material (owing to large particle size, high moisture content, or cohesiveness) leads to a blockage of the auger blades [56, 57]. Clogging causes high disturbance in the system, leading to power, feeding, and safety issues [58].

Figure 2.3 shows the issues biomass materials face in different conveyor systems.

The feedstock flow issues in the conveyor systems have a highly detrimental effect on the biorefinery's operational economics [59, 60]. Due to the challenges faced in the feedstock handling and preprocessing stage, biorefineries typically operate on-stream for only 20-50% of their design capacity [61]. A techno-economic analysis done for a conceptual biorefinery assessed that to reach the break-even point, the biorefinery needs to operate

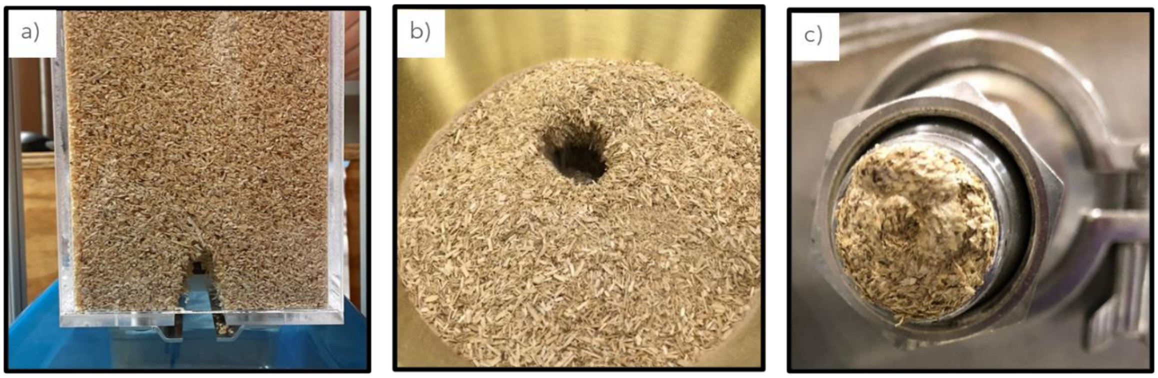

Figure 2.3. Flow issues prevalent in biorefinery conveyor systems, a) bridging (arching), b) ratholing, and c) clogging.

on-stream for 90% of its design capacity (as shown in Figure 2.4) [47]. Thus, to meet annual cost targets, biorefineries need to raise the minimum fuel selling price (MESP) to more than 80% of the target selling price, making them non-competitive with conventional fuel refineries [62, 63].

The flow issues have implications beyond the biorefining industry. The change in flow properties of granular materials (highly prevalent in all manufacturing industries) during the flow process manifests as processing problems and severely affects product quality [64]. For example, 94% of all solid processing plants experience processing problems [65, 66]. The pharmaceutical industry is especially susceptible to these problems as 80% of the processed products (tablets, pills, or capsules) are granular in nature [64, 67, 68]. Therefore, a fundamental understanding of the controlling factors behind the granular biomass flow can benefit the global manufacturing and processing industry.

Significant work has been done to analyze and improve the logistics of biomass feedstock flow, including improvement of biomass collection and pretreatment operations [69], supply chain management [70], and the harvest and preservation of feedstock [71]. However, feedstock quality remains a critical issue, as feedstock consistency is integral for reliable, efficient bio-refinery operation [66]. Therefore, a physically and chemically uniform, reliable, and consistent biomass feedstock is essential for optimum biorefinery operation [72].

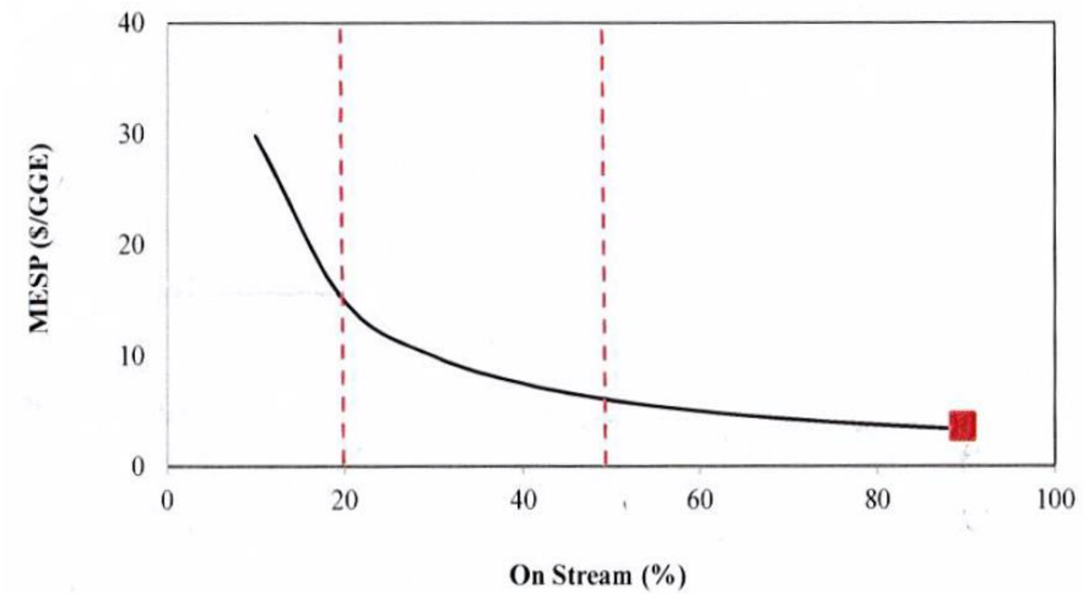

Figure 2.4. Economic impacts of reduced on-stream time in a fast pyrolysis process [47].

2.6. Flow Analysis of Lignocellulosic Biomass Feedstock

Biomass feedstock exhibits varying quality arising from variations in species (herbaceous/woody), geographical locations (warm/cold climate), fractional forms (chips/pellets/sawdust), seasonal effects, and harvesting/collection techniques [73]. The variations are especially evident in the biomass particle morphology (size/shape) and size distribution, which are essential particle properties that influence feedstock flow behavior [74].

Figure 2.5 shows three different varieties of biomass feedstock materials from diverse sources, namely herbaceous crops (switchgrass), softwood (loblolly pine), and hardwood (hybrid poplar), subjected to the same preprocessing techniques (hammermilling) and sieved to a particular size range. Yet, particle shape and size distribution are highly different between them.

The quality of biomass feedstock is highly dependent on the feedstock's physical, chemical, and engineering properties. The most influential properties include particle morphology and distribution, bulk and particle density, Poisson’s ratio, elastic modulus, friction coefficient, and restitution coefficient. The properties are interlinked, regulating biomass conveyance and conversion process efficiency [75]. The material and interaction properties are highly influential in designing biomass transport equipment, storage systems, and thermochemical conversion apparatus [76, 77].

Figure 2.5. Lignocellulosic biomass materials of different morphological features, a) switchgrass, b) loblolly pine, and c) hybrid poplar.

Since biomass feedstock has a granular microstructure, they exhibit continua-like behavior in the bulk scale [78] and stress inhomogeneity in the particle scale [79]. Therefore, researchers have focused on the effect of the bulk-scale and the particle-scale material characteristics and engineering properties on the feedstock variability and flow conditions. Furthermore, since the conveyance process is a significant cost driver in bioenergy and biofuel production, investigating the biomass properties' effect on flow behavior is highly relevant.

While these properties can be studied individually, each parameter's measurement during the bulk scale analysis of the biomass feedstock flow is expensive and time-consuming [80]. Additionally, the interaction effects during the flow process also require consideration. As such, computational simulation techniques provide a more feasible particle flow analysis [81]. The discrete element modeling technique (DEM) [82] is widely used for analyzing particle dynamics. In this method, computational analysis of the particles' movement (particle displacement, velocity, and related forces) involves solving Newton’s equations of motion [83]. Researchers have extensively used the discrete element method to analyze the flow of granular materials in a wide variety of conveyance systems, such screw conveyors [84-86], hopper conveyors [87-89], and belt conveyors [90, 91]. Others have applied the DEM technique to analyze the mechanical behavior of specific feedstock materials such as switchgrass [92], corn stover [93], pine [94], and poplar [95]. However, a robust approach combining experimental and computational techniques is necessary for analyzing a wide range of feedstock materials and conveyance systems. Furthermore, robust computational models validated by physical experimental measurements have the potential to predict future flow issues encountered by the biomass feedstock in an actual conveyor system. Thus, the developed experimental and computational analysis framework will help in designing more efficient biomass transport equipment, storage systems, and thermochemical conversion apparatus.

2.7. Experimental Investigation of Lignocellulosic Biomass

2.7.1. Flow Behavior of Biomass Particles

Lignocellulosic biomass particles fall in the category of granular materials, which are abundant in the natural environment and industrial applications [96]. Particle scientists have estimated that more than 50% of all manufactured products are either in granular form or involve the processing of granular materials [97, 98]. Despite their ubiquity, the flow behavior of granular materials is not clearly understood [99]. Solid particulate flow is a complex behavior dependent on many powder characteristics, with no one parameter or tests completely and quantitatively capturing the flow behavior [100]. A granular or powder material's ability to undergo flow under a specified set of conditions represents the flowability of said material [51]. Flowability results from aggregating the physio-mechanical properties that influence the flow and equipment used to handle, process, or store materials. No unified framework exists for comprehensively describing the particulate flow behavior [101, 102]. Hence, researchers typically use a combination of experimental techniques and empirical correlation to characterize granular particulates [103].

Scientists characterize the flow behavior of granular particulate assemblies in terms of their low shear strength, which depends on the stress states. For granular materials, the shear strength (τ) is defined in terms of the normal stress (σ) and the dimensionless coefficient of friction (μ), a commonly used measure of frictional behavior as presented in Equation 2.1,

$$\tau = C + \mu\sigma. \tag{2.1}$$

where, C = Cohesion (stress independent component),

μ = coefficient of friction = $tan(\varphi)$,

φ = angle of friction, and

σ = normal stress.

The coefficient of friction represents two forces acting perpendicularly and in parallel, respectively, to an interface between two bodies under relative motion or impending relative motion [104]. The translational and rotational motions of the particles in a solid particulate system are closely related to the particle-particle and particle-wall coefficients of friction [105]. The cohesion force is essentially zero for unconsolidated granular material [106, 107]; thus, the frictional behavior only contains the contribution from the internal friction [108].

For loose material assemblies, the static angle of friction, and thus the coefficient of friction, is equal to the angle of repose, which is the maximum angle at which a pile of unconfined material can rest on an incline without collapsing [109]. According to the classical Coulomb's theory of friction, the angle of internal friction for a conical-shaped pile is equal to the arctan of the maximum static friction coefficient, i.e., the angle of repose, assuming the frictional force is independent of the contact area and is linearly related to the normal force [110]. A larger coefficient of friction and the resulting higher resistance to motion result in the consumption of kinetic energy and the formation of a material pile of high potential energy, thus exhibiting a high repose angle [111]. For denser material assemblies, the angle of friction and the associated coefficient of friction can be determined from the slope of the Mohr-Coulomb failure envelope, representing the shear strength at zero confining stress [112].

The angle of repose test is a popular technique for solid particulate system analysis. The angle of repose is an indicator of the flowability of material, and researchers classify the flowability as free-flowing (30-38°), fair to passable flowing (38-45°), and cohesive (45-55°) [113, 114]. A variety of methods are available to determine the static angle of repose of unconfined granular material, including the hollow/tilting cylinder method [115-117], the fixed funnel method [118, 119], and the revolving cylinder/drum method [120, 121]. Al-Hashemi et al. conducted an exhaustive review of the different methods for the angle of repose measurement [122]. They concluded that selecting a measurement method depends on the specific objectives, materials, and application.

Another standard flow characterization test is the shear cell test. A.W. Jenike [108] initially developed this technique to design hoppers and silos handling bulk solid materials. Under this test, the bulk granular specimen is contained in an annular shear cell and loaded from the top with vertically acting force through the cell lid to adjust the stress level. During testing, the shear cell rotates, while lid rotation is prevented by tie rods, leading to solid specimen shearing. Forces acting on the tie rods are measured to calculate different flowability and frictional parameters, such as the angle of internal friction, time consolidation, angle of wall friction, and bulk density [123-125]. Shear cells are widely used to classify the flowability of granular materials and determine the relationship between their bulk density and principal stress components [126]. There are international standards available specifying the parameter determination procedures [127], and extensive studies have been performed to validate the use of shear cell testers for specific situations [125, 128-130].

2.7.2. Relationship Between Biomass Flow Behavior and Structural Composition

Experimental characterization methods and empirical relationships for determining flow parameters solid particle assemblies available for various situations. However, the relationship between these parameters and the structural and material properties of the particle materials is not well understood [131, 132]. The specific components of biomass materials have an outsized influence on their particle and bulk scale properties. While prior research show that cellulose, hemicellulose, and lignin play distinct structural roles in the biomass matrix and contribute to the biomass mechanical properties (e.g., mechanical strength, chemical stability, structural rigidity, etc.), the individual contribution of each biopolymer is more challenging to quantify due to their interwoven nature. Limited studies focus on the exact nature of the relationship between lignocellulosic structural composition and specific mechanical properties of biomass materials.

Figure 2.6 illustrates lignocellulosic biomass structural constituents and their influence on particle and bulk-scale physiomechanical properties.

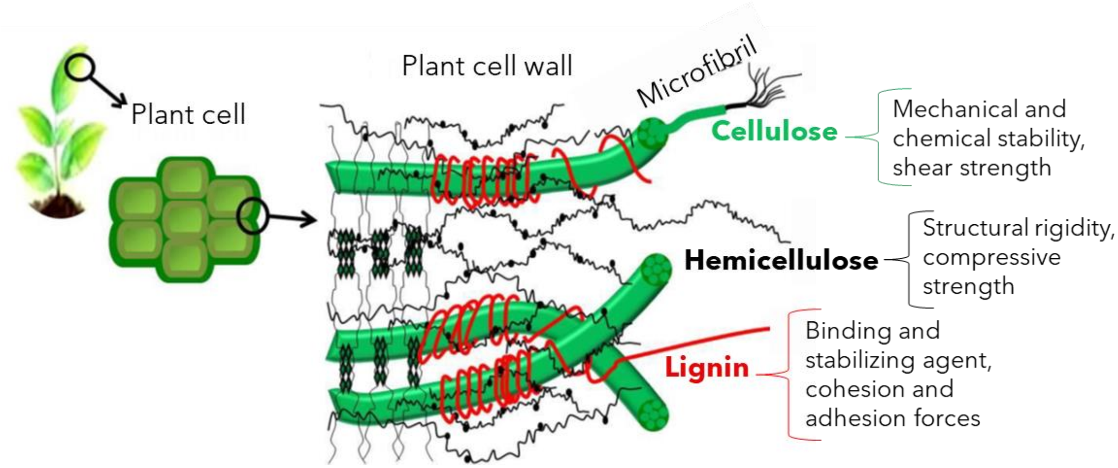

Figure 2.6. Relation between biomass structural constituents and physiomechanical properties [133].

The individual constitutive components can be extracted to alter the matrix structure and composition through biochemical (enzymatic degradation [31, 134]) and chemical treatments (aqueous [37], dilute acid [135], or alkaline [136] pretreatment processes). The alteration of the biomass structure has led to phenomena such as the diminution of compressive strength in spruce wood due to the thermal degradation of hemicellulose [137], the change of transverse elastic modulus of wood cell wall due to a lowered proportion of cellulose and lignin [138], and increase in tensile strength of lignocellulosic jute fibers by removal of hemicellulose [139].

From the previous studies, we infer that the alteration of the biomass structure by changing the composition of hemicellulose, lignin, and cellulose content can affect the strength and frictional characteristics and, therefore, biomass assemblies' flow behavior. Consequently, the following section describes the techniques utilized to change the composition of biomass structural constituents by previous researchers.

2.7.3. Selective Extraction of Biomass Structural Constituents

Biomass researchers have utilized a variety of pretreatment processes for structural modification of lignocellulosic materials to improve the conversion process of bioenergy and biofuels. Pretreatment efforts can be categorized into two major categories: thermo-chemical and biological.

Thermo-chemical pretreatment processes include hot water extraction [140-142], steam explosion [143-145], ammonia fiber expansion [146, 147], dilute acid pretreatment [148-150], alkaline pretreatment [149, 151], wet oxidation [152, 153], and CO_2 explosion [154, 155]. Among the different methods, the hot water extraction process, which utilizes hot water at a moderately high temperature, is a popular choice due to the simplicity of the process, as the process requires no additional chemicals or specially designed equipment [156]. Researchers have successfully used the hot water extraction process to dissolve hemicellulose content in lignocellulosic biomass feedstock, e.g., switchgrass and loblolly pine [141], sugar maple [157], and Norway spruce [140, 141, 157], and fruit processing residues [158].

For biological pretreatment processes, the wood decay fungi are a suitable choice as they are among the most effective bio-converters of native cellulose and play an important role in the biodegradation of lignocellulosic biomass by producing an array of enzymes [159]. Scientists categorize Basidiomycete wood fungi (fungi whose spores develop in basidia) in two categories: brown rot and white rot fungi, based on the color of decayed wood and the degradation mechanism [160]. Brown rot fungi preferentially degrade cellulose and hemicelluloses [161]. The degradation mechanism involves a nonenzymatic process, i.e., the Fenton reaction, followed by depolymerization of radicals, and finally, enzymatic action leading to cellulosic degradation [162]. White rot fungi rely more on enzymatic degradation of hemicellulose, cellulose, and lignin [163]. The white-rot fungi degrade the three major wood components either simultaneously or selectively by preferential attack of lignin and hemicelluloses, followed by cellulose hydrolysis [164]. This is reflected in simultaneous weight loss and cellulose depolymerization [165]. Lignin degradation using white-rot fungi involves the secretion of lignin-degrading enzymes, especially peroxidases [166]. The degradation of lignin can be performed in two ways, a) selective decay, in which lignin and hemicellulose are selectively degraded while cellulose fraction remains unaffected. Some commonly used species include *C. subvermispora*, *Dichomitus squalens*, *P. chrysosporium*, and *Phlebia radiata* [167]. b) non-selective decay, in which approximately equal amounts of all fractions of lignocellulose are degraded. Example species include *Tramester versicolor*, *Fomes fomentarius* [168].

The effect of brown rot and white rot fungi decay can be investigated in a variety of ways, such as nuclear magnetic resonance (NMR) spectroscopy [169-171], FT-IR spectroscopy [172, 173], solid-state cross-polarization (CP) [170, 174, 175], X-ray diffraction (XRD) [176-178], acid hydrolysis using high-performance liquid chromatography (HPLC) [178]. These techniques provide complimentary information about the lignocellulose matrix changes in terms of cellulose crystallinity and crystal lattice spacing [164, 179].

In addition to the characterization of biomass structural constitution either in their raw state or after undergoing thermochemical or biological modification, it is necessary to quantitatively determine the biomass's flow parameters. The next section describes the experimental techniques used to characterize solid particle assemblies applicable to lignocellulosic biomass materials.

2.8. Computational Investigation of Lignocellulosic Biomass

In biorefineries, particulate flow processes are prevalent and have an outsized influence on the performance of crucial unit operations and core systems, e.g., conversion systems. The particulate flow processes are designed following insights and design practices from other biological materials. However, considering the challenges encountered in biorefining facilities, there is an opportunity to deepen our fundamental knowledge of lignocellulosic biomass materials' mechanics and update design practices for their particulate flow equipment. These endeavors will directly benefit process efficiency and scale-up. Process modeling tools are becoming increasingly necessary to gain valuable insight into these processes, translating into improved designs.

Lignocellulosic biomass particulate systems are granular in nature, i.e., they are a collection of macroscopic particles that undergo unique microscopic interactions [180]. Granular particulate systems, such as sand, are ubiquitous in nature and have applications in various industries, including construction, mining, and agriculture [181, 182]. The mechanics of these materials are complex, and their properties span the range of solids, liquids, and gases. Particulate systems' properties depend highly on the micromechanics of both the contacting and non-contacting forces between particles [183]. The accurate understanding and measurement of these forces are essential for predicting the flow of biomass materials and the design and development of machinery and equipment used for handling, feeding, and processing biomass feedstock materials [56, 184]. Thus, detailed knowledge about the mechanics of biomass particles at the micro or macroscale is important for academics and industry practitioners.

While bulk-scale experimental analyses of granular materials are possible in a laboratory environment, they can be costly and are impractical for particle-scale investigations. Furthermore, the opacity of most analytical flow instruments limits accurate experimental measurements using conventional high-speed optical imaging approaches [185, 186]. Computational simulation techniques can be used to investigate a diverse set of granular materials under different flow conditions in a cost-effective and efficient manner [187]. Therefore, the high cost and inconvenience related to the bulk-scale analysis of granular materials [80] makes computational modeling a preferred choice for conducting granular flow analysis [81, 103, 188].

Researchers classify computational simulation techniques for granular materials into two broad categories: i) continuum models such as finite element method (FEM), finite volume method (FVM)) and ii) particle models such as the discrete element method (DEM), Monte Carlo method, and cellular automata [189]. Particle models represent the solid particulate system discretely, and the particle-particle collisions are explicitly solved to provide a more accurate perspective of the interactions [190]. Particle scale computational models are used in both academia and industries for process modeling of solid particulates, including pharmaceuticals [191, 192], food [193], agriculture products [194], and specialty chemicals [195, 196].

In particular, discrete element computational modeling (DEM) has emerged as a suitable technique for simulating the movement of granular biomass particles [197]. The approach is especially advantageous because it relates the macroscopic and microscopic behavior of biomass particulates, which are inexorably related, and thus allows for a detailed accounting of the interaction effects between the individual particles for greater fundamental insights to practically develop control and optimization strategies for the flow system of such materials [198]. The ability of the DEM method to provide a more thorough description of particle dynamics has made it popular for investigating granular systems [199].

Figure 2.7 shows the application of the DEM method for the flow simulation of pharmaceutical tablets in a triangular hopper.

A wealth of fundamental knowledge of solid mechanics already exists for many granular materials (e.g., sand). However, lignocellulosic biomass particulates and their assemblies have unique peculiarities that render the prospect of a completely experimental-based approach unrealistic. The complex hierarchical structure of lignocellulosic biomass makes them highly recalcitrant [200] and makes the inference of physio-mechanical properties of biomass materials challenging [201]. For example, the density of particulate systems in typical DEM simulations is bulk density (also known as envelope density) [202]. For most biomass materials, the envelope density is less than the particle density (also known as skeletal density), which is the ratio of the mass of solid material to the sum of the volumes of the solid material and closed pores within the material). The measurement of either of these densities is not trivial for biomass materials. The envelope density is not highly dependent on any change in the particle sizes, whereas the skeletal density increases with the

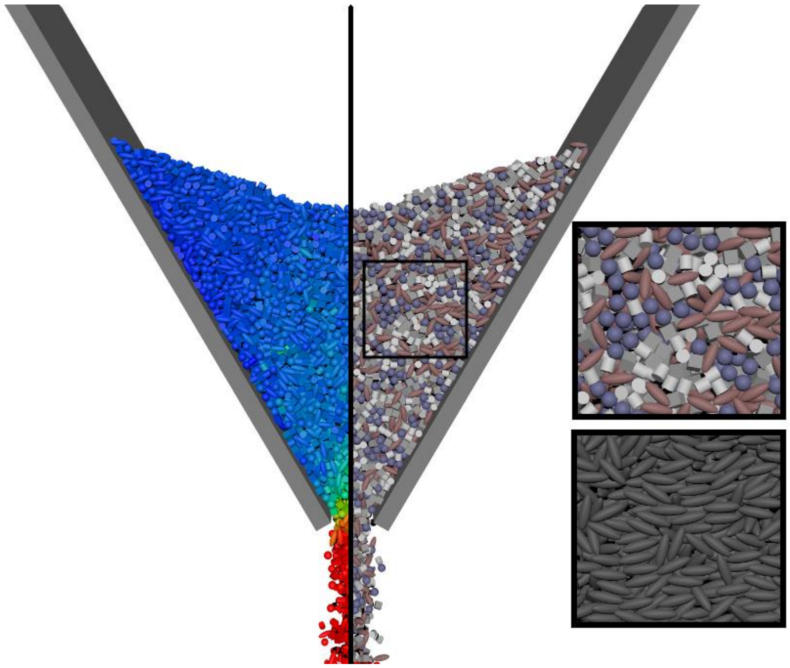

Figure 2.7. Discrete element modeling of granular materials (pharmaceutical tablets) [203].

reduction in sizes. This is due to the decrease in the skeletal volume due to the opening up of interparticle voids [204]. The changing void structures make the use of traditional characterization techniques like surface area analysis by Brunauer–Emmett–Teller nitrogen adsorption/desorption technique [205] or pore size and volume analysis by Barret–Joyner–Halenda methods [206] quite challenging.

The variation in the intraparticle porosity influences the stiffness and the heat and mass transfer process during the conversion [207]. Furthermore, the particle shapes and size distribution vary considerably between different species of biomass particles, e.g., switchgrass, pine, poplar, corn stover, etc., and can significantly affect their bulk flow behavior [208]. Prior researchers have shown that the computational results match the experimental measurements only when the contact force and frictional force models take the geometry of the particles into account [209]. Finally, the moisture content in biomass assemblies significantly influences their mechanical behavior [210, 211], which is challenging to capture in the computational simulation process.

In summary, the discrete element computational modeling of lignocellulosic biomass requires determining particle-scale properties by direct or indirect measurement and calibration process, selecting proper physical models to represent the interaction between the particles and their surroundings, and designing characterization tests whose outputs are comparable with experimental measurements.

The next section of this literature review provides a theoretical presentation of the discrete element method and reviews its application in modeling granular biological materials in general and lignocellulosic biomass materials.

2.8.1. The Discrete Element Method (DEM)

Discrete element modeling is a numerical technique developed by Cundall and Strack [82] to compute the characteristics of systems represented by particles. The basic philosophy behind DEM is modeling actions at a microscopic level to study the effect of these actions on a whole media's motion at the macroscopic level [212]. The DEM allows the determination of particle dynamics parameters (e.g., the magnitude and direction of forces on each particle), which are challenging to determine using a physical experimentation method [213]. A well-designed DEM model captures the physical interaction between the particles and their surrounding environment, applies appropriate boundary conditions to depict the physical process, and produces results like experimental measurements.

The development of a DEM model requires three major components:

i) a contact detection strategy between particles and the surrounding environment,

ii) time-discretized equations of motion governing the particle motion, and

iii) contact models for calculating the interparticle contact forces [214].

Researchers have used two contact detection strategies: the hard-sphere and soft-sphere methods. A hard-sphere method is an event-driven approach that assumes particles as rigid bodies [215]. Particle collisions are processed sequentially, one collision at a time, without explicitly considering the contact forces. The soft-sphere method is a deterministic or time-driven approach that assumes particles undergo deformations during contact [216]. The force model calculations include these deformations. It is a more flexible approach than the hard-particle method since it allows the modeling of particles of different shapes and particle collisions of longer duration [214]. Researchers have employed the soft-sphere approach for investigating various phenomena like hopper flow [81, 87, 213, 217], mixing and granulation [218], particle packing [219], and transport properties [220].

Figure 2.8 shows a schematic illustration of the two major particle contact detection models.

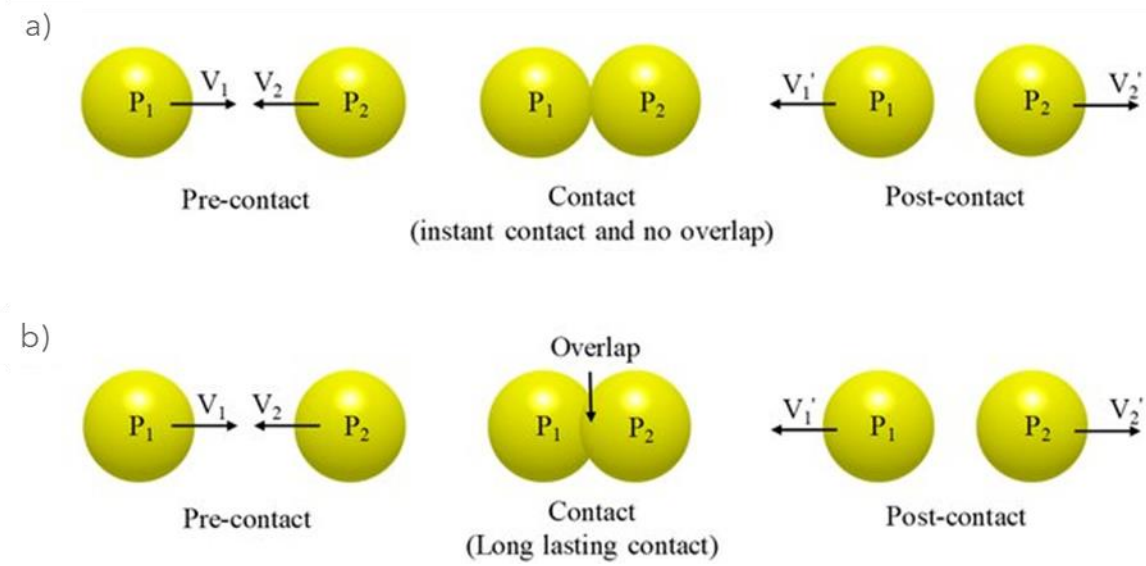

Figure 2.8. Schematic diagram of a) hard-sphere model and b) soft-sphere model [192].

The motion of solid particulate systems, namely, the rotational and translational motion, are modeled by Newton's laws of motion [221, 222].

The particles' translational and rotational motions are described mathematically by Equations 2.2 and 2.3.

$$m_i \frac{dv_i}{dt} = \sum F_i^C + \sum F_i^{nc} + F_i^f + F_i^g \,, \tag{2.2}$$

$$I_i \frac{d\omega_i}{dt} = \sum_j M_{ij} \,, \tag{2.3}$$

where, v_i = translational velocity of particle i,

$\sum_j F_{ij}^C$ = contact force acting on particle i by particle j or walls,

$\sum_k F_{ik}^{nC}$ = non-contact force acting on particle i by particle k or other sources,

F_i^f = particle–fluid interaction force on particle i,

F_i^g = gravitational force,

ω_i = angular velocity of particle i, and

M_{ij} = torque acting on particle i by particle j or walls.

Figure 2.9 schematically describes the fundamental forces acting between two particles in contact.

The final component of a successful DEM model is the calculation of the interparticle contact forces and torques. The calculation of contact forces uses either a linear or non-linear approach.

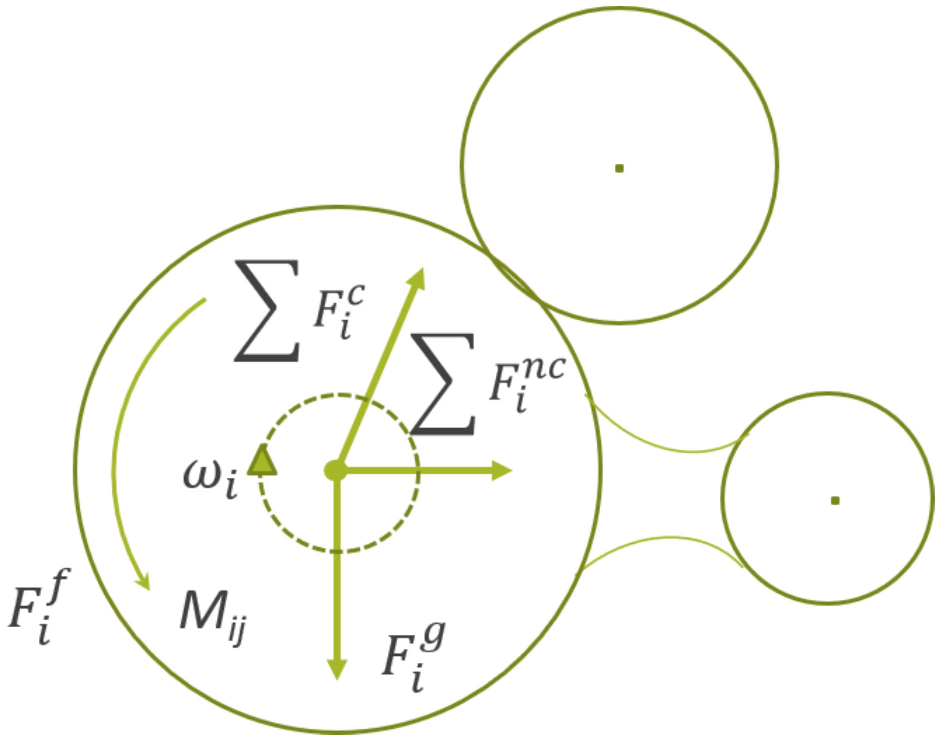

Figure 2.9. Schematic diagram of forces operating between particles [187].

The linear approach assumes the force and displacement to be linearly correlated, i.e., the contact forces increase with particle displacement [223, 224]. The non-linear approach considers the shape of the particles [225]. The inter-particle interaction at the point of contact gives rise to a torque responsible for the particle's rotational motion. The torque consists of a normal and tangential component [226]. The normal component is called the rolling friction torque and is of special interest to researchers [227, 228]. The simplest case considers the particles rigid and in contact at a single point, and the normal forces do not contribute to the total torque. Typically, DEM models consider torque to be zero for the sake of simplicity. However, the consideration of torque is important in cases where there is a shift between static and dynamic forces, such as strain localization [229], heaping and piling [105], and tracking of planar particles [230].

By calculating the contact forces and torques, we can account for the particles' trajectories and solve Equations 2.2 and 2.3 to describe the particulate system's dynamic state completely.

2.8.2. DEM Model Development

The development of a DEM model for particulate flow systems involves specifying four significant aspects (Zhu, Zhou, Yang, & Yu, 2007), which are:

a) Model parameters selection (material/interaction properties)),

b) Particle representation (shape and size distribution),

c) Particle contact models (contact force calculation), and

d) Computational flow characterization (real physical process)

These four aspects are defined, and their values are specified to develop particulate media investigation in different software packages, such as LIGGGHTS (developed by Sandia National Labs and based on LAMMPS), Kratos Multiphysics (developed by CIMNE), Altair EDEM, GranOOO, and YadeDEM.

2.8.3. Model Parameters: Material and Interaction Properties

For simulating physical processes, we need to specify certain input parameters in DEM models. Typically, we classify parameters into two broad categories: material properties (intrinsic characteristics) and interaction properties (extrinsic characteristics). Critical material properties used as DEM modeling input include particle morphology (size/shape) and distribution, density, Poisson's ratio, and modulus of elasticity (particularly Young's modulus) [231, 232]. Interaction properties result from the particles' contact with the boundaries and surfaces of their surroundings and other particles. DEM's critical interaction properties include the coefficients of static friction, rolling friction, and restitution [233]. The DEM model's accuracy and reliability depend heavily on these parameters' appropriate values [234]. Instead of using actual measurements of the experimental procedures' parameters, DEM models often adopt a calibration approach. Under this method, the input parameters are varied, and appropriate statistical tools compare the computational model output to the output of the actual physical experiment [235]. The following section discusses the material and interaction properties necessary for DEM models and the characterization methods for determining these properties.

2.8.3.1. Particle Morphology and Size Distribution

Biomass particle shape and size are essential properties of biomass particles, and researchers recognize them as one of the key parameters influencing flow behavior. A realistic representation of biomass morphology is necessary for modeling the physical processes [74]. Biomass particles usually have highly irregular shapes and aspect ratios [198]. Particle scientists define the shape of biomass particles in specific dimensional parameters, typically by measuring three principal dimensions in the three orthogonally orientations (length, width, and thickness) [236]. Another method to describe particle shape is by specifying it in terms of three morphological parameters: form, angularity, and surface texture [237]. The form describes the dimensional difference of the particle along the principal axes (quantified in terms of sphericity), angularity describes the differences in corners/faces, and surface texture describes the particle surface roughness.

Figure 2.10 schematically describes the three major shape descriptors.

The selection of the particle size parameter is an important consideration. Typical size parameters include particle diameters (area equivalent diameter, equivalent perimeter), Legendre ellipse dimensions (length/width/thickness), Feret parameters, Martin parameters, Krumbein parameters, Heywood parameters, etc. The Feret parameters are extensively used for particle size analysis processes to projections of three-dimensional objects on a two-dimensional plane [238]. For quasi-3d particle analysis, the Feret length represents the distance between two parallel tangent lines [239]. In such a case, the Feret parameters along the x, y, and z planes are the Feret length, Feret width, and Feret thickness for the particle in three-dimensional space. Figure 2.11 shows a particle in three-dimensional space in terms of the Feret parameters.

Typically, particles are finely ground to reduce size and provide a more spherical shape (aspect ratio ~ 1) [240]. The biomass particles' packing highly depends on the size distribution [241]. The shape and size distribution affect non-spherical particles' packing, with the shape effect primarily controlling the packing structure. The angle of internal friction and the related angle of repose positively correlate with the aspect ratio [242] and angularity [243].

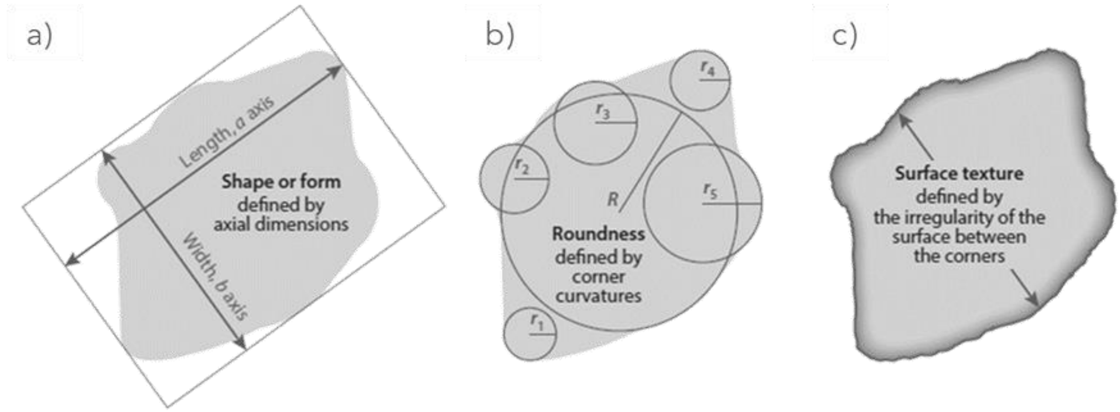

Figure 2.10. Schematic representation of three shape descriptors, a) form, b) angularity, and c) surface texture [237].

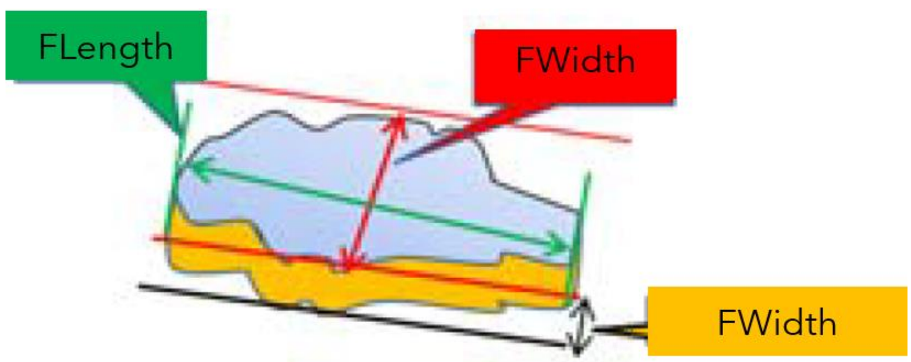

Figure 2.11. Representation of particle in three-dimension using the Feret parameters.

The particle size distribution significantly contributes to the particles' flowability and strength properties [244]. The increase in particle size leads to increased yield strength [245] and bulk density [246]. The increase in particle size and the resulting higher packing density leads to higher bulk and particle density of feedstock [208].

Traditional size measurement approaches like sieving can perform measurements in one dimension only (e.g., particle length). Additionally, sieving is highly dependent on the orientation of the particle. A particle of a prolonged dimension may pass through a sieve if the shorter side (width/thickness) is oriented parallel to the sieve plane. Hence, researchers have taken alternative characterization approaches for biomass feedstock particle morphology. Some alternative digital imaging techniques include a digital scanner combined with MATLAB image analysis toolbox [247], scanning electron microscope [248, 249], and dynamic image analysis [250, 251].

The dynamic image analysis method involves loading particle samples into the measurement field of high-resolution digital cameras, which capture the projection of particle shadows at a high frame rate. The built-in software analyzes the captured images to determine the particle at different orientations and the resulting particle size distribution and particle size and shape parameters (length, width, thickness, aspect ratio, sphericity, angularity, etc.).

2.8.3.2. Bulk Density

Bulk density ρ_b is defined as the amount of granular material by weight present in a specified volume. Bulk density directly influences the feedstock delivery cost to refineries and grain silos [252]. A feedstock with lower bulk density will have a higher transport and handling cost. The bulk density is highly dependent on the moisture content and particle morphology. Hence, any measurement of the feedstock's bulk density must include information about the moisture content and the particle size and shape distribution [253].

The typical methods used for determining bulk density are specified under the ASTM D1895B or ASABE S269.5OCT 2012 standards [208, 254]. In this method, a specified amount of sample material flows through a vertical hopper and fills up a container of known volume. Then, the overflowing material on top of the container is leveled off with a leveling stick. Finally, the material's weight inside the container is determined using an appropriate weight scale, and the bulk density is found by dividing the material weight by the container volume.

2.8.3.3. Modulus of Elasticity

The modulus of elasticity is the ratio of the normal stress to the normal strain. Young's modulus of elasticity (YM) reflects the relationship between the stress applied to an object in a specific direction and the deformation suffered in that direction. For bulk solid materials, the stress (σ) changes directly proportional to the strain, ε as per Hooke's law. Hence, for a sample subjected to a uniaxial load, the Young's modulus, YM is given by Equation 2.4.

$$\sigma = YM * \varepsilon. \tag{2.4}$$

For viscoelastic materials, e.g., granular materials like biomass, Young's modulus is based on the Hertz contact stress equations for small deformations. The parallel plate method has been used for computing the apparent Young's modulus for wheat [255], soybeans [256], and [257], whereas Young's modulus for corn was computed using a spherically shaped indenter on a curved surface [258, 259].

2.8.3.4. Poisson's Ratio

Poisson's ratio (PR) is the proportional deformation along an axis perpendicular to which the loading stress is applied. Mathematically, it is the absolute value of the ratio of the lateral strain, ε_l to the corresponding axial strain, ε_a in the direction of the applied load, as shown by Equation 2.5.

$$PR = \frac{\varepsilon_l}{\varepsilon_a}. \tag{2.5}$$

Typically, the Poisson's ratio is determined by plotting the volumetric strain as a function of the axial strain. Equations 2.6 and 2.7 show the relationship between the Poisson's ratio, ν, volumetric strain, ε_v, and axial strain, ε_a.

$$\varepsilon_l = \frac{\varepsilon_a - \varepsilon_v}{2}. \tag{2.6}$$

$$PR = \frac{\varepsilon_l}{\varepsilon_a} = \frac{\varepsilon_a - \varepsilon_v}{2\varepsilon_a} = \frac{1}{2}\left[1 - \frac{\varepsilon_v}{\varepsilon_a}\right]. \tag{2.7}$$

The Poisson's ratio for grains and oilseeds used as biomass feedstock (e.g., soybeans, corn, wheat) is determined using the ASAE Standards S368.4 (2003b) [260], with typical Poisson's ratio for most biomass materials ranging between 0.2-0.4 [256, 261].

2.8.3.5. Coefficient of Restitution

The coefficient of restitution (CoR) represents the intensity of the energy dissipated by the collision between the particles and is one of the critical properties for DEM techniques [262]. The damping parameter of visco-elastic contact models in DEM models depends on the coefficient of restitution value [187]. The coefficient of restitution has been determined by researchers using different techniques, such as expressing it in terms of the a) ratio of the normal components of impulse under compression restitution and under restitution [263], b) ratio of the normal components of the rebound and impact velocities [264], and c) ratio of the normal components of the reaction forces at the contact point under compression and under restitution [232]. For the third method, the coefficient of restitution is expressed in terms of the square root of the total kinetic energy before (KE_i) and after (KE_r) the collisions while neglecting the tangential frictional losses. The drop and rebound heights are measured for sample materials with minimal rotation and near-vertical rebound trajectories. The coefficient of restitution (CoR) is calculated using Equation 2.8 as the ratio of the square root of the initial height of drop (H_i) and the height of the rebound (H_R), assuming no energy loss except due to contact.

$$CoR = \left(\frac{KE_r}{KE_i}\right)^{\frac{1}{2}} = \left(\frac{H_r}{H_i}\right)^{\frac{1}{2}}. \qquad (2.8)$$

It is difficult to determine the coefficient of restitution for granular biological materials due to the shape irregularities and surface complexities, and it typically ranges from 0 to 1 (1 represents a perfectly elastic collision) [265]. Ramírez-Gómez et al. [266] determined the mean particle-particle restitution coefficient for a number of biomass pellets using a double-pendulum-based experimental setup as described by Wong et al. [267]. The different materials and their mean interparticle restitution coefficients are as follows: maize stalk (0.113), rape straw (0.135), rice husk (0.069), and vine shoots (0.151).

2.8.3.6. Coefficient of Static Friction

The coefficient of friction (μ) is the ratio of the force of limiting friction and normal reaction. A low value of the friction coefficient is indicative of no or little friction between the two materials. The coefficient of friction is related to the angle of friction, φ by Equation 2.9.

$$\mu = \tan(\varphi), \qquad (2.9)$$

The frictional forces between objects at rest and in relative motion are defined, respectively, in terms of the coefficient of static friction (μ_{sf}) and dynamic friction (μ_{kf}).

Researchers have determined the static coefficient of friction for various materials and contact conditions [194, 268-270]. Typically, the coefficient of sliding friction is determined using the ASTM D6128 – 16 method [271] with a direct shear tester, such as the Jenike shear box (Jenike & Johanson, Inc, North Billerica, MA). For biomass materials, the interparticle static coefficient of friction was found to be above 0.5, indicating higher resistance to flow [272]. Stasiak et al. examined pine biomass of different sizes in a Jenike shear box and found the static coefficient of friction to be dependent upon the material type, the normal compressive pressure, and the moisture content. The coefficient of friction values ranged from 0.50 to 0.62 [273].

2.8.3.7. Coefficient of Rolling Friction

The coefficient of rolling friction (μ_{rf}) is the ratio of the frictional force to the normal force at the contact surface, which prevents the particle from rolling. At the contact point, the force couple can be transferred between the particles and acts to resist the rotational motion of the particle without affecting the translational motion [230]. Jiang et al. [274] provided a micro-mechanical model based on a spring-dashpot assembly parallel with a series divider for modeling the rolling resistance at the particle contacts. Zhou et al. examined the effect of the rolling friction on the repose angle of glass beads and utilized coefficients of rolling friction values of 0.05 (range: 0-0.1) for particle-particle contact and double that value for particle-surface contacts. The results indicate that the angle of repose increased with the increase of rolling friction because of the reduction of kinetic energy by the rolling resistance and the formation of piles with high potential energy [275].

Table 2.1 summarizes a wide range of DEM parameters used by previous researchers for different organic and biological materials.

2.8.4. Particle Representation

The reproduction of biomass particles in a DEM environment with morphological parameters similar to real particles is essential for analyzing their flow behavior. As recreating potentially thousands of particles in typical biomass feedstock assemblies is practically impossible, the actual particle shapes in DEM are represented by simpler shapes such as disks for two-dimensional and spheres for three-dimensional cases [202]. The multisphere approach has been popular for modeling realistic granular materials due to its simplicity, fast computation process, and robust contact detection models [276, 277].

Table 2.1. Range of published material parameters for different organic materials.

Material Parameters	Sand	Wood chips	Switch grass	Hybrid poplar	Wheat straw	Corn stover
Bulk Density (kg/m³), ρ_b	1660-2650	209-498	149-190	170-204	690-823.2	95.4-174.5
Young's modulus (MPa), YM	100-650	35	25	40	36	30
Poisson's ratio, PR	0.25-0.3	0.3	0.25-0.35	0.2-0.3	0.3	0.35
Coefficient of restitution, CoR	0.2-0.8	0.3-0.5	0.3-0.7	0.2-0.5	0.4-0.6	0.3-0.5
Coefficient of sliding friction, μ_{sf}	0.6-0.8	0.2-0.8	0.4-0.7	0.5-0.7	0.4-0.7	0.3-0.6
Coefficient of rolling friction, μ_{rf}	1.6×10^{-5}	$0.2\text{-}0.5 \times 10^{-5}$	1.8×10^{-5}	1.6×10^{-5}	2×10^{-5}	1.5×10^{-5}
Angle of repose (°), AOR	25-35	42-50	32-43	38-45	35-44	36-45

Figure 2.12 shows the multisphere models of diverse biological materials with different morphologies.

However, the assumption of rigid particles necessary for applying the multisphere approach makes it only suitable for hard, non-flexible particles like wood chips [95, 278]. The modeling of materials with high degrees of softness and flexibility, like switchgrass, corn stover, and loblolly pine, must take into account the particle deformability and its effect on the flow behavior [279]. Thus, applying the multisphere method to irregularly shaped lignocellulosic biomass feedstock can result in a significant loss of accuracy [276]. Therefore, modeling complex, non-spherically shaped particulate systems require more robust and sophisticated particle models [276, 277, 280, 281].

While more complex particle-shape representations such as sphero-cylinders [282, 283], sphero-polyhedrons [284, 285], and composite-polygons (shell) [94] provide a high level of fidelity for representing particle shapes, implementation of such shape models has a highly prohibitive computational cost.

Additionally, the inherent material variability in particle shapes, distributions, and properties requires solving particle-particle interactions via custom contact detection algorithms, making them highly complex and time-consuming [286, 287]. Therefore, selecting the DEM particle shape must balance computational accuracy and efficiency.

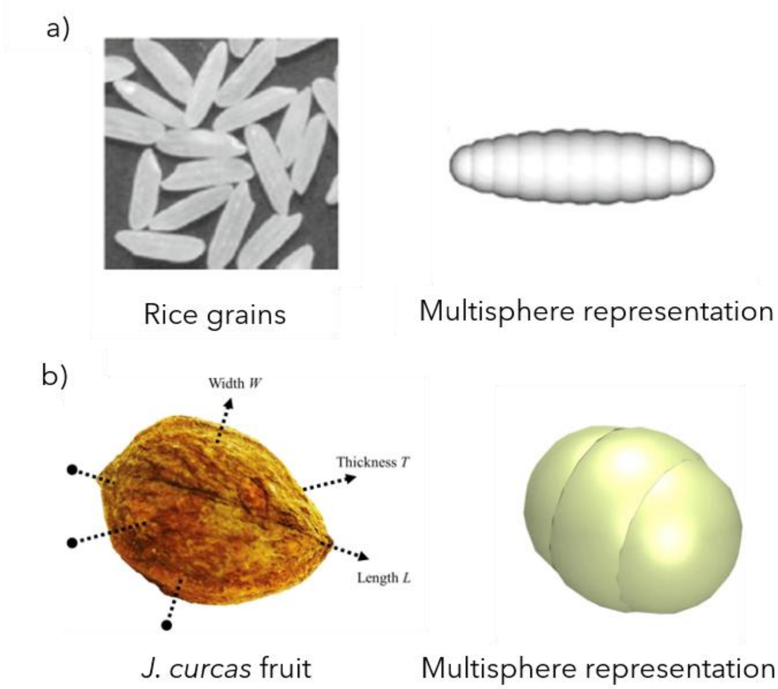

Figure 2.12. Multisphere model of a) rice grains [288], b) Jatropha curcas [289].

Figure 2.13 compares the computing time required for modeling the same group of particles in a cyclic loading-unloading assembly, indicating that the wall time rises exponentially from the spherical assumption to custom-polyhedral models.

The superquadric particle shape representation method is a mathematical representation of geometric shapes introduced by Barr [290] and later applied to discrete element modeling by Williams and Pentland [291], Cleary [81, 292, 293], and Lu [294]. It has been mooted as a potential accuracy and computational efficiency midpoint [291, 295].

Figure 2.14 shows different approaches for the representation of real particle shapes in DEM processes, namely multisphere, superquadric, and polyhedral approaches.

A superquadric is a generalized form of an ellipsoid whose exponents can possess any non-zero real value. A superquadric particle is expressed in three-dimensional space as a set of points (x, y, z), which satisfies the superquadric particle description as per Equation 2.10 [290].

$$\left(\left|\frac{x}{a}\right|^{n_2} + \left|\frac{y}{b}\right|^{n_2}\right)^{\frac{n_1}{n_2}} + \left|\frac{z}{c}\right|^{n_1} \leq 1, \tag{2.10}$$

where, a, b, c = particle half-lengths along the principal axes, n_1, n_2 = blockiness parameters ($n_i = 1,2,3, \ldots$).

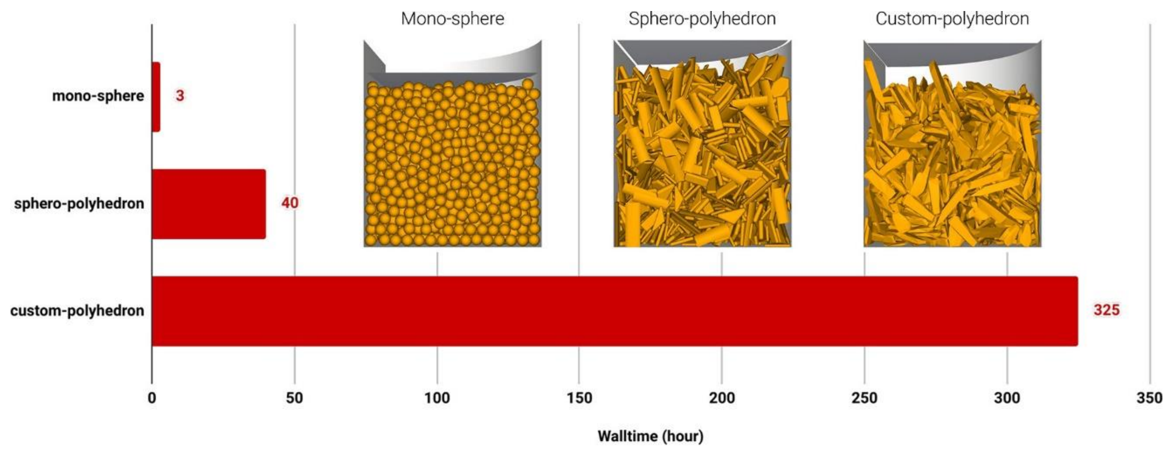

Figure 2.13. Comparison of the measured computing time (wall time) between the mono-sphere, sphero-polyhedron, and custom-polyhedron shape modes for a cyclic loading-unloading test using a quarter-geometry container [197].

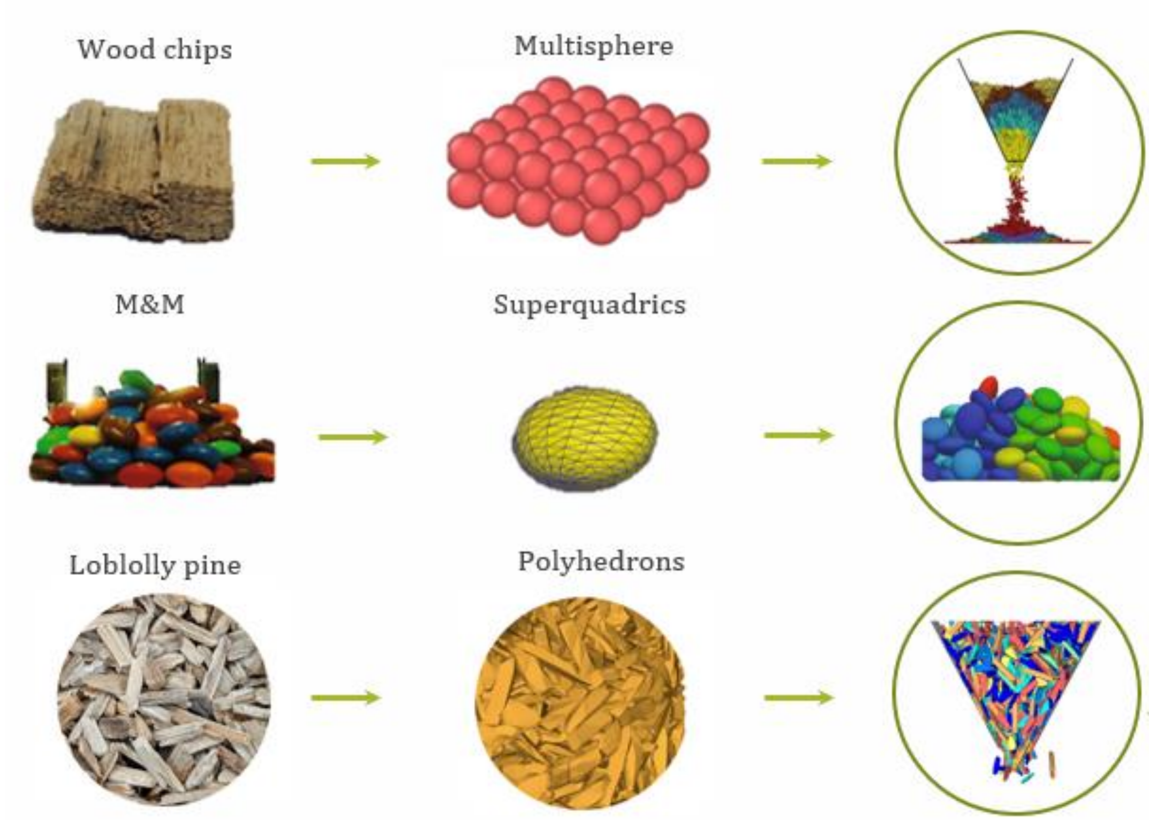

Figure 2.14. Representation of real particles in DEM with simpler shapes a) multisphere approach [278], b) superquadric approach [295], and c) polyhedral approach [197].

By controlling these five parameters, this equation can generate different particle shapes, such as a sphere, cylinder, box, ellipse, etc. Therefore, the superquadric particle assumption provides an optimum balance between the model accuracy and realistic particle shapes [296].

Figure 2.15 shows the different particle shapes approximated using the superquadric equation.

Unfortunately, limited studies are available on extracting the particle parameters necessary for generating a robust superquadric particle-based DEM model for simulating the flow behavior of biomass particulate systems. These shortcomings in the existing literature about accurately representing biomass particulates in DEM models motivated us to develop an analysis framework using appropriately selected material and interaction properties and morphological characteristics.

2.8.5. Particle Contact Model

In a particulate system, two particles are subjected to elastic contact with each other at multiple points. It is difficult to ascertain the particles' actual contact force distribution; instead, simplified contact models are used [297]. Computational modeling experts widely use two basic models for the contact forces: the linear model and the non-linear model. The linear model considers

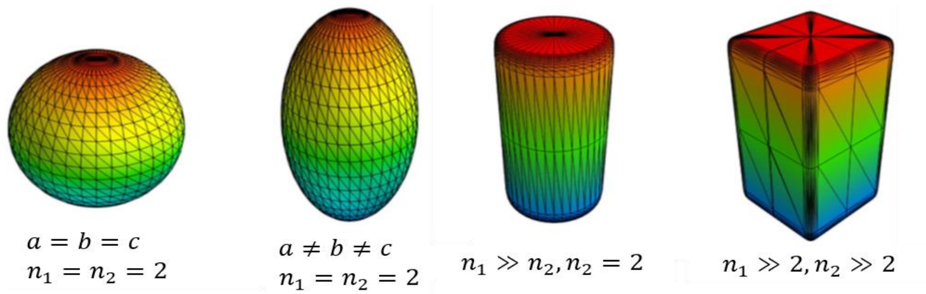

Figure 2.15. Superquadric representation of different particle shapes [295].

the relation between force and displacement to be linear, with the contact force increasing linearly with the increase of the displacement. Cundall and Strack [82] used a linear spring-dashpot system to account for the elastic deformation and viscous dissipation between the particles in contact. On the other hand, the non-linear approach is based on the Hertz-Mindlin contact theory and considers the particle shape [187, 225]. Hertz provided a non-linear solution for normal elastic contact [298], and Mindlin et al. developed a non-slip model for tangential elastic contact [299].

The full Hertz-Mindlin force model is highly complicated and is not efficient from a DEM simulation perspective. Instead, DEM programs use simplified and modified versions of the Hertz-Mindlin theory [296, 300-302].

For superquadric particles, contact detection involves finding the midway point, X_o between two superquadric particles A and B (Figure 2.16), and then solving the non-linear system described by Equation 2.11 iteratively (using Newton's method) for every particle pair at each time step.

$$\begin{cases} \nabla F_A(X) + \mu^2 \nabla F_B(X) = 0 \\ F_A(X) - F_B(X) = 0, \end{cases} \tag{2.11}$$

where, μ = proportionality coefficient, and

$F_k(X)$ = shape function of particle k.

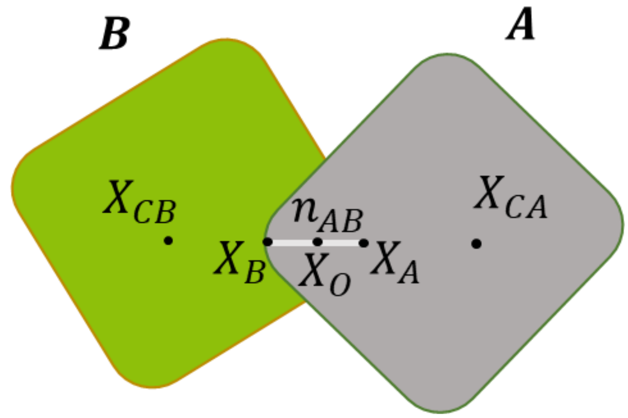

Figure 2.16. Particle-particle contact for superquadric particles.

The Hertz-Mindlin contact model represents the frictional force as a combination of normal and tangential forces. The normal and tangential force calculation uses the local curvature radius as the particle radius [281, 303].

The Hertzian normal force, F_N and tangential force, F_T are given by Equations 2.12 and 2.13.

$$F_N = \frac{4}{3} . \frac{E}{1 - \vartheta^2} \sqrt{R\delta^3}, \tag{2.12}$$

$$F_T = -8 \frac{G}{1 - \vartheta^2} \sqrt{R\delta^3}, \tag{2.13}$$

where E =Young's modulus,

ϑ = Poisson's Ratio,

$G =$ shear modulus, and

R = reduced radius $\left(\frac{1}{R} = \frac{1}{R_1} + \frac{1}{R_2}\right)$.

2.8.6. Computational Flow Characterization

The DEM method has been utilized for a variety of flow characterizations relevant to lignocellulosic biomass materials. Horabik et al. conducted a detailed review of DEM models used to characterize agricultural and biological granular materials [224]. Some of the modeled processes include the angle of repose test [304-308], shear cell test [222, 309, 310], triaxial test [311, 312], dynamic handling [313], uniaxial compression [269, 314], silo discharge [288, 315, 316], chute flow [233, 317], and mass flow [318]. In most of these cases, researchers examine the flow experimentally using standard measurement techniques to determine important flow parameters (e.g., angle of repose, velocity, kinetic energy, material outflow mass, wall pressures, and discharge time) and then compare with the numerical output of the DEM simulation using statistical techniques for validation purpose. Often a sensitivity analysis is performed using a Design of Simulations technique on the particle and flow system geometry and the input parameters of the DEM model to check for robustness [309, 319].

2.8.7. Validation of DEM Model Implementation

The choice of the time step is an important criterion to ascertain the robustness of the computational model. DEM utilizes an explicit numerical integration scheme to resolve the interparticle contacts, so the scheme is only conditionally stable [320]. Numerical stability depends on the size of the time step. The time step should be small enough that simulation should be numerically stable and provide physically reasonable solutions, but an extremely low time step would lead to a long simulation time [321]. The largest time step at which the simulation is numerically stable is called the critical time step. The original description of the discrete element method of single-degree-of-freedom systems considered only particle mass and stiffness for critical time step calculation [82]. However, modern DEM researchers argue that the approach taken by Cundall et al. is not applicable for non-linear contacts (e.g., Hertzian contact models), and the Rayleigh wave speed controls the time step [322, 323]. Therefore, we determine the critical time step using the criterion of Rayleigh time, $t_{Rayleigh}$, which is the time required for a Rayleigh wave to pass a spherical particle in a single time increment [324]. According to the literature, the critical time step, $t_{crit.}$ should be 10 to 20% of the Rayleigh time [225, 325]. The relationship between the critical time step and Rayleigh number is described by Equation 2.14.

$$t_{crit.} = 0.1 \dots 0.2 t_{Rayleigh} = 0.1 \dots 0.2 \frac{\left(\pi R \sqrt{\frac{\rho}{G}}\right)}{0.01631\nu + 0.8766}, \tag{2.14}$$

where G is the shear modulus, ρ is particle density, ν is Poisson's ratio, and r is the radius of the smallest particle.

References

(1) IEA. *Global Energy Review 2020*; International Energy Agency, 2020.

(2) EIA, U. *Annual Energy Outlook 2020*; Energy Information Administration, US 2020.

(3) Stöcker, M. Biofuels and biomass-to-liquid fuels in the biorefinery: Catalytic conversion of lignocellulosic biomass using porous materials. *Angew. Chem. Int. Ed.* **2008**, *47* (48), 9200-9211.

(4) Kobos, P. H.; Erickson, J. D.; Drennen, T. E. Technological learning and renewable energy costs: implications for US renewable energy policy. *Energy Policy* **2006**, *34* (13), 1645-1658.

(5) EIA, U. *Monthly Energy Review - Jan 2021*; Energy Information Administration, US 2021.

(6) Naqvi, M.; Yan, J. First-generation biofuels. *Handbook of clean energy systems* **2015**, 1-18.

(7) Wheals, A. E.; Basso, L. C.; Alves, D. M.; Amorim, H. V. Fuel ethanol after 25 years. *Trends Biotechnol.* **1999**, *17* (12), 482-487.

(8) Naylor, R. L.; Liska, A. J.; Burke, M. B.; Falcon, W. P.; Gaskell, J. C.; Rozelle, S. D.; Cassman, K. G. The ripple effect: biofuels, food security, and the environment. *Environment* **2007**, *49* (9), 30-43.

(9) Sun, Y.; Cheng, J. Hydrolysis of lignocellulosic materials for ethanol production: a review. *Bioresour. Technol.* **2002**, *83* (1), 1-11.

(10) Hill, C. A. *Wood modification: chemical, thermal and other processes*; John Wiley & Sons, 2007.

(11) Carriquiry, M. A.; Du, X.; Timilsina, G. R. Second generation biofuels: Economics and policies. *Energy Policy* **2011**, *39* (7), 4222-4234.

(12) Stürmer, B. Feedstock change at biogas plants–Impact on production costs. *Biomass Bioenergy* **2017**, *98*, 228-235.

(13) Thompson, W.; Whistance, J.; Meyer, S. Effects of US biofuel policies on US and world petroleum product markets with consequences for greenhouse gas emissions. *Energy Policy* **2011**, *39* (9), 5509-5518.

(14) Sims, R. E. H.; Mabee, W.; Saddler, J. N.; Taylor, M. An overview of second generation biofuel technologies. *Bioresour. Technol.* **2010**, *101* (6), 1570-1580.

(15) Bridgwater, A. V. Renewable fuels and chemicals by thermal processing of biomass. *Chem. Eng. J.* **2003**, *91* (2-3), 87-102.

(16) Perlack, R. D. *Biomass as Feedstock for a Bioenergy and Bioproducts Industry: The Technical Feasibility of a Billion-Ton Annual Supply*; Oak Ridge National Laboratory, 2005.

(17) Hutchins, S.; Dyer, J. USDA Agriculture Innovation Agenda Targets the Solutions of Tomorrow. *CSA News* **2020**.
(18) USDA. (2020). *USDA Agriculture Innovation Agenda*. Washington, D.C.
(19) Hallac, B. B.; Ragauskas, A. J. Analyzing cellulose degree of polymerization and its relevancy to cellulosic ethanol. *Biofuel Bioprod Biorefin* **2011**, *5* (2), 215-225.
(20) Puri, V. P. Effect of crystallinity and degree of polymerization of cellulose on enzymatic saccharification. *Biotechnol. Bioeng.* **1984**, *26* (10), 1219-1222.
(21) Carere, C. R.; Sparling, R.; Cicek, N.; Levin, D. B. Third generation biofuels via direct cellulose fermentation. *Int. J. Mol. Sci.* **2008**, *9* (7), 1342-1360.
(22) McMillan, J. D. Pretreatment of lignocellulosic biomass. In *Enzymatic Conversion of Biomass for Fuels Production*, ACS Symposium Series, ACS Publications, 1994; pp 292-324.
(23) Yu, J.; Paterson, N.; Blamey, J.; Millan, M. Cellulose, xylan and lignin interactions during pyrolysis of lignocellulosic biomass. *Fuel* **2017**, *191*, 140-149.
(24) Kuhad, R. C.; Singh, A.; Eriksson, K.-E. L. Microorganisms and enzymes involved in the degradation of plant fiber cell walls. In *Biotechnology in the pulp and paper industry*, Advances in Biochemical Engineering/Biotechnology, Vol. 57; Springer, 2006; pp 45-125.
(25) Silveira, R. L.; Stoyanov, S. R.; Gusarov, S.; Skaf, M. S.; Kovalenko, A. Plant biomass recalcitrance: effect of hemicellulose composition on nanoscale forces that control cell wall strength. *Journal of the American Chemical Society* **2013**, *135* (51), 19048-19051.
(26) Laureano-Perez, L.; Teymouri, F.; Alizadeh, H.; Dale, B. E. Understanding factors that limit enzymatic hydrolysis of biomass. *Appl. Biochem. Biotechnol.* **2005**, *124* (1-3), 1081-1099.
(27) Kumagai, A.; Endo, T. Effects of hemicellulose composition and content on the interaction between cellulose nanofibers. *Cellulose* **2021**, *28* (1), 259-271.
(28) Hatakeyama, H.; Hatakeyama, T. Lignin structure, properties, and applications. *Biopolymers* **2009**, 1-63.
(29) Ralph, J.; Lapierre, C.; Boerjan, W. Lignin structure and its engineering. *Curr. Opin. Biotechnol.* **2019**, *56*, 240-249.
(30) Hu, T. Q. *Characterization of lignocellulosic materials*; Blackwell, 2008.
(31) Pérez, J.; Munoz-Dorado, J.; De la Rubia, T.; Martinez, J. Biodegradation and biological treatments of cellulose, hemicellulose and lignin: an overview. *Int. Microbiol.* **2002**, *5* (2), 53-63.

(32) Chakar, F. S.; Ragauskas, A. J. Review of current and future softwood kraft lignin process chemistry. *Ind. Crops Prod.* **2004**, *20* (2), 131-141.
(33) Tu, W.-C.; Hallett, J. P. Recent advances in the pretreatment of lignocellulosic biomass. *Curr. Opin. Green Sustain. Chem.* **2019**, *20*, 11-17.
(34) McKendry, P. Energy production from biomass (part 1): overview of biomass. *Bioresour. Technol.* **2002**, *83* (1), 37-46.
(35) Rowell, R. M. *Handbook of wood chemistry and wood composites*; CRC press, 2012.
(36) Parmar, K. Biomass-An overview on composition characteristics and properties. *Int. J. Appl. Sci.* **2017**, *7* (1), 42-51.
(37) Huber, G. W.; Dumesic, J. A. An overview of aqueous-phase catalytic processes for production of hydrogen and alkanes in a biorefinery. *Catal. Today* **2006**, *111* (1-2), 119-132.
(38) Brandt, A.; Gräsvik, J.; Hallett, J. P.; Welton, T. Deconstruction of lignocellulosic biomass with ionic liquids. *Green Chem.* **2013**, *15* (3), 550-583.
(39) Côté, W. A. *Wood ultrastructure: an atlas of electron micrographs*; University of Washington press, 1967.
(40) Himmel, M. E.; Ding, S.-Y.; Johnson, D. K.; Adney, W. S.; Nimlos, M. R.; Brady, J. W.; Foust, T. D. Biomass recalcitrance: engineering plants and enzymes for biofuels production. *Science* **2007**, *315* (5813), 804-807.
(41) Wang, S.; Dai, G.; Yang, H.; Luo, Z. Lignocellulosic biomass pyrolysis mechanism: a state-of-the-art review. *Prog. Energy Combust. Sci.* **2017**, *62*, 33-86.
(42) Bajpai, P. Structure of lignocellulosic biomass. In *Pretreatment of lignocellulosic biomass for biofuel production*, Springer, 2016; pp 7-12.
(43) Cai, J.; He, Y.; Yu, X.; Banks, S. W.; Yang, Y.; Zhang, X.; Yu, Y.; Liu, R.; Bridgwater, A. V. Review of physicochemical properties and analytical characterization of lignocellulosic biomass. *Renew. Sust. Energ. Rev.* **2017**, *76*, 309-322.
(44) Elliott, D. C.; Beckman, D.; Bridgwater, A. V.; Diebold, J. P.; Gevert, S. B.; Solantausta, Y. Developments in direct thermochemical liquefaction of biomass: 1983-1990. *Energy Fuels* **1991**, *5* (3), 399-410.
(45) Bridgwater, A. V. Review of fast pyrolysis of biomass and product upgrading. *Biomass Bioenergy* **2012**, *38*, 68-94.
(46) Patel, M.; Zhang, X.; Kumar, A. Techno-economic and life cycle assessment on lignocellulosic biomass thermochemical conversion technologies: A review. *Renew. Sust. Energ. Rev.* **2016**, *53*, 1486-1499.

(47) Dutta, A.; Sahir, A.; Tan, E.; Humbird, D.; Snowden-Swan, L. J.; Meyer, P. A.; Ross, J.; Sexton, D.; Yap, R.; Lukas, J. *Process design and economics for the conversion of lignocellulosic biomass to hydrocarbon fuels: Thermochemical research pathways with in situ and ex situ upgrading of fast pyrolysis vapors*; Pacific Northwest National Lab.(PNNL), Richland, WA (United States), 2015.
(48) Hess, J. R.; Wright, C. T.; Kenney, K. L. Cellulosic biomass feedstocks and logistics for ethanol production. *Biofuels, Bioprod. Bioref.* **2007**, *1* (3), 181-190.
(49) Cummer, K. R.; Brown, R. C. Ancillary equipment for biomass gasification. *Biomass Bioenergy* **2002**, *23* (2), 113-128.
(50) Carson, J. W. Hopper/bin design. In *Bulk Solids Handling: Equipment Selection and Operation*, D. McGlinchey Ed.; Wiley Online Library, 2008; pp 68-98.
(51) Prescott, J. K.; Barnum, R. A. On powder flowability. *Pharm. Technol.* **2000**, *24* (10), 60-85.
(52) Polizzi, M. A.; Franchville, J.; Hilden, J. L. Assessment and predictive modeling of pharmaceutical powder flow behavior in small-scale hoppers. *Powder Technol.* **2016**, *294*, 30-42.
(53) Johanson, K. Rathole stability analysis for aerated powder materials. *Powder Technol.* **2004**, *141* (1-2), 161-170.
(54) Cheng, Z.; Leal, J. H.; Hartford, C. E.; Carson, J. W.; Donohoe, B. S.; Craig, D. A.; Xia, Y.; Daniel, R. C.; Ajayi, O. O.; Semelsberger, T. A. Flow behavior characterization of biomass Feedstocks. *Powder Technol.* **2021**, *387*, 156-180.
(55) Hsiao, W.-K.; Hörmann, T. R.; Toson, P.; Paudel, A.; Ghiotti, P.; Stauffer, F.; Bauer, F.; Lakio, S.; Behrend, O.; Maurer, R. Feeding of particle-based materials in continuous solid dosage manufacturing: a material science perspective. *Drug Discov. Today* **2020**, *25* (4), 800-806.
(56) Miao, Z.; Grift, T. E.; Hansen, A. C.; Ting, K. C. Flow performance of ground biomass in a commercial auger. *Powder Technol.* **2014**, *267*, 354-361.
(57) Olanrewaju, T. O. Design and fabrication of a screw conveyor. *Agric. Eng.* **2017**, *19* (3), 156-162.
(58) Campuzano, F.; Brown, R. C.; Martínez, J. D. Auger reactors for pyrolysis of biomass and wastes. *Renew. Sust. Energ. Rev.* **2019**, *102*, 372-409.
(59) De Meyer, A.; Cattrysse, D.; Rasinmäki, J.; Van Orshoven, J. Methods to optimise the design and management of biomass-for-bioenergy supply chains: A review. *Renew. Sust. Energ. Rev.* **2014**, *31*, 657-670.

(60) Caputo, A. C.; Palumbo, M.; Pelagagge, P. M.; Scacchia, F. Economics of biomass energy utilization in combustion and gasification plants: effects of logistic variables. *Biomass Bioenergy* **2005**, *28* (1), 35-51.
(61) Wang, X.; Leng, W.; Nayanathara, R. M. O.; Milsted, D.; Eberhardt, T. L.; Zhang, Z.; Zhang, X. Recent advances in transforming agricultural biorefinery lignins into value-added products. *J. Agric. Res.* **2023**, 100545.
(62) Merrow, E. W.; Phillips, K.; Myers, C. W. *Understanding cost growth and performance shortfalls in pioneer process plants*; Rand Corporation, 1981.
(63) Byun, J.; Han, J. Sustainable development of biorefineries: integrated assessment method for co-production pathways. *Energy Environ. Sci.* **2020**, *13* (8), 2233-2242.
(64) Muzzio, F. J.; Shinbrot, T.; Glasser, B. J. Powder technology in the pharmaceutical industry: the need to catch up fast. *Powder Technol.* **2002**.
(65) Wibowo, C.; Ng, K. M. Operational issues in solids processing plants: Systems view. *AIChE J.* **2001**, *47* (1), 107-125.
(66) Lan, K.; Park, S.; Kelley, S. S.; English, B. C.; Yu, T. H. E.; Larson, J.; Yao, Y. Impacts of uncertain feedstock quality on the economic feasibility of fast pyrolysis biorefineries with blended feedstocks and decentralized preprocessing sites in the Southeastern United States. *Glob. Change Biol. Bioenergy* **2020**, *12* (11), 1014-1029.
(67) Leuenberger, H.; Lanz, M. Pharmaceutical powder technology—from art to science: the challenge of the FDA's Process Analytical Technology initiative. *Adv. Powder Technol.* **2005**, *16* (1), 3-25.
(68) Zhao, Y.; Liu, M.; Wang, C.-H.; Matsusaka, S.; Yao, J. Electrostatics of granules and granular flows: A review. *Adv. Powder Technol.* **2023**, *34* (1), 103895.
(69) Wyman, C. E.; Dale, B. E.; Elander, R. T.; Holtzapple, M.; Ladisch, M. R.; Lee, Y. Coordinated development of leading biomass pretreatment technologies. *Bioresour. Technol.* **2005**, *96* (18), 1959-1966.
(70) Yue, D.; You, F.; Snyder, S. W. Biomass-to-bioenergy and biofuel supply chain optimization: overview, key issues and challenges. *Comput. Chem. Eng.* **2014**, *66*, 36-56.
(71) Rentizelas, A. A.; Tolis, A. J.; Tatsiopoulos, I. P. Logistics issues of biomass: the storage problem and the multi-biomass supply chain. *Renew. Sust. Energ. Rev.* **2009**, *13* (4), 887-894.
(72) Ray, A. E.; Williams, C. L.; Hoover, A. N.; Li, C.; Sale, K. L.; Emerson, R. M.; Klinger, J.; Oksen, E.; Narani, A.; Yan, J. Multiscale Characterization of

Lignocellulosic Biomass Variability and Its Implications to Preprocessing and Conversion: a Case Study for Corn Stover. *ACS Sustain. Chem. Eng.* **2020**, *8* (8), 3218-3230.
(73) Oyedeji, O.; Daw, C. S.; Labbe, N.; Ayers, P.; Abdoulmoumine, N. Kinetics of the release of elemental precursors of syngas and syngas contaminants during devolatilization of switchgrass. *Bioresour. Technol.* **2017**, *244*, 525-533. DOI: 10.1016/j.biortech.2017.07.167.
(74) Guo, Y.; Curtis, J. S. Discrete element method simulations for complex granular flows. *Annu. Rev. Fluid Mech.* **2015**, *47*, 21-46.
(75) Yan, J.; Oyedeji, O.; Leal, J. H.; Donohoe, B. S.; Semelsberger, T. A.; Li, C.; Hoover, A. N.; Webb, E.; Bose, E.; Zeng, Y. Characterizing variability in lignocellulosic biomass-A review. *ACS Sustain. Chem. Eng.* **2020**, *8* (22), 8059–8085. DOI: https://doi.org/10.1021/acssuschemeng.9b06263.
(76) Knowlton, T. M.; Klinzing, G.; Yang, W.; Carson, J. The importance of storage, transfer, and collection. *Chem. Eng. Prog.* **1994**, *90* (4).
(77) Wang, Z.; Ganewatta, M. S.; Tang, C. Sustainable polymers from biomass: Bridging chemistry with materials and processing. *Prog. Polym. Sci.* **2020**, *101*, 101197.
(78) Kolymbas, D. *Introduction to Hypoplasticity: Advances in Geotechnical Engineering and Tunnelling 1*; CRC Press, 2014.
(79) Wensrich, C.; Stratton, R. Shock waves in granular materials: Discrete and continuum comparisons. *Powder Technol.* **2011**, *210* (3), 288-292.
(80) Zhang, Z. P.; Liu, L. F.; Yuan, Y. D.; Yu, A. B. A simulation study of the effects of dynamic variables on the packing of spheres. *Powder Technol.* **2001**, *116* (1), 23-32.
(81) Cleary, P. W.; Sawley, M. L. DEM modelling of industrial granular flows: 3D case studies and the effect of particle shape on hopper discharge. *Appl. Math. Model.* **2002**, *26* (2), 89-111.
(82) Cundall, P. A.; Strack, O. D. A discrete numerical model for granular assemblies. *Geotechnique* **1979**, *29* (1), 47-65.
(83) Cleary, P. W. DEM prediction of industrial and geophysical particle flows. *Particuology* **2010**, *8* (2), 106-118.
(84) Tanida, K.-i.; Honda, K.; Kawano, N.; Kawaguchi, T.; Tanaka, T.; Tsuji, Y. Particle motion in screw feeder simulated by discrete element method. In *NIP & Digital Fabrication Conference*, 1998; Society for Imaging Science and Technology: pp 429-431.
(85) Shimizu, Y.; Cundall, P. A. Three-dimensional DEM simulations of bulk handling by screw conveyors. *J. Eng. Mech.* **2001**, *127* (9), 864-872.

(86) Qi, F.; Heindel, T. J.; Wright, M. M. Numerical study of particle mixing in a lab-scale screw mixer using the discrete element method. *Powder Technol.* **2017**, *308*, 334-345.
(87) Anand, A.; Curtis, J. S.; Wassgren, C. R.; Hancock, B. C.; Ketterhagen, W. R. Predicting discharge dynamics from a rectangular hopper using the discrete element method (DEM). *Chem. Eng. Sci.* **2008**, *63* (24), 5821-5830.
(88) Tao, H.; Jin, B.; Zhong, W.; Wang, X.; Ren, B.; Zhang, Y.; Xiao, R. Discrete element method modeling of non-spherical granular flow in rectangular hopper. *Chem. Eng. Process.: Process Intensif.* **2010**, *49* (2), 151-158.
(89) Höhner, D.; Wirtz, S.; Scherer, V. A study on the influence of particle shape on the mechanical interactions of granular media in a hopper using the Discrete Element Method. *Powder Technol.* **2015**, *278*, 286-305.
(90) Guo, Y.-c.; Wang, S.; Hu, K.; Li, D.-y. Optimizing the pipe diameter of the pipe belt conveyor based on discrete element method. *3D Res.* **2016**, *7* (1), 5.
(91) Krause, F.; Katterfeld, A. Usage of the discrete element method in conveyor technologies. *Institute for Conveyor Technologies (IFSL), The Otto-von-Guericke-University of Magdeburg, PO Box* **2010**, *4120*.
(92) Guo, Y.; Chen, Q.; Xia, Y.; Westover, T.; Eksioglu, S.; Roni, M. Discrete element modeling of switchgrass particles under compression and rotational shear. *Biomass Bioenergy* **2020**, *141*, 105649.
(93) Kaliyan, N.; Morey, R. V. Constitutive model for densification of corn stover and switchgrass. *Biosys. Eng.* **2009**, *104* (1), 47-63.
(94) Xia, Y.; Lai, Z.; Westover, T.; Klinger, J.; Huang, H.; Chen, Q. Discrete element modeling of deformable pinewood chips in cyclic loading test. *Powder Technol.* **2019**, *345*, 1-14.
(95) Pachón-Morales, J.; Perré, P.; Casalinho, J.; Do, H.; Schott, D.; Puel, F.; Colin, J. Potential of DEM for investigation of non-consolidated flow of cohesive and elongated biomass particles. *Adv. Powder Technol.* **2020**, *31* (4), 1500-1515.
(96) Shinbrot, T.; LaMarche, K.; Glasser, B. J. Triboelectrification and razorbacks: geophysical patterns produced in dry grains. *Phys. Rev. Lett.* **2006**, *96* (17), 178002.
(97) Bridgwater, J. The dynamics of granular materials–towards grasping the fundamentals. *Granul. Matter* **2003**, *4* (4), 175-181.
(98) Escotet-Espinoza, M. S.; Foster, C. J.; Ierapetritou, M. Discrete Element Modeling (DEM) for mixing of cohesive solids in rotating cylinders. *Powder Technol.* **2018**, *335*, 124-136.

(99) Rhodes, M. J. *Principles of powder technology*; John Wiley and Sons Inc., 1990.
(100) Faqih, A.; Chaudhuri, B.; Alexander, A. W.; Davies, C.; Muzzio, F. J.; Tomassone, M. S. An experimental/computational approach for examining unconfined cohesive powder flow. *Int. J. Pharm.* **2006**, *324* (2), 116-127.
(101) Jop, P.; Forterre, Y.; Pouliquen, O. A constitutive law for dense granular flows. *Nature* **2006**, *441* (7094), 727-730.
(102) Chevoir, F.; Prochnow, M.; Jenkins, J. T.; Mills, P. Dense granular flows down an inclined plane. In *Powders and grains 2001*, CRC Press, 2020; pp 373-376.
(103) El-Emam, M. A.; Zhou, L.; Shi, W.; Han, C.; Bai, L.; Agarwal, R. Theories and applications of CFD–DEM coupling approach for granular flow: A review. *Arch. Comput. Methods Eng.* **2021**, 1-42.
(104) Blau, P. The significance and use of the friction coefficient. *Tribol. Int.* **2001**, *34* (9), 585-591.
(105) Zhou, Y.; Wright, B.; Yang, R.; Xu, B. H.; Yu, A.-B. Rolling friction in the dynamic simulation of sandpile formation. *Physica A* **1999**, *269* (2-4), 536-553.
(106) Jenike, A. W. S., R.T. . On the plastic flow of Coulomb solids beyond original failure. *J Appl Mech* **1959**, *81*, 599-602.
(107) Weir, G. J. A mathematical model for dilating, non-cohesive granular flows in steep-walled hoppers. *Chem. Eng. Sci.* **2004**, *59* (1), 149-161. DOI: https://doi.org/10.1016/j.ces.2003.09.031.
(108) Jenike, A. Steady gravity flow of frictional-cohesive solids in converging channels. *J Appl Mech* **1964**, *31*, 5-11.
(109) Terzaghi, K. *Theoretical Soil Mechanics*; John Wiley & Sons, 1943.
(110) Rackl, M.; Grötsch, F. E.; Günthner, W. A. Angle of repose revisited: When is a heap a cone? In *EPJ Web of Conferences*, 2017; EDP Sciences: Vol. 140, p 02002.
(111) Pohlman, N. A.; Severson, B. L.; Ottino, J. M.; Lueptow, R. M. Surface roughness effects in granular matter: Influence on angle of repose and the absence of segregation. *Phys. Rev. E: Stat. Phys., Plasmas, Fluids,* **2006**, *73* (3), 031304.
(112) Lambe, T. W.; Whitman, R. V. *Soil Mechanics, SI Version (Series in Soil Engineering)*; John Wiley & Sons, 1969.
(113) Carr, R. *Gas–solids handling in the processing industries: Powder and granule properties and mechanics*; Marcel Dekker, 1976.
(114) Youness, D.; Hosseinpoor, M.; Yahia, A.; Tagnit-Hamou, A. Flowability characteristics of dry supplementary cementitious materials using Carr

measurements and their effect on the rheology of suspensions. *Powder Technol.* **2021**, *378*, 124-144.
(115) Lajeunesse, E.; Mangeney-Castelnau, A.; Vilotte, J. Spreading of a granular mass on a horizontal plane. *Phys. Fluids* **2004**, *16* (7), 2371-2381.
(116) Briend, R.; Radziszewski, P.; Pasini, D. Virtual soil calibration for wheel–soil interaction simulations using the discrete-element method. *Can. Aeronaut. Space J.* **2011**, *57* (1), 59-64.
(117) Derakhshani, S. M.; Schott, D. L.; Lodewijks, G. Micro–macro properties of quartz sand: Experimental investigation and DEM simulation. *Powder Technol.* **2015**, *269*, 127-138.
(118) Johnston, L. J.; Goihl, J.; Shurson, G. C. Selected additives did not improve flowability of DDGS in commercial systems. *Appl. Eng. Agric.* **2009**, *25* (1), 75-82.
(119) Cho, G.-C.; Dodds, J.; Santamarina, J. C. Particle shape effects on packing density, stiffness, and strength: natural and crushed sands. *J. Geotech. Geoenviron. Eng.* **2006**, *132* (5), 591-602.
(120) Fowler, R. T.; Wyatt, F. A. The effect of moisture content on the angle of repose of granular solids. *Aust. J. Chem.* **1960**, *1*, 5-8.
(121) Mellmann, J. The transverse motion of solids in rotating cylinders—forms of motion and transition behavior. *Powder Technol.* **2001**, *118* (3), 251-270. DOI: https://doi.org/10.1016/S0032-5910(00)00402-2.
(122) Al-Hashemi, H. M. B.; Al-Amoudi, O. S. B. A review on the angle of repose of granular materials. *Powder Technol.* **2018**, *330*, 397-417.
(123) Freeman, R. Measuring the flow properties of consolidated, conditioned and aerated powders—a comparative study using a powder rheometer and a rotational shear cell. *Powder Technol.* **2007**, *174* (1-2), 25-33.
(124) Ghadiri, M.; Ning, Z.; Kenter, S. J.; Puik, E. Attrition of granular solids in a shear cell. *Chem. Eng. Sci.* **2000**, *55* (22), 5445-5456.
(125) Salehi, H.; Barletta, D.; Poletto, M. A comparison between powder flow property testers. *Particuology* **2017**, *32*, 10-20.
(126) Koynov, S.; Wang, Y.; Redere, A.; Amin, P.; Emady, H. N.; Muzzio, F. J.; Glasser, B. J. Measurement of the axial dispersion coefficient of powders in a rotating cylinder: dependence on bulk flow properties. *Powder Technol.* **2016**, *292*, 298-306.
(127) ASTM, I. *D6773-16: Standard shear test method for bulk solids using the Schulze ring shear tester*; West Conshohocken, PA, 2016. DOI: 10.1520/D6773-16.
(128) Koynov, S.; Glasser, B.; Muzzio, F. Comparison of three rotational shear cell testers: Powder flowability and bulk density. *Powder Technol.* **2015**, *283*, 103-112.

(129) Vasilenko, A.; Koynov, S.; Glasser, B. J.; Muzzio, F. J. Role of consolidation state in the measurement of bulk density and cohesion. *Powder Technol.* **2013**, *239*, 366-373.
(130) Wang, Y.; Koynov, S.; Glasser, B. J.; Muzzio, F. J. A method to analyze shear cell data of powders measured under different initial consolidation stresses. *Powder Technol.* **2016**, *294*, 105-112.
(131) Johnson, P. C.; Jackson, R. Frictional–collisional constitutive relations for granular materials, with application to plane shearing. *J. Fluid Mech.* **1987**, *176*, 67-93.
(132) Nemat-Nasser, S. A micromechanically-based constitutive model for frictional deformation of granular materials. *J. Mech. Phys. Solids* **2000**, *48* (6-7), 1541-1563.
(133) Tomme, P.; Warren, R. A. J.; Gilkes, N. R. Cellulose hydrolysis by bacteria and fungi. *Adv. Microb. Physiol.* **1995**, *37*, 1-81.
(134) Martínez, Á. T.; Speranza, M.; Ruiz-Dueñas, F. J.; Ferreira, P.; Camarero, S.; Guillén, F.; Martínez, M. J.; Gutiérrez Suárez, A.; Río Andrade, J. C. d. Biodegradation of lignocellulosics: microbial, chemical, and enzymatic aspects of the fungal attack of lignin. *Int. Microbiol.* **2005**, *8* (3), 195-204.
(135) Bhandari, N.; Macdonald, D. G.; Bakhshi, N. N. Kinetic studies of corn stover saccharification using sulphuric acid. *Biotechnol. Bioeng.* **1984**, *26* (4), 320-327.
(136) Mishima, D.; Tateda, M.; Ike, M.; Fujita, M. Comparative study on chemical pretreatments to accelerate enzymatic hydrolysis of aquatic macrophyte biomass used in water purification processes. *Bioresour. Technol.* **2006**, *97* (16), 2166-2172.
(137) Yildiz, S.; Gezer, E. D.; Yildiz, U. C. Mechanical and chemical behavior of spruce wood modified by heat. *Build. Environ.* **2006**, *41* (12), 1762-1766.
(138) Bergander, A.; Salmén, L. Cell wall properties and their effects on the mechanical properties of fibers. *J. Mater. Sci.* **2002**, *37* (1), 151-156.
(139) Saha, P.; Manna, S.; Chowdhury, S. R.; Sen, R.; Roy, D.; Adhikari, B. Enhancement of tensile strength of lignocellulosic jute fibers by alkali-steam treatment. *Bioresour. Technol.* **2010**, *101* (9), 3182-3187.
(140) Leppänen, K.; Spetz, P.; Pranovich, A.; Hartonen, K.; Kitunen, V.; Ilvesniemi, H. Pressurized hot water extraction of Norway spruce hemicelluloses using a flow-through system. *Wood Sci. Technol.* **2011**, *45* (2), 223-236.
(141) Liu, Q.; Labbé, N.; Adhikari, S.; Chmely, S. C.; Abdoulmoumine, N. Hot water extraction as a pretreatment for reducing syngas inorganics impurities–A parametric investigation on switchgrass and loblolly pine bark. *Fuel* **2018**, *220*, 177-184.

(142) Wan, C.; Li, Y. Effect of hot water extraction and liquid hot water pretreatment on the fungal degradation of biomass feedstocks. *Bioresour. Technol.* **2011**, *102* (20), 9788-9793.
(143) Auxenfans, T.; Crônier, D.; Chabbert, B.; Paës, G. Understanding the structural and chemical changes of plant biomass following steam explosion pretreatment. *Biotechnol. Biofuels* **2017**, *10* (1), 1-16.
(144) Ballesteros, I.; Oliva, J. M.; Navarro, A. A.; Gonzalez, A.; Carrasco, J.; Ballesteros, M. Effect of chip size on steam explosion pretreatment of softwood. In *Twenty-First Symposium on Biotechnology for Fuels and Chemicals*, 2000, 2000; Springer: pp 97-110.
(145) Lizasoain, J.; Trulea, A.; Gittinger, J.; Kral, I.; Piringer, G.; Schedl, A.; Nilsen, P. J.; Potthast, A.; Gronauer, A.; Bauer, A. Corn stover for biogas production: effect of steam explosion pretreatment on the gas yields and on the biodegradation kinetics of the primary structural compounds. *Bioresour. Technol.* **2017**, *244*, 949-956.
(146) Terry, S. A.; Ribeiro, G. O.; Conrad, C. C.; Beauchemin, K. A.; McAllister, T. A.; Gruninger, R. J. Pretreatment of crop residues by ammonia fiber expansion (AFEX) alters the temporal colonization of feed in the rumen by rumen microbes. *FEMS Microbiol. Ecol.* **2020**, *96* (6), fiaa074.
(147) Zhao, C.; Qiao, X.; Cao, Y.; Shao, Q. Application of hydrogen peroxide presoaking prior to ammonia fiber expansion pretreatment of energy crops. *Fuel* **2017**, *205*, 184-191.
(148) Nieder-Heitmann, M.; Haigh, K.; Louw, J.; Görgens, J. F. Economic evaluation and comparison of succinic acid and electricity co-production from sugarcane bagasse and trash lignocelluloses in a biorefinery, using different pretreatment methods: dilute acid (H2SO4), alkaline (NaOH), organosolv, ammonia fibre expansion (AFEX™), steam explosion (STEX), and wet oxidation. *Biofuel Bioprod Biorefin* **2020**, *14* (1), 55-77.
(149) Kim, J. S.; Lee, Y. Y.; Kim, T. H. A review on alkaline pretreatment technology for bioconversion of lignocellulosic biomass. *Bioresour. Technol.* **2016**, *199*, 42-48.
(150) Gonzales, R. R.; Sivagurunathan, P.; Kim, S.-H. Effect of severity on dilute acid pretreatment of lignocellulosic biomass and the following hydrogen fermentation. *Int. J. Hydrogen Energy* **2016**, *41* (46), 21678-21684.
(151) Park, Y. C.; Kim, J. S. Comparison of various alkaline pretreatment methods of lignocellulosic biomass. *Energy* **2012**, *47* (1), 31-35.
(152) An, S.; Li, W.; Liu, Q.; Xia, Y.; Zhang, T.; Huang, F.; Lin, Q.; Chen, L. Combined dilute hydrochloric acid and alkaline wet oxidation pretreatment to improve sugar recovery of corn stover. *Bioresour. Technol.* **2019**, *271*, 283-288.

(153) Palonen, H.; Thomsen, A. B.; Tenkanen, M.; Schmidt, A. S.; Viikari, L. Evaluation of wet oxidation pretreatment for enzymatic hydrolysis of softwood. *Appl. Biochem. Biotechnol.* **2004**, *117* (1), 1-17.
(154) Srinivasan, N.; Ju, L.-K. Pretreatment of guayule biomass using supercritical carbon dioxide-based method. *Bioresour. Technol.* **2010**, *101* (24), 9785-9791.
(155) Gu, T.; Held, M. A.; Faik, A. Supercritical CO2 and ionic liquids for the pretreatment of lignocellulosic biomass in bioethanol production. *Environ. Technol.* **2013**, *34* (13-14), 1735-1749.
(156) Amidon, T. E.; Wood, C. D.; Shupe, A. M.; Wang, Y.; Graves, M.; Liu, S. Biorefinery: conversion of woody biomass to chemicals, energy and materials. *J Biobased Mater Bioenergy* **2008**, *2* (2), 100-120.
(157) Mante, O. D.; Amidon, T. E.; Stipanovic, A.; Babu, S. P. Integration of biomass pretreatment with fast pyrolysis: An evaluation of electron beam (EB) irradiation and hot-water extraction (HWE). *J. Anal. Appl. Pyrolysis* **2014**, *110*, 44-54.
(158) Wolf, M.; Berger, F.; Hanstein, S.; Weidenkaff, A.; Endreß, H.-U.; Oestreich, A. M.; Ebrahimi, M.; Czermak, P. Hot-Water Hemicellulose Extraction from Fruit Processing Residues. *ACS omega* **2022**, *7* (16), 13436-13447.
(159) Baldrian, P.; Valášková, V. Degradation of cellulose by basidiomycetous fungi. *FEMS Microbiol. Rev.* **2008**, *32* (3), 501-521.
(160) Goodell, B.; Qian, Y.; Jellison, J. Fungal decay of wood: soft rot—brown rot—white rot. In *Development of Commercial Wood Preservatives*, ACS Publications, 2008; pp 9-31.
(161) Arantes, V.; Goodell, B. Current understanding of brown-rot fungal biodegradation mechanisms: a review. In *Deterioration and protection of sustainable biomaterials*, ACS Publications, 2014; pp 3-21.
(162) Goodell, B.; Qian, Y.; Jellison, J.; Richard, M.; Qi, W. Lignocellulose oxidation by low molecular weight metal-binding compounds isolated from wood degrading fungi: A comparison of brown rot and white rot systems and the potential application of chelator-mediated Fenton reactions. *Prog. Biotechnol.* **2002**, *21*, 37-47.
(163) Arantes, V.; Milagres, A. M. F.; Filley, T. R.; Goodell, B. Lignocellulosic polysaccharides and lignin degradation by wood decay fungi: the relevance of nonenzymatic Fenton-based reactions. *J. Ind. Microbiol. Biotechnol.* **2011**, *38* (4), 541-555.
(164) Hastrup, A. C. S.; Howell, C.; Larsen, F. H.; Sathitsuksanoh, N.; Goodell, B.; Jellison, J. Differences in crystalline cellulose modification due to degradation by brown and white rot fungi. *Fungal Biol.* **2012**, *116* (10), 1052-1063.

(165) Bari, E.; Daniel, G.; Yilgor, N.; Kim, J. S.; Tajick-Ghanbary, M. A.; Singh, A. P.; Ribera, J. Comparison of the Decay Behavior of Two White-Rot Fungi in Relation to Wood Type and Exposure Conditions. *Microorganisms* **2020**, *8* (12), 1931.
(166) Janusz, G.; Pawlik, A.; Sulej, J.; Świderska-Burek, U.; Jarosz-Wilkołazka, A.; Paszczyński, A. Lignin degradation: microorganisms, enzymes involved, genomes analysis and evolution. *FEMS Microbiol. Rev.* **2017**, *41* (6), 941-962.
(167) Tuomela, M.; Hatakka, A.; Raiskila, S.; Vikman, M.; Itävaara, M. Biodegradation of radiolabelled synthetic lignin (14 C-DHP) and mechanical pulp in a compost environment. *Appl. Microbiol. Biotechnol.* **2001**, *55* (4), 492-499.
(168) Blanchette, R. A. Degradation of the lignocellulose complex in wood. *Can. J. Plant Sci.* **1995**, *73* (S1), 999-1010.
(169) Sivonen, H.; Nuopponen, M.; Maunu, S. L.; Sundholm, F.; Vuorinen, T. Carbon-thirteen cross-polarization magic angle spinning nuclear magnetic resonance and Fourier transform infrared studies of thermally modified wood exposed to brown and soft rot fungi. *Appl. Spectrosc.* **2003**, *57* (3), 266-273.
(170) Gamble, G. R.; Akin, D. E.; Makkar, H. P.; Becker, K. Biological degradation of tannins in sericea lespedeza (Lespedeza cuneata) by the white rot fungi Ceriporiopsis subvermispora and Cyathus stercoreus analyzed by solid-state 13C nuclear magnetic resonance spectroscopy. *Appl. Environ. Microbiol.* **1996**, *62* (10), 3600-3604.
(171) Gamble, G. R.; Sethuraman, A.; Akin, D. E.; Eriksson, K. E. Biodegradation of lignocellulose in Bermuda grass by white rot fungi analyzed by solid-state 13C nuclear magnetic resonance. *Appl. Environ. Microbiol.* **1994**, *60* (9), 3138-3144.
(172) Gilardi, G.; Abis, L.; Cass, A. E. G. Carbon-13 CP/MAS solid-state NMR and FT-IR spectroscopy of wood cell wall biodegradation. *Enzyme Microb. Technol.* **1995**, *17* (3), 268-275.
(173) Durmaz, S.; Özgenç, Ö.; Boyacı, İ. H.; Yıldız, Ü. C.; Erişir, E. Examination of the chemical changes in spruce wood degraded by brown-rot fungi using FT-IR and FT-Raman spectroscopy. *Vib. Spectrosc* **2016**, *85*, 202-207.
(174) González-Bautista, E.; Alarcón-Gutierrez, E.; Dupuy, N.; Gaime-Perraud, I.; Ziarelli, F.; Farnet-da-Silva, A.-M. Influence of yeast extract enrichment and Pycnoporus sanguineus inoculum on the dephenolisation of sugar-cane bagasse for production of second-generation ethanol. *Fuel* **2020**, *260*, 116370.

(175) Khatami, S.; Deng, Y.; Tien, M.; Hatcher, P. G. Formation of water-soluble organic matter through fungal degradation of lignin. *Org. Geochem.* **2019**, *135*, 64-70.
(176) Howell, C.; Hastrup, A. C. S.; Goodell, B.; Jellison, J. Temporal changes in wood crystalline cellulose during degradation by brown rot fungi. *International Biodeterioration & Biodegradation* **2009**, *63* (4), 414-419.
(177) Lee, J.-W.; Gwak, K.-S.; Park, J.-Y.; Park, M.-J.; Choi, D.-H.; Kwon, M.; Choi, I.-G. Biological pretreatment of softwood Pinus densiflora by three white rot fungi. *J. Microbiol.* **2007**, *45* (6), 485-491.
(178) Monrroy, M.; Ortega, I.; Ramírez, M.; Baeza, J.; Freer, J. Structural change in wood by brown rot fungi and effect on enzymatic hydrolysis. *Enzyme Microb. Technol.* **2011**, *49* (5), 472-477.
(179) Xu, G.; Wang, L.; Liu, J.; Wu, J. FTIR and XPS analysis of the changes in bamboo chemical structure decayed by white-rot and brown-rot fungi. *Appl. Surf. Sci.* **2013**, *280*, 799-805.
(180) Jaeger, H. M.; Nagel, S. R.; Behringer, R. P. Granular solids, liquids, and gases. *Rev. Mod. Phys.* **1996**, *68* (4), 1259-1273. DOI: 10.1103/RevModPhys.68.1259.
(181) Ottino, J.; Khakhar, D. Mixing and segregation of granular materials. *Annu. Rev. Fluid Mech.* **2000**, *32* (1), 55-91.
(182) Aranson, I. S.; Tsimring, L. S. Patterns and collective behavior in granular media: Theoretical concepts. *Rev. Mod. Phys.* **2006**, *78* (2), 641-692. DOI: 10.1103/RevModPhys.78.641.
(183) Bouchaud, J. P.; Claudin, P.; Levine, D.; Otto, M. Force chain splitting in granular materials: A mechanism for large-scale pseudo-elastic behaviour. *Eur. Phys. J. E Soft Matter* **2001**, *4* (4), 451-457.
(184) Tumuluru, J. S.; Wright, C. T.; Hess, J. R.; Kenney, K. L. A review of biomass densification systems to develop uniform feedstock commodities for bioenergy application. *Biofuel Bioprod Biorefin* **2011**, *5* (6), 683-707.
(185) Müller, C. R.; Davidson, J. F.; Dennis, J. S.; Fennell, P.; Gladden, L. F.; Hayhurst, A. N.; Mantle, M. D.; Rees, A.; Sederman, A. J. Real-time measurement of bubbling phenomena in a three-dimensional gas-fluidized bed using ultrafast magnetic resonance imaging. *Phys. Rev. Lett.* **2006**, *96* (15), 154504.
(186) Amini, J.; Sumantyo, J. T. S. Employing a method on SAR and optical images for forest biomass estimation. *IEEE Trans. Geosci. Remote Sens.* **2009**, *47* (12), 4020-4026.
(187) Zhu, H.; Zhou, Z.; Yang, R.; Yu, A. Discrete particle simulation of particulate systems: theoretical developments. *Chem. Eng. Sci.* **2007**, *62* (13), 3378-3396.

(188) Munjiza, A.; Cleary, P. W. Industrial particle flow modelling using discrete element method. *Eng. Comput.* **2009**.
(189) Wassgren, C.; Curtis, J. S. The application of computational modeling to pharmaceutical materials science. *MRS Bull.* **2006**, *31* (11), 900-904.
(190) Kriebitzsch, S. H. L.; van der Hoef, M. A.; Kuipers, J. A. M. Drag force in discrete particle models—Continuum scale or single particle scale? *AIChE J.* **2013**, *59* (1), 316-324. DOI: https://doi.org/10.1002/aic.13804.
(191) Wu, C.-Y. DEM simulations of die filling during pharmaceutical tabletting. *Particuology* **2008**, *6* (6), 412-418.
(192) Yeom, S. B.; Ha, E.-S.; Kim, M.-S.; Jeong, S. H.; Hwang, S.-J.; Choi, D. H. Application of the discrete element method for manufacturing process simulation in the pharmaceutical industry. *Pharmaceutics* **2019**, *11* (8), 414.
(193) Azmir, J.; Hou, Q.; Yu, A. CFD-DEM simulation of drying of food grains with particle shrinkage. *Powder Technol.* **2019**, *343*, 792-802.
(194) Tijskens, E.; Ramon, H.; De Baerdemaeker, J. Discrete element modelling for process simulation in agriculture. *J. Sound Vibrat.* **2003**, *266* (3), 493-514.
(195) Golshan, S.; Sotudeh-Gharebagh, R.; Zarghami, R.; Mostoufi, N.; Blais, B.; Kuipers, J. A. M. Review and implementation of CFD-DEM applied to chemical process systems. *Chem. Eng. Sci.* **2020**, *221*, 115646.
(196) Jovanović, A.; Pezo, M.; Pezo, L.; Lević, L. DEM/CFD analysis of granular flow in static mixers. *Powder Technol.* **2014**, *266*, 240-248.
(197) Xia, Y.; Stickel, J. J.; Jin, W.; Klinger, J. A review of computational models for the flow of milled biomass I: Discrete-particle models. *ACS Sustain. Chem. Eng.* **2020**, *8* (16), 6142–6156. DOI: https://doi.org/10.1021/acssuschemeng.0c00402.
(198) Ketterhagen, W. R.; Curtis, J. S.; Wassgren, C. R.; Kong, A.; Narayan, P. J.; Hancock, B. C. Granular segregation in discharging cylindrical hoppers: a discrete element and experimental study. *Chem. Eng. Sci.* **2007**, *62* (22), 6423-6439.
(199) Zhu, H.; Yu, A. A theoretical analysis of the force models in discrete element method. *Powder Technol.* **2006**, *161* (2), 122-129.
(200) Lee, H. V.; Hamid, S. B. A.; Zain, S. K. Conversion of lignocellulosic biomass to nanocellulose: structure and chemical process. *Sci. World J.* **2014**, *2014*.
(201) Agbor, V. B.; Cicek, N.; Sparling, R.; Berlin, A.; Levin, D. B. Biomass pretreatment: fundamentals toward application. *Biotechnology advances* **2011**, *29* (6), 675-685.

(202) Wensrich, C.; Katterfeld, A. Rolling friction as a technique for modelling particle shape in DEM. *Powder Technol.* **2012**, *217*, 409-417.
(203) Pazouki, A.; Serban, R.; Negrut, D. A high performance computing approach to the simulation of fluid-solid interaction problems with rigid and flexible components. *Arch. Mech. Eng.* **2014**, *61* (2), 227-251.
(204) Trubetskaya, A.; Leahy, J. J.; Yazhenskikh, E.; Müller, M.; Layden, P.; Johnson, R.; Ståhl, K.; Monaghan, R. F. D. Characterization of woodstove briquettes from torrefied biomass and coal. *Energy* **2019**, *171*, 853-865.
(205) Naderi, M. Surface Area: Brunauer–Emmett–Teller (BET). In *Progress in filtration and separation*, Elsevier, 2015; pp 585-608.
(206) Villarroel-Rocha, J.; Barrera, D.; Sapag, K. Introducing a self-consistent test and the corresponding modification in the Barrett, Joyner and Halenda method for pore-size determination. *Microporous Mesoporous Mater.* **2014**, *200*, 68-78.
(207) Ciesielski, P. N.; Crowley, M. F.; Nimlos, M. R.; Sanders, A. W.; Wiggins, G. M.; Robichaud, D.; Donohoe, B. S.; Foust, T. D. Biomass particle models with realistic morphology and resolved microstructure for simulations of intraparticle transport phenomena. *Energy Fuels* **2015**, *29* (1), 242-254.
(208) Lam, P. S.; Sokhansanj, S. Engineering properties of biomass. In *Engineering and Science of Biomass Feedstock Production and Provision*, Springer, 2014; pp 17-35.
(209) Guo, Y.; Liu, Q.; Li, Y.; Li, Z.; Jin, H.; Wassgren, C.; Curtis, J. S. Discrete element method models of elastic and elastoplastic fiber assemblies. *AIChE J.* **2021**, *67* (8), e17296. DOI: https://doi.org/10.1002/aic.17296.
(210) Acharjee, T. C.; Coronella, C. J.; Vasquez, V. R. Effect of thermal pretreatment on equilibrium moisture content of lignocellulosic biomass. *Bioresour. Technol.* **2011**, *102* (7), 4849-4854.
(211) Barakat, A.; Monlau, F.; Solhy, A.; Carrere, H. Mechanical dissociation and fragmentation of lignocellulosic biomass: Effect of initial moisture, biochemical and structural proprieties on energy requirement. *Appl. Energy* **2015**, *142*, 240-246.
(212) Yu, A. Discrete Element Method—An Effective Method for Particle Scale Research of Particulate Matter. *Eng. Comput.* **2004**, 205-214. DOI: 10.1108/02644400410519749.
(213) Zhu, H.; Yu, A. Steady-state granular flow in a three-dimensional cylindrical hopper with flat bottom: microscopic analysis. *J. Phys. D: Appl. Phys.* **2004**, *37* (10), 1497.
(214) Hoomans, B.; Kuipers, J.; Briels, W. J.; van Swaaij, W. P. M. Discrete particle simulation of bubble and slug formation in a two-dimensional gas-

fluidised bed: a hard-sphere approach. *Chem. Eng. Sci.* **1996**, *51* (1), 99-118.
(215) Richardson, D. C.; Walsh, K. J.; Murdoch, N.; Michel, P. Numerical simulations of granular dynamics: I. Hard-sphere discrete element method and tests. *Icarus* **2011**, *212* (1), 427-437.
(216) Murphy, E.; Subramaniam, S. Binary collision outcomes for inelastic soft-sphere models with cohesion. *Powder Technol.* **2017**, *305*, 462-476.
(217) Tangri, H.; Guo, Y.; Curtis, J. S. Hopper discharge of elongated particles of varying aspect ratio: Experiments and DEM simulations. *Chem. Eng. Sci.: X* **2019**, *4*, 100040.
(218) Stewart, R.; Bridgwater, J.; Zhou, Y.; Yu, A. Simulated and measured flow of granules in a bladed mixer—a detailed comparison. *Chem. Eng. Sci.* **2001**, *56* (19), 5457-5471.
(219) Fu, X.; Dutt, M.; Bentham, A. C.; Hancock, B. C.; Cameron, R. E.; Elliott, J. A. Investigation of particle packing in model pharmaceutical powders using X-ray microtomography and discrete element method. *Powder Technol.* **2006**, *167* (3), 134-140.
(220) Bizon, C.; Shattuck, M.; Swift, J.; McCormick, W.; Swinney, H. L. Patterns in 3D vertically oscillated granular layers: simulation and experiment. *Phys. Rev. Lett.* **1998**, *80* (1), 57.
(221) Jensen, R. P.; Bosscher, P. J.; Plesha, M. E.; Edil, T. B. DEM simulation of granular media—structure interface: effects of surface roughness and particle shape. *Int. J. Numer. Anal. Methods Geomech.* **1999**, *23* (6), 531-547.
(222) Falke, T.; de Payrebrune, K. M.; Kirchhof, S.; Kühnel, L.; Kühnel, R.; Mütze, T.; Kröger, M. An alternative DEM parameter identification procedure based on experimental investigation: A case study of a ring shear cell. *Powder Technol.* **2018**, *328*, 227-234.
(223) Boikov, A. V.; Savelev, R. V.; Payor, V. A. DEM calibration approach: implementing contact model. In *Journal of Physics: Conference Series*, 2018, 2018; IOP Publishing: Vol. 1050, p 012014.
(224) Horabik, J.; Molenda, M. Parameters and contact models for DEM simulations of agricultural granular materials: A review. *Biosys. Eng.* **2016**, *147*, 206-225.
(225) Burns, S. J.; Piiroinen, P. T.; Hanley, K. J. Critical time step for DEM simulations of dynamic systems using a Hertzian contact model. *Int. J. Numer. Methods Eng.* **2019**, *119* (5), 432-451.
(226) Bian, X.; Wang, G.; Wang, H.; Wang, S.; Lv, W. Effect of lifters and mill speed on particle behaviour, torque, and power consumption of a

tumbling ball mill: Experimental study and DEM simulation. *Miner. Eng.* **2017**, *105*, 22-35.
(227) Johnson, K. L. *Contact mechanics*; Cambridge university press, 1987.
(228) Greenwood, J.; Minshall, H.; Tabor, D. Hysteresis losses in rolling and sliding friction. *Proc. R. Soc. Lond. A* **1961**, *259* (1299), 480-507.
(229) Munjiza, A. A. *The combined finite-discrete element method*; John Wiley & Sons, 2004.
(230) Ai, J.; Chen, J.-F.; Rotter, J. M.; Ooi, J. Y. Assessment of rolling resistance models in discrete element simulations. *Powder Technol.* **2011**, *206* (3), 269-282.
(231) El-Kassem, B.; Salloum, N.; Brinz, T.; Heider, Y.; Markert, B. A multivariate regression parametric study on DEM input parameters of free-flowing and cohesive powders with experimental data-based validation. *Comput. Part. Mech.* **2020**, 1-25.
(232) Vu-Quoc, L.; Zhang, X. An elastoplastic contact force–displacement model in the normal direction: displacement–driven version. In *Proceedings of the Royal Society of London A: Mathematical, Physical and Engineering Sciences*, 1999; The Royal Society: Vol. 455, pp 4013-4044.
(233) LoCurto, G.; Zhang, X.; Zakirov, V.; Bucklin, R.; Vu-Quoc, L.; Hanes, D.; Walton, O. Soybean impacts: experiments and dynamic simulations. *Trans. ASAE* **1997**, *40* (3), 789-794.
(234) Benvenuti, L.; Kloss, C.; Pirker, S. Identification of DEM simulation parameters by Artificial Neural Networks and bulk experiments. *Powder Technol.* **2016**, *291*, 456-465.
(235) Marigo, M.; Cairns, D.; Bowen, J.; Ingram, A.; Stitt, E. Relationship between single and bulk mechanical properties for zeolite ZSM5 spray-dried particles. *Particuology* **2014**, *14*, 130-138.
(236) Fasina, O. Physical properties of peanut hull pellets. *Bioresour. Technol.* **2008**, *99* (5), 1259-1266.
(237) Tafesse, S.; Robison Fernlund, J. M.; Sun, W.; Bergholm, F. Evaluation of image analysis methods used for quantification of particle angularity. *Sedimentology* **2013**, *60* (4), 1100-1110.
(238) Xu, R.; Di Guida, O. A. Comparison of sizing small particles using different technologies. *Powder Technol.* **2003**, *132* (2-3), 145-153.
(239) Roostaei, M.; Hosseini, S. A.; Soroush, M.; Velayati, A.; Alkouh, A.; Mahmoudi, M.; Ghalambor, A.; Fattahpour, V. Comparison of Various Particle-Size Distribution-Measurement Methods. *SPE Reserv. Eval. Eng.* **2020**.
(240) Lam, P. S.; Sokhansanj, S.; Bi, X.; Lim, C. J. Effect of particle size and shape on physical properties of biomass grinds. In *2008 ASABE Annual*

International Meeting, Providence, Rhode Island, June 29–July 2, 2008; American Society of Agricultural and Biological Engineers.
(241) Zou, R. P.; Lin, X. Y.; Yu, A. B.; Wong, P. Packing of cylindrical particles with a length distribution. *J. Am. Ceram. Soc.* **1997**, *80* (3), 646-652.
(242) Podczeck, F.; Mia, Y. The influence of particle size and shape on the angle of internal friction and the flow factor of unlubricated and lubricated powders. *Int. J. Pharm.* **1996**, *144* (2), 187-194.
(243) Robinson, D.; Friedman, S. Observations of the effects of particle shape and particle size distribution on avalanching of granular media. *Physica A* **2002**, *311* (1-2), 97-110.
(244) Ganesan, V.; Rosentrater, K. A.; Muthukumarappan, K. Flowability and handling characteristics of bulk solids and powders–a review with implications for DDGS. *Biosys. Eng.* **2008**, *101* (4), 425-435.
(245) Hann, D.; Stražišar, J. Influence of particle size distribution, moisture content, and particle shape on the flow properties of bulk solids. *Instrum Sci. Technol.* **2007**, *35* (5), 571-584.
(246) Mani, S.; Tabil, L. G.; Sokhansanj, S. Grinding performance and physical properties of wheat and barley straws, corn stover and switchgrass. *Biomass Bioenergy* **2004**, *27* (4), 339-352.
(247) Tannous, K.; Lam, P.; Sokhansanj, S.; Grace, J. Physical properties for flow characterization of ground biomass from douglas fir wood. *Part. Sci. Technol.* **2013**, *31* (3), 291-300.
(248) Guo, Q.; Chen, X.; Liu, H. J. F. Experimental research on shape and size distribution of biomass particle. *Fuel* **2012**, *94*, 551-555.
(249) Igathinathane, C.; Melin, S.; Sokhansanj, S.; Bi, X.; Lim, C.; Pordesimo, L.; Columbus, E. Machine vision based particle size and size distribution determination of airborne dust particles of wood and bark pellets. *Powder Technol.* **2009**, *196* (2), 202-212.
(250) Fu, J.; Cheong, Y.; Reynolds, G.; Adams, M.; Salman, A.; Hounslow, M. An experimental study of the variability in the properties and quality of wet granules. *Powder Technol.* **2004**, *140* (3), 209-216.
(251) Oliver, M.; Matúš, Č.; Ľudmila, G.; Martin, J.; Radovan, R.; Peter, P. Dynamic Image Analysis to Determine Granule Size and Shape, for Selected High Shear Granulation Process Parameters. *Stroj. Cas.* **2019**, *69* (4), 57-64.
(252) Miao, Z.; Shastri, Y.; Grift, T. E.; Hansen, A. C.; Ting, K. Lignocellulosic biomass feedstock transportation alternatives, logistics, equipment configurations, and modeling. *Biofuel Bioprod Biorefin* **2012**, *6* (3), 351-362.
(253) Nelson, S. O. Density-permittivity relationships for powdered and granular materials. *IEEE Trans. Instrum. Meas.* **2005**, *54* (5), 2033-2040.

(254) Van Zuilichem, D. J.; Van Egmond, N. D.; De Swart, J. G. Density behaviour of flowing granular material. *Powder Technol.* **1974**, *10* (4-5), 161-169.
(255) Arnold, P.; Roberts, A. Fundamental aspects of load-deformation behavior of wheat grains. *Trans. ASAE* **1969**, *12* (1), 104-0108.
(256) Misra, R. N.; Young, J. H. A model for predicting the effect of moisture content on the modulus of elasticity of soybeans. *Trans. ASAE* **1981**, *24* (5), 1338-1341.
(257) Molenda, M.; Horabik, J. *Characterization of mechanical properties of particulate solids for storage and handling*; Institute of Agrophysics. Polish Academy of Science. Lublin, 2005.
(258) Shelef, L.; Mohsenin, N. Effect of moisture content on mechanical properties of shelled corn. *Cereal Chem.* **1969**, *46* (3), 242-253.
(259) Chung, Y.; Ooi, J.; Favier, J. Measurement of mechanical properties of agricultural grains for DE models. In *17th ASCE Engineering Mechanics Conference. Netwark, USA*, 2004.
(260) ASABE. *S368.4: Compression Test of Food Materials of Convex Shape*; 2022.
(261) Wiącek, J.; Molenda, M. Effect of particle size distribution on micro-and macromechanical response of granular packings under compression. *Int. J. Solids Struct.* **2014**, *51* (25-26), 4189-4195.
(262) Kloss, C.; Goniva, C.; Hager, A.; Amberger, S.; Pirker, S. Models, algorithms and validation for opensource DEM and CFD–DEM. *Prog. Comput. Fluid Dyn.* **2012**, *12* (2-3), 140-152.
(263) Ramírez, R.; Pöschel, T.; Brilliantov, N. V.; Schwager, T. Coefficient of restitution of colliding viscoelastic spheres. *Phys. Rev. E: Stat. Phys., Plasmas, Fluids,* **1999**, *60* (4), 4465.
(264) Ozturk, I.; Kara, M.; Uygan, F.; Kalkan, F. Restitution coefficient of chick pea and lentil seeds. *Int. Agrophysics* **2010**, *24* (2), 209-211.
(265) Hlosta, J.; Jezerská, L.; Rozbroj, J.; Žurovec, D.; Nečas, J.; Zegzulka, J. DEM Investigation of the Influence of Particulate Properties and Operating Conditions on the Mixing Process in Rotary Drums: Part 1—Determination of the DEM Parameters and Calibration Process. *Processes* **2020**, *8* (2), 222.
(266) Ramírez-Gómez, Á.; Gallego, E.; Fuentes, J. M.; González-Montellano, C.; Ayuga, F. Values for particle-scale properties of biomass briquettes made from agroforestry residues. *Particuology* **2014**, *12*, 100-106.
(267) Wong, C. X.; Daniel, M. C.; Rongong, J. A. Energy dissipation prediction of particle dampers. *J. Sound Vibrat.* **2009**, *319* (1), 91-118. DOI: https://doi.org/10.1016/j.jsv.2008.06.027.

(268) Azushima, A.; Kudo, H. Direct observation of contact behaviour to interpret the pressure dependence of the coefficient of friction in sheet metal forming. *CIRP Ann. - Manuf. Technol.* **1995**, *44* (1), 209-212.
(269) Raji, A. O.; Favier, J. F. Model for the deformation in agricultural and food particulate materials under bulk compressive loading using discrete element method. I: Theory, model development and validation. *J. Food Eng.* **2004**, *64* (3), 359-371.
(270) Shafaei, S. M.; Kamgar, S. A comprehensive investigation on static and dynamic friction coefficients of wheat grain with the adoption of statistical analysis. *J. Adv. Res.* **2017**, *8* (4), 351-361.
(271) ASTM, I. *D6128-16: Standard Test Method for Shear Testing of Bulk Solids Using the Jenike Shear Tester*; West Conshohocken, PA, 2016.
(272) Mohsenin, N. N. *Physical Properties of Plant and Animal Materials: v. 1: Physical Characteristics and Mechanical Properties*; Routledge, 1986.
(273) Stasiak, M.; Molenda, M.; Bańda, M.; Horabik, J.; Wiącek, J.; Parafiniuk, P.; Wajs, J.; Gancarz, M.; Gondek, E.; Lisowski, A. Friction and Shear Properties of Pine Biomass and Pellets. *Materials* **2020**, *13* (16), 3567.
(274) Jiang, M.; Yu, H.-S.; Harris, D. A novel discrete model for granular material incorporating rolling resistance. *Comput Geotech* **2005**, *32* (5), 340-357.
(275) Zhou, Y.; Xu, B. H.; Yu, A.-B.; Zulli, P. An experimental and numerical study of the angle of repose of coarse spheres. *Powder Technol.* **2002**, *125* (1), 45-54.
(276) Lattanzi, A. M.; Stickel, J. J. Hopper flows of mixtures of spherical and rod-like particles via the multisphere method. *AIChE J.* **2020**, *66* (4), e16882.
(277) Feng, Y. T.; Han, K.; Owen, D. R. J. Energy-conserving contact interaction models for arbitrarily shaped discrete elements. *Comput. Methods Appl. Mech. Eng.* **2012**, *205-208*, 169-177. DOI: https://doi.org/10.1016/j.cma.2011.02.010.
(278) Maione, R.; De Richter, S. K.; Mauviel, G.; Wild, G. DEM investigation of granular flow and binary mixture segregation in a rotating tumbler: Influence of particle shape and internal baffles. *Powder Technol.* **2015**, *286*, 732-739.
(279) Pasha, M.; Hare, C.; Ghadiri, M.; Gunadi, A.; Piccione, P. M. Effect of particle shape on flow in discrete element method simulation of a rotary batch seed coater. *Powder Technol.* **2016**, *296*, 29-36.
(280) Zhong, W.; Yu, A.; Liu, X.; Tong, Z.; Zhang, H. DEM/CFD-DEM modelling of non-spherical particulate systems: theoretical developments and applications. *Powder Technol.* **2016**, *302*, 108-152.

(281) Kruggel-Emden, H.; Rickelt, S.; Wirtz, S.; Scherer, V. A study on the validity of the multi-sphere Discrete Element Method. *Powder Technol.* **2008**, *188* (2), 153-165.
(282) Guo, Y.; Li, Y.; Liu, Q.; Li, Z.; Jin, H.; Wassgren, C.; Curtis, J. S. Discrete Element Method Model of Elastic Fiber Uniaxial Compression. *arXiv preprint arXiv:1909.02927* **2019**.
(283) Guo, Y.; Wassgren, C.; Curtis, J. S.; Xu, D. A bonded sphero-cylinder model for the discrete element simulation of elasto-plastic fibers. *Chem. Eng. Sci.* **2018**, *175*, 118-129.
(284) Alonso-Marroquin, F. Spheropolygons: A new method to simulate conservative and dissipative interactions between 2D complex-shaped rigid bodies. *Europhys. Lett.* **2008**, *83* (1), 14001.
(285) Pournin, L.; Liebling, T. M. A generalization of distinct element method to tridimensional particles with complex shapes. In Powders and Grains 2005, Stuttgart; 2005.
(286) Govender, N.; Wilke, D. N.; Kok, S.; Els, R. Development of a convex polyhedral discrete element simulation framework for NVIDIA Kepler based GPUs. *J. Comput. Appl. Math.* **2014**, *270*, 386-400.
(287) Nassauer, B.; Liedke, T.; Kuna, M. Polyhedral particles for the discrete element method. *Granul. Matter* **2013**, *15* (1), 85-93.
(288) Markauskas, D.; Kačianauskas, R. Investigation of rice grain flow by multi-sphere particle model with rolling resistance. *Granul. Matter* **2011**, *13* (2), 143-148.
(289) Romuli, S.; Karaj, S.; Müller, J. Discrete element method simulation of the hulling process of Jatropha curcas L. fruits. *Biosys. Eng.* **2017**, *155*, 55-67.
(290) Barr, A. H. Superquadrics and angle-preserving transformations. *IEEE Comput. Graph. Appl.* **1981**, *1* (1), 11-23.
(291) Williams, J. R.; Pentland, A. P. Superquadrics and modal dynamics for discrete elements in interactive design. *Eng. Comput.* **1992**, *9*, 115-127. DOI: https://doi.org/10.1108/eb023852.
(292) Cleary, P. W. DEM simulation of industrial particle flows: case studies of dragline excavators, mixing in tumblers and centrifugal mills. *Powder Technol.* **2000**, *109* (1-3), 83-104.
(293) Cleary, P. W. Large scale industrial DEM modelling. *Eng. Comput.* **2004**, *21* (2/3/4), 169-204.
(294) Lu, G.; Third, J. R.; Müller, C. R. Critical assessment of two approaches for evaluating contacts between super-quadric shaped particles in DEM simulations. *Chem. Eng. Sci.* **2012**, *78*, 226-235.

(295) Podlozhnyuk, A.; Pirker, S.; Kloss, C. Efficient implementation of superquadric particles in Discrete Element Method within an open-source framework. *Comput. Part. Mech.* **2017**, *4* (1), 101-118.
(296) Ji, S.; Wang, S.; Zhou, Z. Influence of particle shape on mixing rate in rotating drums based on super-quadric DEM simulations. *Adv. Powder Technol.* **2020**, *31* (8), 3540-3550.
(297) Thornton, C. Coefficient of restitution for collinear collisions of elastic-perfectly plastic spheres. *J Appl Mech* **1997**, *64* (2), 383-386.
(298) Hertz, H. Über die Berührung fester elastischer Körper und öber die Härte. *J. fur Reine Angew. Math.* **1882**, *92*, 156-171.
(299) Mindlin, R. D. Elastic spheres in contact under varying oblique forces. *J Appl Mech* **1953**, *20*, 327-344.
(300) Walton, O. R.; Braun, R. L. Viscosity, granular-temperature, and stress calculations for shearing assemblies of inelastic, frictional disks. *J. Rheol.* **1986**, *30* (5), 949-980.
(301) Langston, P.; Tüzün, U.; Heyes, D. Continuous potential discrete particle simulations of stress and velocity fields in hoppers: transition from fluid to granular flow. *Chem. Eng. Sci.* **1994**, *49* (8), 1259-1275.
(302) Zhu, H.; Yu, A. Averaging method of granular materials. *Phys. Rev. E: Stat. Phys., Plasmas, Fluids,* **2002**, *66* (2), 021302.
(303) Soltanbeigi, B.; Podlozhnyuk, A.; Papanicolopulos, S.-A.; Kloss, C.; Pirker, S.; Ooi, J. Y. DEM study of mechanical characteristics of multi-spherical and superquadric particles at micro and macro scales. *Powder Technol.* **2018**, *329*, 288-303.
(304) Roessler, T.; Katterfeld, A. Scalability of angle of repose tests for the calibration of DEM parameters. In *12th International Conference on Bulk Materials Storage, Handling and Transportation (ICBMH 2016)*, 2016; Engineers Australia: p 201.
(305) Roessler, T.; Katterfeld, A. Scaling of the angle of repose test and its influence on the calibration of DEM parameters using upscaled particles. *Powder Technol.* **2018**, *330*, 58-66.
(306) Roessler, T.; Katterfeld, A. DEM parameter calibration of cohesive bulk materials using a simple angle of repose test. *Particuology* **2019**, *45*, 105-115.
(307) Chen, J.; Gao, R.; Liu, Y. Numerical study of particle morphology effect on the angle of repose for coarse assemblies using DEM. *Adv. Mater. Sci. Eng.* **2019**, *2019*. DOI: https://doi.org/10.1155/2019/8095267.
(308) Nakashima, H.; Shioji, Y.; Kobayashi, T.; Aoki, S.; Shimizu, H.; Miyasaka, J.; Ohdoi, K. Determining the angle of repose of sand under low-gravity

conditions using discrete element method. *J. Terramech.* **2011**, *48* (1), 17-26.
(309) Alenzi, A.; Marinack, M.; Higgs, C. F.; McCarthy, J. J. DEM validation using an annular shear cell. *Powder Technol.* **2013**, *248*, 131-142.
(310) Angus, A.; Yahia, L. A. A.; Maione, R.; Khala, M.; Hare, C.; Ozel, A.; Ocone, R. Calibrating friction coefficients in discrete element method simulations with shear-cell experiments. *Powder Technol.* **2020**, *372*, 290-304.
(311) Kozicki, J.; Tejchman, J. Numerical simulations of triaxial test with sand using DEM. *Arch. Hydroengineering Environ. Mech.* **2009**, *56* (3-4), 149-172.
(312) Salot, C.; Gotteland, P.; Villard, P. Influence of relative density on granular materials behavior: DEM simulations of triaxial tests. *Granul. Matter* **2009**, *11* (4), 221-236.
(313) Abbaspour-Fard, M. H. Theoretical validation of a multi-sphere, discrete element model suitable for biomaterials handling simulation. *Biosys. Eng.* **2004**, *88* (2), 153-161.
(314) Wiacek, J.; Molenda, M. Moisture-dependent physical properties of rapeseed–experimental and DEM modeling. *Int. Agrophysics* **2011**, *25* (1).
(315) Balevičius, R.; Sielamowicz, I.; Mroz, Z.; Kačianauskas, R. Investigation of wall stress and outflow rate in a flat-bottomed bin: A comparison of the DEM model results with the experimental measurements. *Powder Technol.* **2011**, *214* (3), 322-336.
(316) Coetzee, C. J.; Els, D. N. J. Calibration of discrete element parameters and the modelling of silo discharge and bucket filling. *Comput. Electron. Agric.* **2009**, *65* (2), 198-212.
(317) Lourel, I.; Wu, W.; Morrison, D. J. Experimental validation on the computational modelling of granular flow using the discrete element method (DEM). In *Asia-Pacific Bulk Materials Handling Conference BULKEX*, Melbourne, Australia, 2006.
(318) Weigler, F.; Mellmann, J. Investigation of grain mass flow in a mixed flow dryer. *Particuology* **2014**, *12*, 33-39.
(319) Wilkinson, S. K.; Turnbull, S. A.; Yan, Z.; Stitt, E. H.; Marigo, M. A parametric evaluation of powder flowability using a Freeman rheometer through statistical and sensitivity analysis: A discrete element method (DEM) study. *Comput. Chem. Eng.* **2017**, *97*, 161-174.
(320) Žídek, M.; Rozbroj, J.; Jezerska, L.; Diviš, J.; Nečas, J.; Zegzulka, J.; Demmler, M. Effective use of DEM to design chain conveyor geometry. *Chem. Eng. Res. Des.* **2021**, *167*, 25-36.

(321) Peng, D.; Hanley, K. J. Contact detection between convex polyhedra and superquadrics in discrete element codes. *Powder Technol.* **2019**, *356*, 11-20.
(322) Otsubo, M.; O'Sullivan, C.; Shire, T. Empirical assessment of the critical time increment in explicit particulate discrete element method simulations. *Comput Geotech* **2017**, *86*, 67-79.
(323) Jiang, M.; Kamura, A.; Kazama, M. Numerical study on liquefaction characteristics of granular materials under Rayleigh-wave strain conditions using 3D DEM. *Soils Found.* **2022**, *62* (4), 101176.
(324) Guo, Y.; Wassgren, C.; Hancock, B.; Ketterhagen, W.; Curtis, J. Validation and time step determination of discrete element modeling of flexible fibers. *Powder Technol.* **2013**, *249*, 386-395.
(325) Huang, X.; Hanley, K. J.; O'Sullivan, C.; Kwok, C. Y.; Wadee, M. A. DEM analysis of the influence of the intermediate stress ratio on the critical-state behaviour of granular materials. *Granul. Matter* **2014**, *16* (5), 641-655.

CHAPTER 3.

EXPERIMENTAL INVESTIGATION OF THE EFFECT OF LIGNOCELLULOSIC BIOMASS STRUCTURAL CONSTITUENTS ON THE FLOW BEHAVIOR

Disclaimer: The author previously included partial results of this chapter's work in the following articles:

1. Ehite, E. H.; Drumm, E.; Abdoulmoumine, N. The effect of hemicellulose on the interparticle frictional behavior of lignocellulosic biomass particulates. *Particuology* **2021**, *55*, 16-22. DOI: https://doi.org/10.1016/j.partic.2020.09.002. [1]

2. Ehite, E.H., Oyedeji, O., Abdoulmoumine, N., The role of cellulose, hemicellulose, and lignin on the shear strength and frictional parameters of lignocellulosic biomass particulates. In preparation for submission at *ACS Sustainable Chemistry and Engineering*.

3.1. Introduction

This chapter details the experimental investigation of the relationship between the structural constituents of lignocellulosic biomass particle assemblies and the flow characteristics of the bulk material.

The optimum operation of the biorefining process requires a consistent, efficient flow of the biomass feedstock material through the whole system [2]. As such, researchers have focused on different aspects of the flow process, including characterizing physiochemical properties of lignocellulosic biomass [3], and their variability [4], and the feedstock supply chain process, including the transportation, logistics, and equipment configurations and their impact on biomass flow consistency and efficiency [5, 6]. However, the existing literature lacks a thorough exploration of the impact of the unique structural composition of lignocellulosic biomass on the global flow behavior.

The lignocellulosic biomass cell wall consists of a compound, non-uniform, three-dimensional matrix structure comprising three polymers: cellulose and hemicellulose, both polysaccharides, and lignin, a phenolic polymer, with trace amounts of other organic and inorganic constituents [4, 7-10]. The principal biomass constituents influence different mechanical properties. For example, cellulose, hemicellulose, and lignin contribute to mechanical and chemical stability [11, 12], structural rigidity and shear strength [13], and cohesion and adhesion forces [14, 15], respectively. However, due to their interwoven nature, the individual contribution of each biopolymer to specific mechanical properties is more challenging to quantify [16].

Furthermore, the relative composition of biomass constitutive polymers varies between species, harvest locations, and conditions [17-19]. The typical composition of structural constituents in herbaceous plants is 30–38% cellulose, 16–26% hemicellulose, 16–25% lignin, and 4–9% extractives [20-24]. This is significantly different from softwood and hardwood materials, as softwood species typically include 33–42% cellulose, 22–40% hemicellulose, 27–32%

lignin, and 2–3.5% extractives [25-27], whereas hardwood species include 38–51% cellulose, 17–38% hemicellulose, 21–31% lignin, and 3% extractives [25, 28-30]. The variability results in unique and complex structures in lignocellulosic biomass feedstocks that influence their mechanical behavior. For example, prior studies on herbaceous, softwood, and hardwood feedstock flow characteristics in screw conveyors indicate that hardwood materials exhibit quicker clogging than softwood and herbaceous feedstock [31]. Therefore, the interwoven nature and inherent variability are challenges for investigating the effect of structural constituents on overall flow behavior.

The other challenge is defining biomass flow behavior, a complex characteristic influenced by numerous lignocellulosic biomass physio-mechanical properties. Among them, we are specifically interested in two properties: i) shear strength, which is the strength of a material or component against the type of yield or structural failure when the material or component fails in shear [32, 33], and ii) friction, which represents forces acting perpendicularly and in parallel, respectively, to an interface between two bodies under relative motion or impending relative motion [34-37]. The reason behind this specific interest is that lignocellulosic biomass particles fall in the category of granular materials, i.e., they are a collection of macroscopic particles that undergo unique microscopic interactions [38]. Granular flow scientists characterize the flow behavior of granular particulate assemblies in terms of their shear strength, which depends on the stress states. For granular materials, the shear strength (τ) is defined in terms of the normal stress (σ) and the dimensionless coefficient of friction (μ), as presented in previous chapter (Equation 2.1).

For non-fibrous and stiff materials in unconsolidated, i.e., loose states such as sand and soil samples, the cohesion force is zero, and therefore their shear strength and resulting flow behavior depend only on the normal stress and the internal friction [37, 39, 40]. For granular biomass materials, the cohesion force is non-zero and given by the intercept of the stress-strain curve [41, 42]. Previous studies have shown that translational and rotational motions of the particles in a solid particulate system are governed by the particle-particle and particle-wall coefficients of friction [43-45]. Therefore, shear strength and frictional parameters are critical characteristics necessary to describe the global flow behavior of lignocellulosic biomass materials comprehensively.

Due to their importance in granular material flow, there are a variety of experimental characterization techniques for shear strength and frictional parameters of solid particle assemblies available for a variety of situations. For shear strength, these techniques include direct shear methods using instruments with translational and rotational shear kinematics 48-50 and indirect methods such as compression and penetration tests [46, 47]. During flow, individual particles slide across each other in a shearing action. The shear strength expresses the resistance of a granular material to flow, and thus materials with higher shear strength will have a lower flowability [48, 49]. Similarly, experimental techniques for determining frictional parameters of granular materials under different stress states include the angle of repose measurement by a variety of methods, including the hollow or tilting cylinder method [50, 51], and the fixed funnel method [52]. Al-Hashemi et al. conducted an exhaustive review of the different methods for the angle of repose measurement [53]. They concluded that selecting a measurement method depends on the specific objectives, materials, and application. For example, the fixed funnel/hopper method is used for cohesionless, well-graded materials with a grain size ≤10 mm material [54]. It performs best for materials with a higher flowability, such as pharmaceutical tablets [55]. For poor-flowing material, the fixed funnel method is susceptible to bridging and almost zero flow, making investigating the material flow dynamics difficult [56]. Furthermore, using this method, the angle of repose of two piles of granular material can be compared only if the piles have even, regular slopes, which are not exhibited for cohesive material or extremely angular particles as is the case of lignocellulosic biomass materials [57].

Despite the presence of standardized characterization methods and empirical relationship, the state-of-the-art neither provides much information about quantitative values of shear strength or frictional parameters of different lignocellulosic biomass materials nor does it explore the relationship between these parameters and individual structural constituents of lignocellulosic biomass materials. This realization has motivated, in part, our overarching goal of relating the structural composition of biomass materials with significantly different structural constituents to their flow behavior.

We hypothesize that the lignocellulosic biomass materials of different structural compositions will have significantly different shear strengths and associated frictional characteristics. Our research question is: How can we relate the variation of structural constituent contents between and within lignocellulosic biomass materials with variations in their flow behavior?

We will test this hypothesis by conducting three case studies to quantify the effects of different lignocellulosic biomass structural constituents on the frictional parameters and shear strength of herbaceous, softwood, and hardwood feedstocks through a series of standardized tests.

In Case Study #1, we examined the relationship between lignocellulosic biomass materials from different sources, namely switchgrass, hybrid poplar, and loblolly pine, and containing <u>different proportions of structural constituents, namely cellulose, hemicellulose, and lignin,</u> and their frictional parameters and shear strength.

In Case Study #2, we examined the relationship between the structural compositions of biomass materials of varying cellulosic content but sourced from a single source, namely hybrid poplar, and their frictional parameters and shear strength.

Finally, in case study #3, we examined the relationship between lignocellulosic biomass materials, namely switchgrass, hybrid poplar, and loblolly pine, of different particle sizes and their frictional parameters and shear strength.

3.2. Materials and Methods

3.2.1. Material Selection and Preparation

We used three biomass materials for this case study, representing different bioenergy-relevant feedstocks commonly used in lignocellulosic biorefineries. They are: a) Herbaceous material: Switchgrass (*Panicum virgatum*), b) Softwood: Loblolly pine (*Pinus taeda*), and c) Hardwood: Hybrid poplar (Populus deltoides).

We received the switchgrass (Alamo variant) in dried condition from Genera Energy Inc. in Vonore, TN. Then, we obtained hybrid poplar and loblolly pine materials from trees harvested from the Cumberland Forest Unit of the University of Tennessee, Institute of Agriculture's Forest Resources Research and Education Center in Oliver Springs, TN. The trees were approximately 20-25 and 10 years old for hybrid poplar and loblolly pine, respectively, and were felled, delimbed, and cut into logs at the harvest site. The logs were then debarked using a draw knife and subsequently dried in a large kiln at 48 °C for 10 days to begin removing a portion of the water contained within their fibers. At the end of the drying period, we chipped the logs in a chipper (Model: Predator Chipper Shredder, 6.5 HP, 3 gallons) and then placed them back in a large kiln to continue drying at 48 °C for another 10 days. Subsequently, the switchgrass and the dried chips were hammermilled and further sieved between sieve mesh sizes 10-20 (2 – 0.8 mm), 20-30 (0.8-0.6 mm), and 30–40 (0.6 – 0.4 mm) to generate the final sample materials.

Figure 3.1 shows the herbaceous, softwood, and hardwood materials used for our research.

3.2.2. Chemical and Physical Characterization

We conducted a number of standard chemical and physio-mechanical characterization processes on the sample materials, including proximate analysis, chemical composition analysis, thermogravimetric, density, and compressibility assessments on different feedstock materials following ASTM or NREL standards. The next section discusses these analyses in detail.

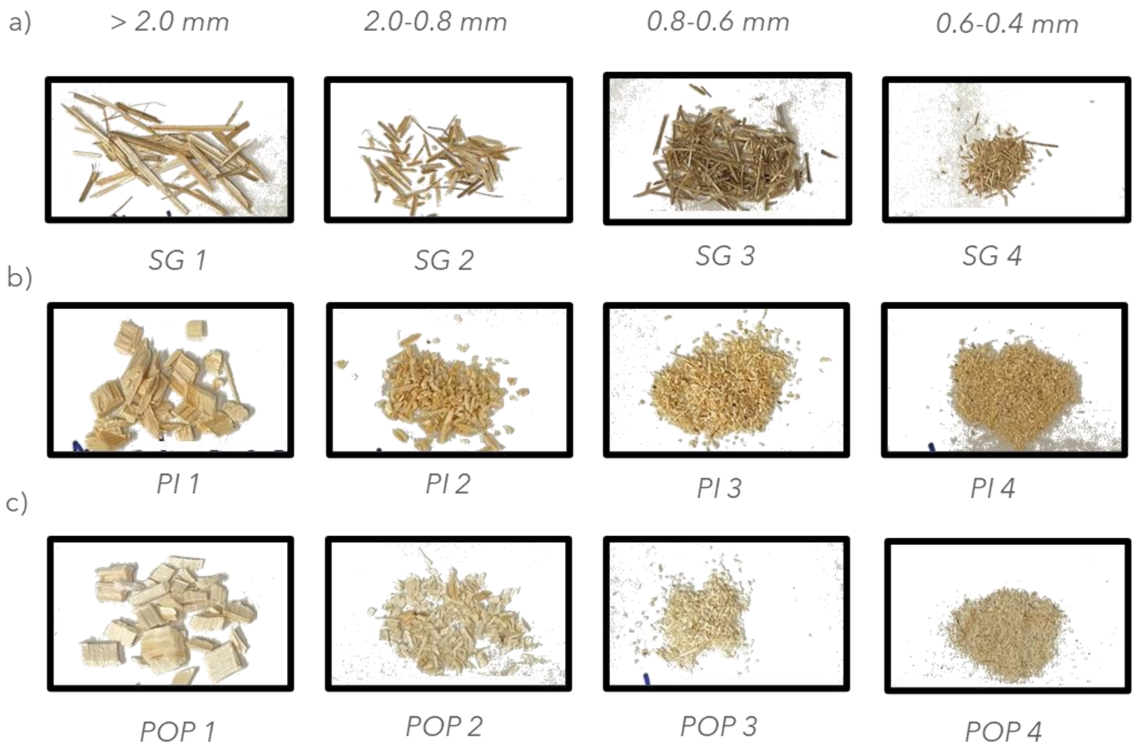

Figure 3.1. Sample materials of different sizes, a) switchgrass, b) loblolly pine, and c) hybrid poplar.

We measured sample materials' moisture, ash, and volatile matter contents according to the standard methods ASTM E871-82 (2013) [58], ASTM E1755-01 (2015) [59], and ASTM E872-82 (2013) [60], respectively. We calculated the fixed carbon by the difference between the volatile matter and ash values. We conducted all proximate analyses in triplicate.

Next, we conducted a chemical composition analysis to determine the cellulose, hemicellulose, and lignin content in our sample materials. Initially, we conducted a Soxhlet extraction process to extract solid extractives from samples specified by the NREL/TP-510-42619 standard [61]. This step is necessary because solid non-structural components (principally phenolic compounds) affect the samples' wet chemistry analysis [62]. Then, we conducted the biomass structural carbohydrates (cellulose and hemicellulose) and lignin content analysis on a wt.% basis (on a dry ash-free basis) following the NREL/TP-510-42618 standard [63]. We conducted the chemical composition analysis in triplicate.

Then, we conducted a thermogravimetric analysis (TGA) on the samples to assess the differences qualitatively and quantitatively in cellulose, hemicellulose, and lignin compositions between the different materials by examining their thermal degradation profile. Thermal decomposition of biomass under increasing temperature initially causes moisture loss, followed by the decomposition of hemicellulose, then cellulose decomposes, and finally, lignin decomposition occurs. We conducted our thermogravimetric analyses using a Pyris 1 thermogravimetric analyzer (Perkin-Elmer, USA) according to the method of ASTM E1131-08 (2014) [64]. We evaluated the decomposition profile of our samples from 25 to 750 °C with a heating rate of 5°C/min under 20 ml/min of helium gas flow using about 5 mg for each run. We generated derivatives of the resulting mass loss thermographs were generated for each run and plotted them against the temperature change. We identified the characteristic peak of cellulose, hemicellulose, and lignin and determined its height relative to the baseline. We conducted all thermogravimetric analyses in triplicate.

Afterward, we measured the particle density of the sample materials using a gas pycnometer (Model AccuPyc 1330, Micromeritics Instrument Corp., Norcross, GA) using the ASTM D5550 standard [65]. We used particles sieved through an ASTM size 40 sieve (0.425 mm) for the particle density analysis. We performed the particle density measurements in triplicate and averaged the values to calculate the average particle density.

Finally, we conducted a compressibility test to examine the sensitivity of our granular lignocellulosic biomass materials to a reduction in volume, i.e., their compressibility due to pressure. We performed the compressibility test with a powder rheometer (model: FT4 Powder Rheometer, Freeman Technology, Tewkesbury, Gloucestershire, UK) using the ASTM D7891-15 standard [66], which provides us the bulk density of the sample material under test as a function of consolidating stresses. We filled a glass sample cylinder vessel (62 mm diameter and 137 ml volume), leveled the material across the top of the vessel's surface, and placed and secured the vessel on the rheometer for compressibility characterization. The rheometer compresses the material using a vented piston at a rate of 1 mm/s until a consolidating pressure of 0.05, 0.5, 1, 2, 4, 6, 8, 10, 12, and 14 kPa is achieved sequentially. Throughout each experimental cycle, the rheometer's software recorded, displayed and saved the bulk density measurements at each consolidating pressure. We derived and computed the compressibility curve and the compressibility index, CI (Equation 3.1) from this data.

$$\mathrm{CI} = \frac{\text{Bulk density at 14 kPa consolidating pressure}}{\text{Unconsolidated bulk density}} \tag{3.1}$$

If the compressibility curve is flat across a range of normal stresses, the material is incompressible; if the density rises, then the material is compressible [67]. The intercept of the plot represents the bulk density in the unconsolidated state. We compared this unconsolidated bulk density with the bulk density determined with a bulk density measurement apparatus (Seedburo Equipment Company, Chicago, Ill., USA) using the ASTM D1895B standard [68]. We did not measure the compressibility characteristics for our largest particle size fraction (>2.0 mm), as the equipment sample vessel was not large enough to hold a representative sample of the largest particle size fraction. We performed the compressibility and bulk density measurements in triplicate.

3.2.3. Flow Behavior Characterization

3.2.3.1. Frictional Parameters

We chose a classical flow characterization technique, namely the angle of repose test, to examine our sample materials' macroscale flow behavior in terms of their frictional parameters. While there is no single consistent standard technique available for characterizing the angle of repose [50, 53, 69-71], we decided to choose the hollow cylinder method for investigating lignocellulosic biomass feedstock used for our research because the kinetics of the test ensures the formation of pile regardless of the cohesiveness of the material and, therefore, can be used reliably for material with poor flow characteristics irrespective of the particle size [52, 72].

The hollow cylinder method places the sample under test inside a hollow cylinder of known dimensions above a base. The cylinder is then displaced vertically from the base at a specific velocity, and the material flows under gravity to form a semi-conical pile. Our experimental setup of the angle of repose test consisted of a clear acrylic cylinder attached to a pulley-based lifting mechanism and an imaging camera.

Figure 3.2 shows the experimental setup used for the angle of repose measurement.

We began the angle of repose experiment by pouring our samples into the plexiglass cylinder (inner diameter = 0.04 m; height = 0.20 m) with a funnel positioned on the cylinder's top rim. We then raised the cylinder vertically at an approximate velocity of 0.1 m/s such that the particles fell on the flat surface and formed a semi-conical pile. We then photographed the pile using a high-resolution camera (model: Canon Rebel T4i Digital SLR Camera, EF-S 55-250mm f4-5.6 lens) placed on an extendable tripod stand with a remote shutter.

We subsequently processed the images using a custom image analysis and segmentation script in MATLAB (The Mathworks, Natick, MA, USA). In order to partition the original image file and segment the area of the sample pile into distinct regions, we used the active contour method, which detects the boundaries of objects using evolving curves [73].

After the image segmentation, we fitted a triangle to the segmented sample pile and calculated the topmost point of the pile as well as the left and right vertex to determine the height (h) and the diameter (D) of the pile. We two angles α_1 at left and α_2 at right, as shown in Figure 3.3. This is because the peak of H of the triangle might not always be directly above the center of the diameter, AB [1].

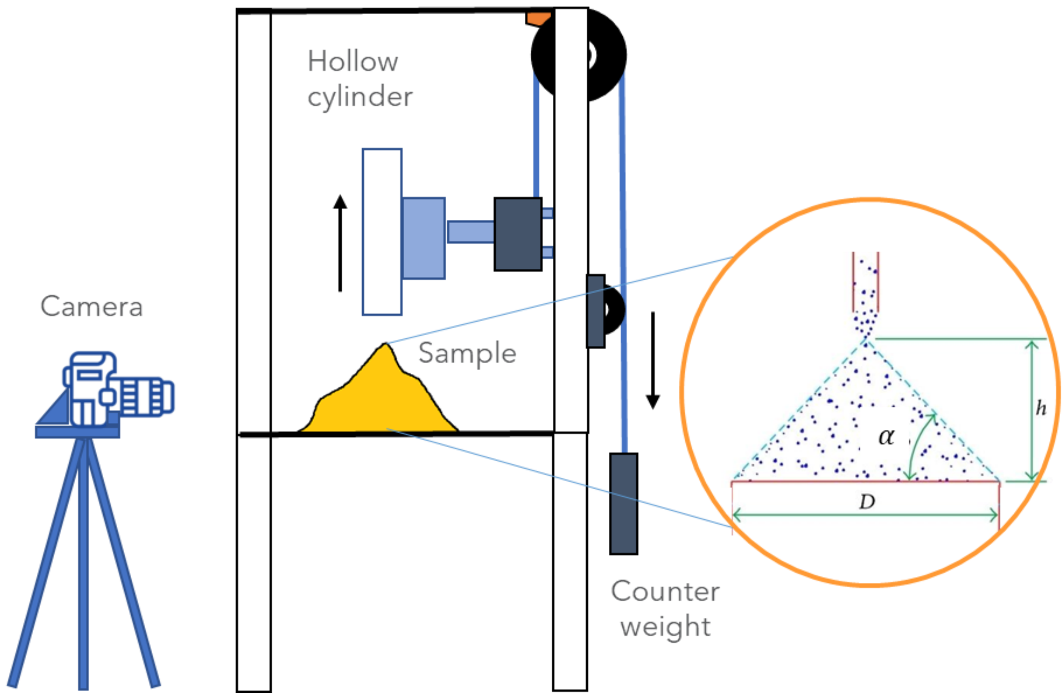

Figure 3.2. Schematic representation of the experimental setup for the angle of repose measurement.

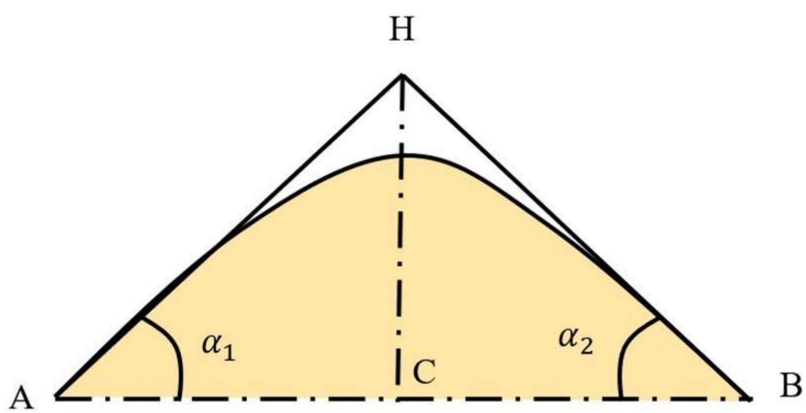

Figure 3.3. Determination of the angle of repose from the material pile using the fitted triangle.

We can calculate the angle of repose using Equation 3.2.

$$\alpha = \frac{1}{2}(\alpha_1 + \alpha_2) = \frac{1}{2}\left(\tan^{-1}\left|\frac{HC}{AC}\right| + \tan^{-1}\left|\frac{HC}{BC}\right|\right) \tag{3.2}$$

where A and B are the left and right vertices of the fitted triangle, and C is the intersection of the perpendicular line from top point H with the baseline AB.

For a loose material, the angle of repose (α) is equal to the angle of friction (φ), which is related to the coefficient of friction, μ, according to Equation 3.3.

$$\mu = tan(\varphi), \tag{3.3}$$

We used approximately 50g of material for each run of the angle of repose test. We replicated the angle of repose testing, imaging, and analysis process 10 times for each sample material and reported the averages.

Finally, we conducted a balanced one-way analysis of variance (ANOVA) on the angle of repose and coefficient of friction for sample materials at $\alpha = 5\%$. Additionally, we conducted a Tukey-HSD multiple comparison test to see if statistically significant differences were observed. We performed the statistical analysis using the "anovan" function in MATLAB.

3.2.3.2. Shear Strength

We conducted a triaxial shear strength test to determine the strength characteristics of the herbaceous, softwood, and hardwood samples. We performed the triaxial test in an S-510 triaxial cell (Durham Geo Slope Indicator, Stone Mountain, GA, USA) under consolidated-drained conditions according to the ASTM D7181-11 standard [74].

Initially, we vertically constrained the material in a cylindrical latex sleeve and applied a vacuum pressure of 35 kPa to create a stiff sample. Then, we placed the sleeve with the sample material between two rigid plates of the triaxial test cell. The top plate can move vertically and apply vertical stress to the sample, which is the major principal stress, σ_1. The movement of this plate controls the axial stress and strain of the sample. Water entered the cell and provided confining pressure along the sides and tops of the sample, resulting in the confining stress or the minor principal stress, σ_3. We investigated sample materials at three levels of confining stresses, namely 138, 207, and 276 kPa. We kept the maximum strain rate at 15% as per the typical triaxial testing convention for loose samples [75, 76]. We conducted a triaxial test for each sample in triplicate.

During the test, the top plate mechanically drives up or down along the axis of the cylinder to apply additional stress in the vertical direction, resulting in the principal stress difference or the deviatoric stress, $\sigma_1 - \sigma_3$. We plot the principal stress difference against axial strain, ε_a [77, 78]. Then, we determined the volume change of the sample by measuring the exact volume of water displaced from the chamber using a flowmeter. We divided this volume change by the initial volume of the cylindrical sample to determine the volumetric strain, ε_v and plotted it against the axial strain, ε_a [79, 80]. Finally, we produced a Mohr's Circle for each consolidated-drained triaxial compression test to determine the maximum and minimum shear stresses that form the shear envelope, i.e., the Mohr-Coulomb failure envelope [81]. Figure 3.4 shows a schematic diagram of the triaxial cell with the sample under uniaxial compressive load.

3.3. Results

3.3.1. Proximate and Density Analysis

Table 3.1 shows the proximate and density analysis results for three biomass sample materials (switchgrass, loblolly pine, and hybrid poplar). The proximate analysis shows that the highest mean moisture content is for hybrid poplar, followed by switchgrass and loblolly pine. Switchgrass has the highest ash content and volatile matter and the lowest fixed carbon. Loblolly pine has the lowest ash content, the lowest volatile content, and the highest fixed carbon. Hybrid poplar has middle values of all three materials for all three characteristics. The proximate analysis results of switchgrass, loblolly pine, and hybrid poplar are consistent with the results reported in literature [82-87].

The density analysis shows that loblolly pine and hybrid poplar samples have higher particle density than switchgrass samples, which is consistent with

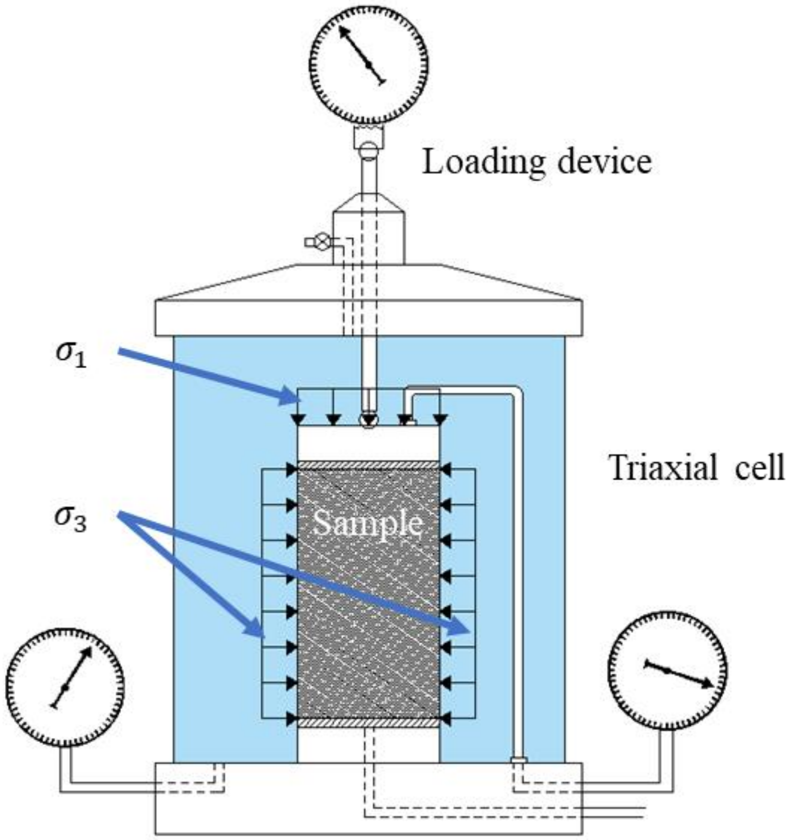

Figure 3.4. Schematic representation of the triaxial cell with the sample under compressive load.

Table 3.1. Proximate and density analysis of switchgrass, loblolly pine, and hybrid poplar samples.

	Mean (SD)		
	Switchgrass	Loblolly pine	Hybrid poplar
Moisture (wt.% wet basis)	7.16 (0.22)	7.35 (0.13)	7.40 (0.62)
Proximate analysis (wt.% dry basis)			
Ash	0.90 (0.08)	0.16 (0.04)	0.61 (0.05)
Volatiles	90.70 (0.69)	85.57 (0.36)	87.12 (0.52)
Fixed Carbon	8.40 (0.69)	14.28 (0.39)	12.27 (0.51)
Density analysis			
Particle density (kg/m^3)	1098.13 (15.33)	1466.09 (16.80)	1195.50 (15.40)

prior comparisons between herbaceous and woody biomass [88, 89]. The increase in particle density can be attributed to the rise in cellulosic content, as cellulose is the densest of all constituent materials owing to its crystalline structure [90, 91].

From the literature, we see that switchgrass particles in a size range of 0.4 to 1 mm have a bulk density ranging from 210 to 100 kg/m^3 and particle density ranging from 690 to 815 kg/m^3 [92-94]. Olatunde et al. conducted a density analysis with loblolly pine grinds [95] ranging in size from sieve sizes 12 to 50 (nominal sieve opening of 1.7 mm to 0.300 mm) and found the particle density of loblolly pine to range from 1453.1 to 1437.5 kg/m^3, and bulk density range from 254 to 152.7 kg/m^3. For hybrid poplar samples, Morales Vera et al. found a bulk density ranging from 160 to 180 kg/m^3 for particle sizes ranging from 2- to 5 mm [96], whereas for particles in the same size range, Lam et al. found particle density values to range from 1213 to 1164 kg/m^3 [97]. Therefore, we can conclude that prior findings from the literature support our density analysis results.

3.3.2. Structural and Thermogravimetric Analysis

Table 3.2 shows the overall chemical composition of the sample materials. Compared to switchgrass samples, the woody samples have higher cellulose content and lower hemicellulose content, whereas the lignin content is not significantly different.

Table 3.2. Chemical composition (wt.% based on dry ash free basis) of switchgrass, loblolly pine, and hybrid poplar samples.

	Mean (SD)		
	Switchgrass	Loblolly pine	Hybrid poplar
Cellulose (Glucose)	27.2 (0.2)	38.1 (0.5)	44.1 (0.9)
Hemicellulose	30.1 (0.0)	19.6 (0.1)	20.7 (0.1)
Total sugar	57.3 (0.1)	57.7 (0.3)	64.8 (0.4)
Xylose	25.5 (0.1)	14.8 (0.2)	15.5 (0.4)
Galactose	2.4 (0.1)	3.0 (0.1)	3.1 (0.1)
Arabinose	2.2 (0.0)	0.4 (0.0)	0.6 (0.1)
Mannose	0.0 (0.0)	1.5 (0.0)	1.6 (0.1)
Total Lignin	21.2 (0.1)	21.7 (0.2)	23.3 (0.3)
Acid soluble lignin	2.1 (0.0)	2.1 (0.0)	5.2 (0.1)
Acid insoluble lignin	19.1 (0.1)	19.6 (0.1)	18.0 (0.3)
Acetyl	3.3 (0.7)	5.7 (0.1)	5.1 (0.4)

Figure 3.5 shows the DTG plots versus temperature for the switchgrass, loblolly pine, and hybrid poplar samples at a heating rate of 5° C/min.

We observed that the hemicellulose peak for the raw samples occurs at around 300 °C with a prominent shoulder, while the cellulose peak occurs at about 375 °C. Hybrid poplar has a higher peak than loblolly pine and switchgrass. Sundar et al. reported a similar DTG curve for the switchgrass samples of similar size (40 mesh), with hemicellulose peak and cellulose peaks around 300 °C and 337 °C, respectively [98].

Moreover, switchgrass shows a prominent shoulder in the hemicellulose decomposition, indicating a higher proportion of hemicellulose content. The smoothening of the hemicellulose peak for the woody biomass samples can be attributed to the absence of lower molecular weight polymers. Therefore, hemicellulose is included in the cellulose peak instead of appearing as a distinct peak [98]. Furthermore, an increase in the magnitude of the mass loss rates from switchgrass to woody samples is observed. Previous studies demonstrated that higher volatile contents correspond to higher mass loss rates during thermal decomposition [99]. Therefore, the differences in the magnitude of the mass loss rate correlate well with the volatile contents presented in Table 3.1.

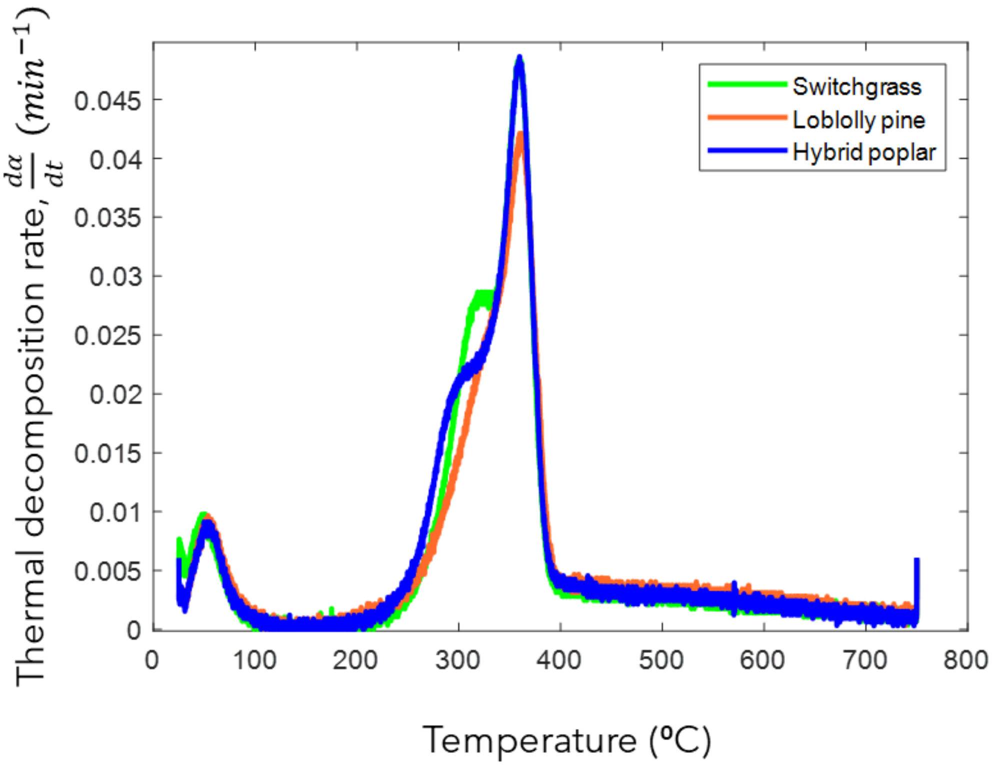

Figure 3.5. Differential thermogravimetric (DTG) curves of the thermal decomposition of switchgrass, loblolly pine, and hybrid poplar samples.

Overall, our observations confirmed the results obtained from structural analysis concerning the cellulose and hemicellulose content of herbaceous, softwood, and hardwood samples.

3.3.3. Frictional Parameters

Figure 3.6 shows the material piles formed for the angle of repose test for the switchgrass, loblolly pine, and hybrid poplar samples after image processing.

Table 3.3 summarizes the average angle of repose and the corresponding coefficient of friction for the different sample batches.

The results show that the angle of repose and coefficient of friction decreased from herbaceous to woody samples. Therefore, we conducted a statistical significance test using One-way ANOVA to examine the differences.

Figure 3.7 shows the box plots for the angle of repose and coefficient of friction values for the switchgrass, loblolly pine, and hybrid poplar samples.

Table 3.4 summarizes the ANOVA results (at α=0.05) for the average angle of repose and the corresponding coefficient of friction. The boxplots for the switchgrass, loblolly pine, and hybrid poplar samples do not overlap, indicating a significant difference between those two sample batches. This is supported by the ANOVA results that show that both the angle of repose and

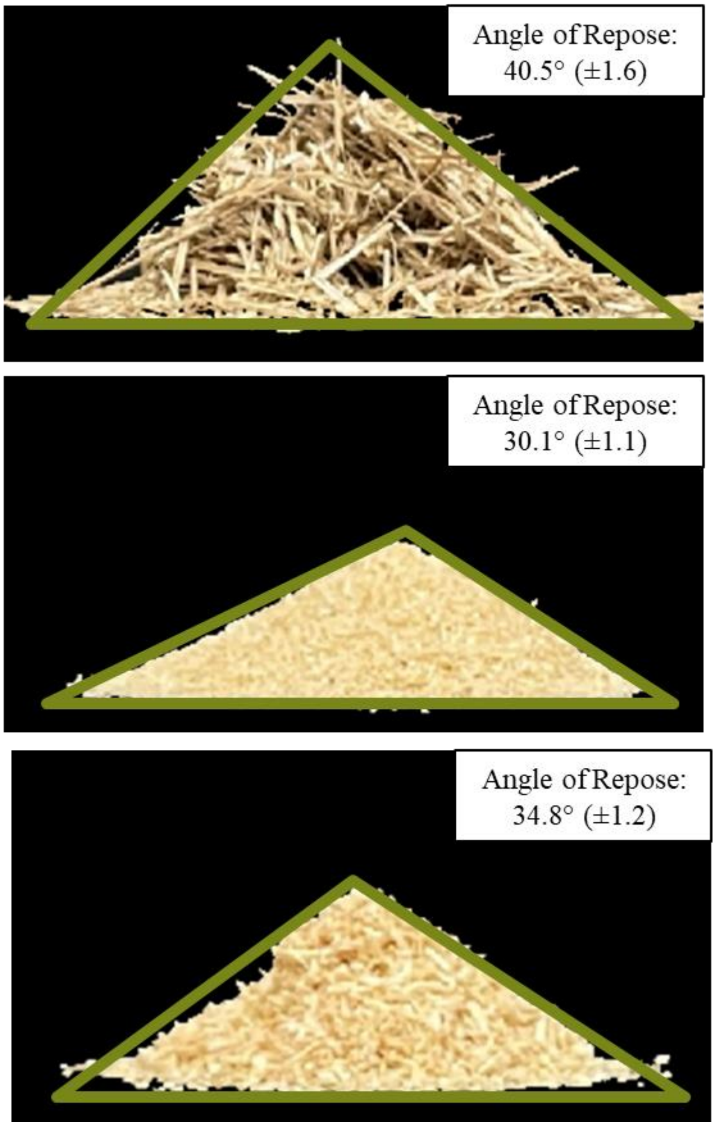

Figure 3.6. Material pile formed for a) switchgrass, b) loblolly pine, and c) hybrid poplar samples, after image processing.

Table 3.3. The angle of repose and the coefficient of friction results for the switchgrass, loblolly pine, and hybrid poplar samples.

	Mean (SD)		
	Switchgrass	Loblolly pine	Hybrid poplar
Angle of repose (AOR)	40.5° (1.6)[a]	30.1° (1.1)[b]	34.8° (1.2)[c]
Coefficient of friction (μ)	0.61 (0.0)	0.46 (0.0)	0.5 (0.0)

SD stands for the standard deviation for N = 10 replicates per treatment.

a, b, and c are significantly different from each other ($p<0.05$)

a)

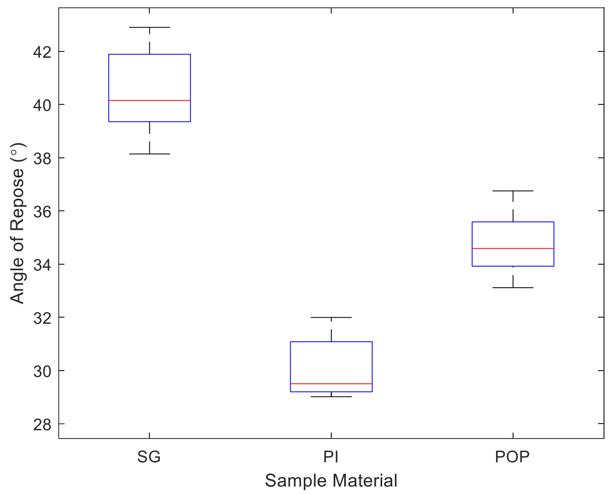

b)

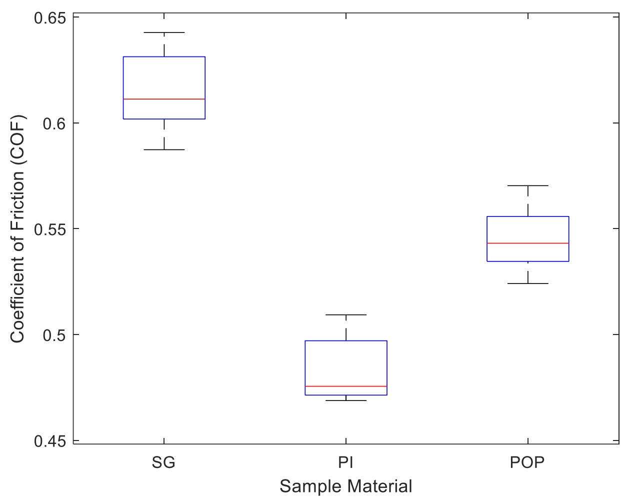

Figure 3.7. Boxplots for the a) angle of repose, b) coefficient of friction results for switchgrass, loblolly pine, and hybrid poplar samples.

Table 3.4. ANOVA tables for a) angle of repose and b) coefficient of friction results for switchgrass, loblolly pine, and hybrid poplar samples.

a)

Source	df	Sum of Squares	Mean Square	F Ratio	Prob > F
Model	2	270.76	135.38	61.07	0.00
Error	12	26.60	2.217		
Total	14	297.36			

b)

Source	df	Sum of Squares	Mean Square	F Ratio	Prob > F
Model	2	0.04	0.02	63.15	0.00
Error	12	0.00	0.0		
Total	14	0.04			

the coefficient of friction values are not the same for all the sample groups ($p<0.05$). Thus, based on our statistical analysis, we can conclude significant differences in frictional behavior between the switchgrass, softwood, and hardwood biomass samples. According to the Carr classification, the switchgrass samples show fair-flowing characteristics (between 38-45°), while the softwood and hardwood have free-flowing characteristics (between 30-38°) [100]. The results are consistent with the findings of Lam et al., as they conducted a fixed-funnel angle of repose test on switchgrass samples varying in size from 707 μm to 25 μm and found the angle of repose to range between 35.56° and 43.03° [101]. Similarly, studies conducted on woody biomass varying in size from 2000 μm to 400 μm have shown to exhibit values of angle of repose ranging between 22° to 37° [102-104].

Overall, based on image processing and statistical analysis values, the samples' flowability characteristics and frictional behavior are significantly different between the herbaceous and the woody biomass samples.

The improvement in flowability due to the variation in structural composition can be attributed to a decrease in frictional forces acting between the particles. The moisture content for the herbaceous and woody samples is between 7.16 and 7.40% in this study, which suggests the capillary force between the particles is within a close range and should not significantly affect the flowability and friction characteristics of particles [105]. Nzokou et al. reported that materials with a lower amount of lignin and extractives content on the woody biomass surface affect their wettability and Van der Waal's force between the particles [106]. Kumar et al. found that epoxy-based hybrid composites (bonded with natural fiber microparticles) undergoing alkali treatment to reduce the hemicellulose and lignin in their structural matrix results in improved flow characteristics [107]. We believe the difference in cellulosic content between lignocellulosic matrices has caused a difference in forces existing on the surfaces between the inter-particles, resulting in different particle flow characteristics.

3.3.4. Compressibility Characteristics

Figure 3.8 shows the bulk density vs. normal stress plots for switchgrass, loblolly pine, and hybrid poplar of different mesh sizes.

We see that all of our materials are compressible, as their bulk density increases with increasing stress. The highest level of bulk density occurs for loblolly pine samples, consistent with our particle density analysis results in Table 3.1, i.e., loblolly pine shows the highest particle density among the sample materials. Additionally, the bulk density at the same stress level for switchgrass samples of all sizes is significantly lower than loblolly pine and hybrid poplar. The low bulk density of herbaceous samples indicates their porosity is lower

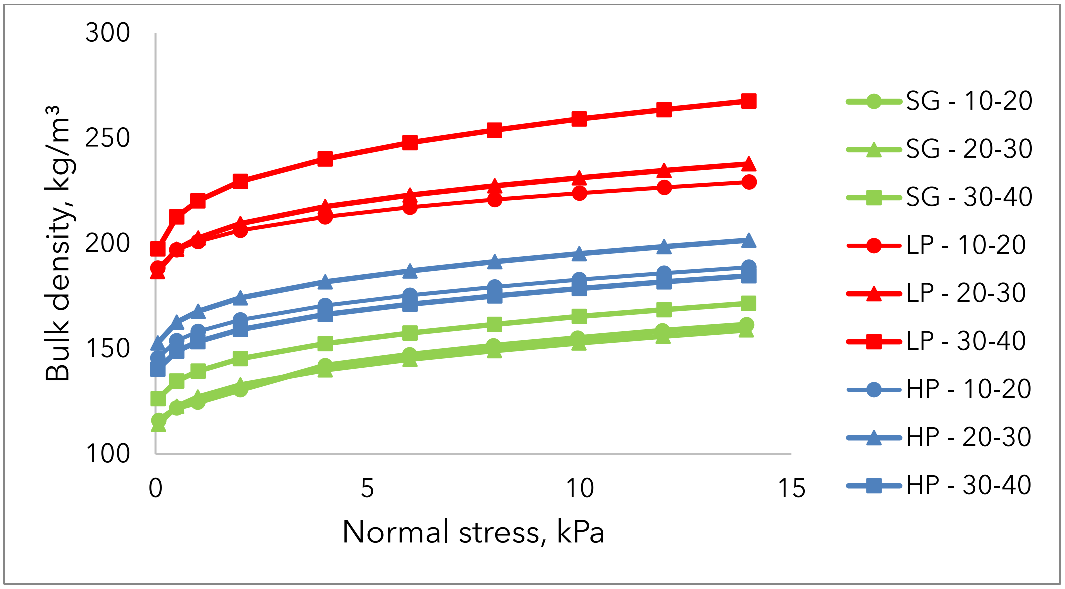

Figure 3.8. Bulk density as a function of normal stress, i.e., compressibility curves for switchgrass, loblolly pine, and hybrid poplar materials of different sizes.

than softwood and hardwood samples, consistent with prior studies comparing herbaceous and woody biomass samples [92, 108].

Finally, the bulk density increases as the particle size decreases. As bulk density is the amount of material by weight in a definite volume, a smaller particle size results in more material accommodated by the same volume. Therefore, we achieve the highest bulk density for mesh size 30-40 (0.6-0.4 mm) samples of loblolly pine, indicating it has the lowest porosity [109, 110].

Table 3.5 shows the unconsolidated bulk density from the compressibility test (the intercept of the bulk density vs. normal stress curve) and the direct measurement using the bulk density measurement apparatus. The results are similar between the two methods, and the measured values for bulk density are consistent with previous reports from the literature for switchgrass, loblolly pine, and hybrid poplar [111].

3.3.5. Shear Strength Characteristics

Figure 3.9 shows the principal stress difference as a function of the axial strain at 138, 207, and 276 kPa minor principal stresses for different sample batches. For all materials, the deviatoric stress increases with the level of confining stress, i.e., the material shows increased strength against the applied load. At the confining stress levels used in our test, the material does not reach

Table 3.5. Comparison of bulk density from compressibility plot and direct measurement.

Material	Particle mesh size	Bulk density from compressibility plot (kg/m^3)	Bulk density from direct measurement (kg/m^3)
Switchgrass	10-20	130.41	133.26 (±1.78)
	20-30	130.91	135.26 (±1.33)
	30-40	143.95	145.83 (±1.09)
Loblolly pine	10-20	204.86	206.20 (±1.34)
	20-30	207.67	202.11 (±1.22)
	30-40	227.15	239.25 (±1.69)
Hybrid poplar	10-20	162.02	165.68 (±1.99)
	20-30	172.26	176.31 (±1.44)
	30-40	159.33	185.06 (±1.85)

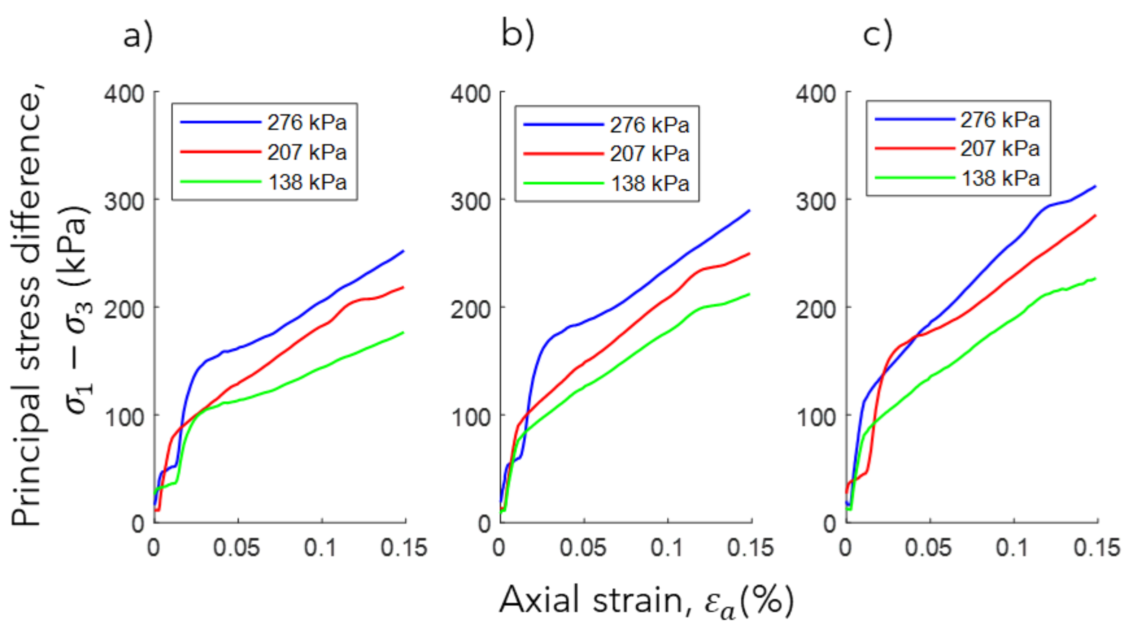

Figure 3.9. Principal stress difference vs. axial strain for a) switchgrass, b) loblolly pine, c) hybrid poplar samples.

failure at the maximum strain rate of 15%. The lower deviatoric stress at lower levels of confining stress results from the lower degree of axial support for the sample material during the testing [112, 113]. Woody samples have higher deviatoric stress at the same confining stress, indicating an increase in the material shear strength [114].

Figure 3.10 shows the volumetric strain as a function of the axial strains for the different sample batches. The volumetric response indicates a tendency to contract, similar to the characteristics of a typical loose granular specimen [115]. The contractive phase is quite long and does not reach the peak volumetric strain level at the 15% strain rate. The level of contraction increases from herbaceous to woody materials.

Figure 3.11 shows Mohr's circles and resulting shear envelopes for the different sample batches. Table 3.6 presents average shear strength values, shear envelope sizes, and the cohesion forces at different confining stresses.

The switchgrass sample has a shear envelope (difference between the maximum and minimum shear stress) encompassing 37.9 kPa. The size of the shear envelope and the cohesion force (the y-intercept) increases for woody samples, from 52.3 kPa for loblolly pine to 55.2 kPa for hybrid poplar. The results indicate that shear strength increased from herbaceous to woody biomass. Statistical analysis using a One-way ANOVA test and subsequent Tukey's HSD

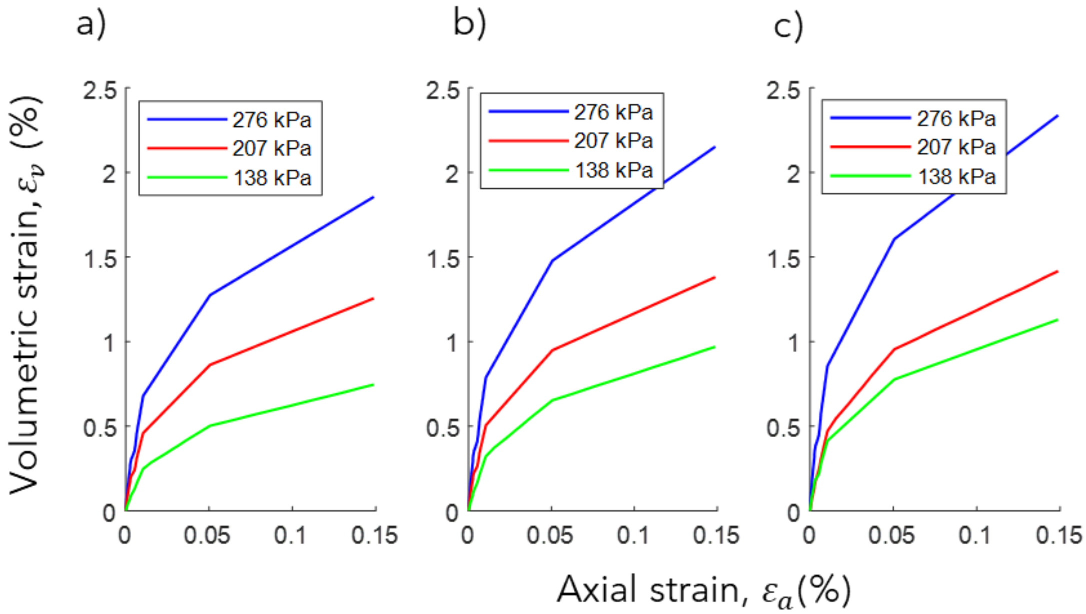

Figure 3.10. Volumetric strain vs. axial strain for a) switchgrass, b) loblolly pine, c) hybrid poplar samples.

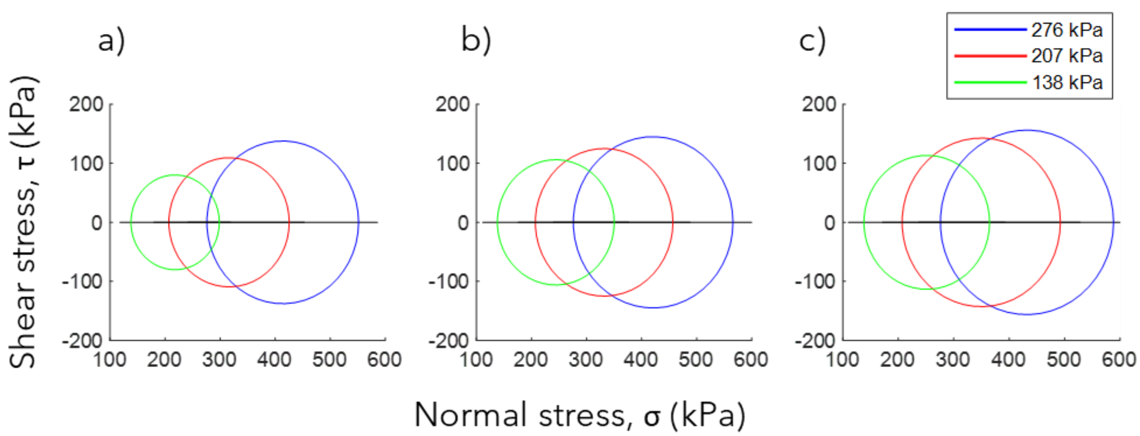

Figure 3.11. Mohr's Circles at different confining stresses, a) switchgrass, b) loblolly pine, and c) hybrid poplar samples.

Table 3.6. Summary of shear strength parameters for switchgrass, loblolly pine, and hybrid poplar samples.

Minor principal stress, σ_3 (kPa)	Average Shear strength, $Ys = (\sigma_3 - \sigma_1)/2$ (kPa)		
	Mean (SD)		
	Switchgrass	Loblolly pine	Hybrid poplar
138	80.3 (10.1) [a]	106.2 (5.3) [b]	113.4 (13.3) [c]
207	109.4 (11.0) [a]	125.0 (12.7) [b]	142.8 (11.7) [c]
276	126.2 (9.1) [a]	145.1 (11.1) [b]	156.2 (16.7) [c]
Shear envelope size ($\tau_{max} - \tau_{min}$) (kPa)	37.9	52.3	55.2
Cohesion (kPa)	27.1	38.9	42.8

SD stands for the standard deviation for N = 3 replicates per sample material.

a and c are significantly different ($p<0.05$)

test indicates a significant difference between the switchgrass and the hybrid poplar samples (one-way ANOVA, Tukey's HSD, $p<0.05$). Overall, based on the triaxial test results, the shear strength characteristics of the samples are significantly different between the herbaceous, softwood, and hardwood samples. This, in turn, indicates that differences in relative composition have resulted in significant differences in the stress states of the biomass material under test.

Helmerius et al. showed that [116] silver birchwood chips with lower hemicellulose content exhibit lower compression strength, tensile strength, and burst strength index, all of which are proportional to shear strength. Since the moisture content between the different sample batches is not significantly different, we can rule out the effect of interparticle capillary forces [117, 118]. Zhang et al., in their research on the molecular dynamics simulations of cellulose-hemicellulose composites under shear loading, showed that the presence of hemicellulose chains of different shapes between cellulose microfibrils increases the overall shear strength of wood specimens increases [119]. Depending on the binding modes, the magnitude of the shear strength changes, where the differences are caused by the contribution of cellulose-hemicellulose hydrogen bonds and the expansion of the covalent bonds in the hemicellulose chain backbone [120, 121]. Therefore, we believe the presence of a higher amount of cellulose and hemicellulose in the lignocellulosic matrix has caused changes in the bond structure of the lignocellulose matrix, resulting in increased strength characteristics for hardwood.

3.3.6. Case Study #2: Relation of Frictional Parameters and Shear Strength Characteristics with Biomass of Varying Cellulose Content

To study the relationship between different structural compositions of lignocellulosic biomass materials, we collected six different hybrid poplar samples from different forest sites in the Southeastern United States in chip form [122]. We initially hammermilled hybrid poplar chips through a 1 mm screen to create starter batches and further sieved them between sieve mesh sizes 20 – 40 (0.6 – 0.4 mm) to create our sample batches (hereafter referred to as SE-POP 1, SE-POP 2…, SE-POP 6).

Table 3.7 shows selected hybrid poplar samples' chemical composition (carbohydrates and lignin). The cellulose content significantly changed between the selected hybrid poplar samples, whereas the hemicellulose and lignin content were not significantly different.

We then conducted the angle of repose and triaxial shear strength study with these batches using the process outlined in the previous sections.

Table 3.7. Chemical composition (wt.% based on dry ash free basis) of hybrid poplar samples with different cellulosic contents.

	Mean (SD)					
	SE-POP 1	SE-POP 2	SE-POP 3	SE-POP 4	SE-POP 5	SE-POP 6
Cellulose	44.1 (0.9)	36.9 (0.3)	38.1 (0.5)	33.4 (0.3)	32.2 (0.5)	27.2 (0.2)
Hemicellulose	20.7 (0.1)	19.5 (0.0)	19.6 (0.1)	18.1 (0.1)	18.0 (0.1)	17.2 (0.0)
Total Lignin	23.3 (0.3)	25.2 (0.2)	26.9 (0.4)	30.0 (0.2)	24.5 (0.3)	25.6 (0.1)

Figure 3.12 shows the angle of repose values from the hollow cylinder test as a function of the structural constituents, namely cellulose, hemicellulose, and lignin, for the poplar samples of the same size but different compositions, ranging from high cellulosic to low cellulosic content.

Based on the R-square values, we conclude that the angle of repose has a strong correlation with cellulose, a slightly weaker correlation with hemicellulose, and no significant relation with lignin.

Figure 3.13 shows shear strength values from the triaxial test as a function of the structural constituents, namely cellulose, hemicellulose, and lignin, for the same poplar samples of the same size. Based on the R square values, we see that shear strength again has a strong correlation with cellulose, a slightly weaker correlation with hemicellulose, and no significant relation with lignin. The positive correlation of shear strength and angle of repose characteristics with the cellulose content can be attributed to the longer length of the linear chain of β-(1-4)-D-glucopyranose bonds in materials with higher cellulose content [120, 123, 124]. Prior studies on pretreatment with woody materials have shown that reducing the hemicellulose and lignin content to increase the cellulose percentage in the matrix has led to the strength and toughness of prepared densified wood to increase by 7-10 times higher, and on a scale comparable with metallic alloys [124-126]. To create better-flowing materials, we

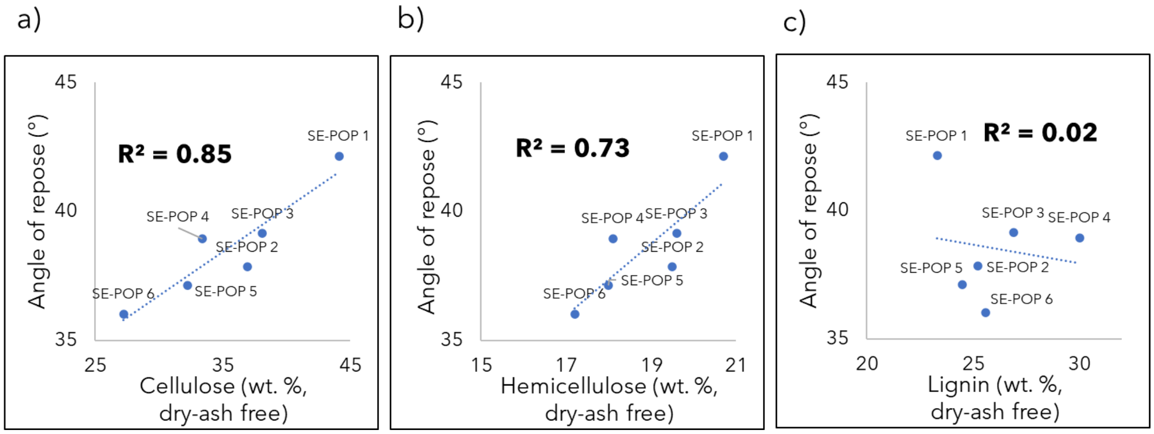

Figure 3.12. Angle of repose as a function of structural constituents, i.e., a) cellulose, b) hemicellulose, and c) lignin for biomass materials of the same size (0.6-0.4 mm).

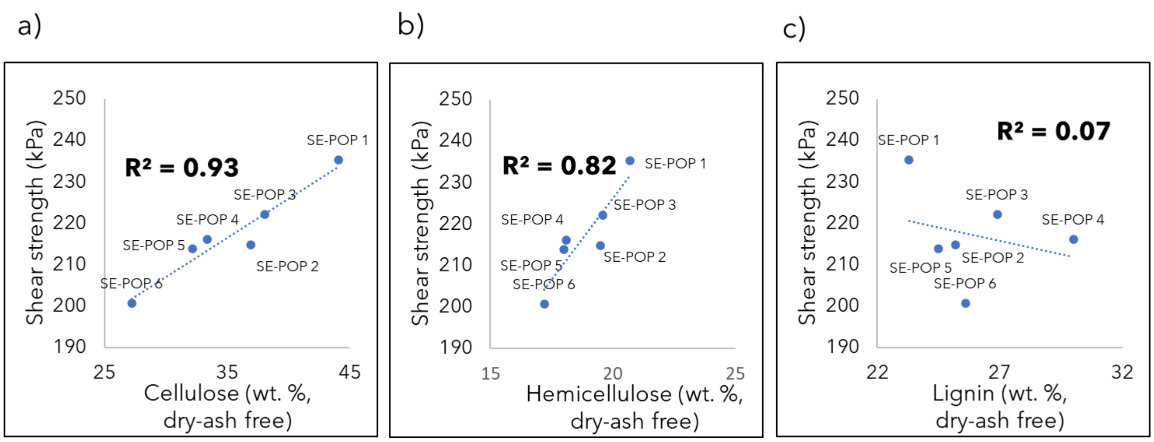

Figure 3.13. Shear strength as a function of structural constituents, i.e., a) cellulose, b) hemicellulose, and c) lignin for biomass materials of the same size (0.6-0.4 mm).

desire an opposite outcome, i.e., a material with lower shear strength resulting in higher flowability. Therefore, using materials with lower cellulosic content can lead to better flow characteristics. Additionally, cellulose is the densest of all the constituents due to their crystallinity [127-129], making the high cellulosic sample (SE-POP 1) the densest. This observation is supported by thermogravimetric analysis, which shows cellulose peaks are highest for materials with higher cellulosic content. Therefore, we can conclude that materials with a lower cellulose content provide the lowest resistance to flow and may give the best flow performance.

3.3.7. Case Study #3: Relation of Frictional Parameters and Shear Strength Characteristics with Particle Sizes

To study the relationship between particle sizes and their frictional and strength parameters, we selected the same materials as used in Case Study #1. The particle sizes range from > 2 mm, 2 – 0.8 mm, 0.8-0.6 mm), and 0.6 – 0.4 mm.

Figure 3.14 shows the angle of repose from the hollow cylinder test as a function of particle size for switchgrass, loblolly pine, and hybrid poplars of different sizes. The results based on the extremely low R-square values indicate that particle size does not significantly correlate with the frictional parameters

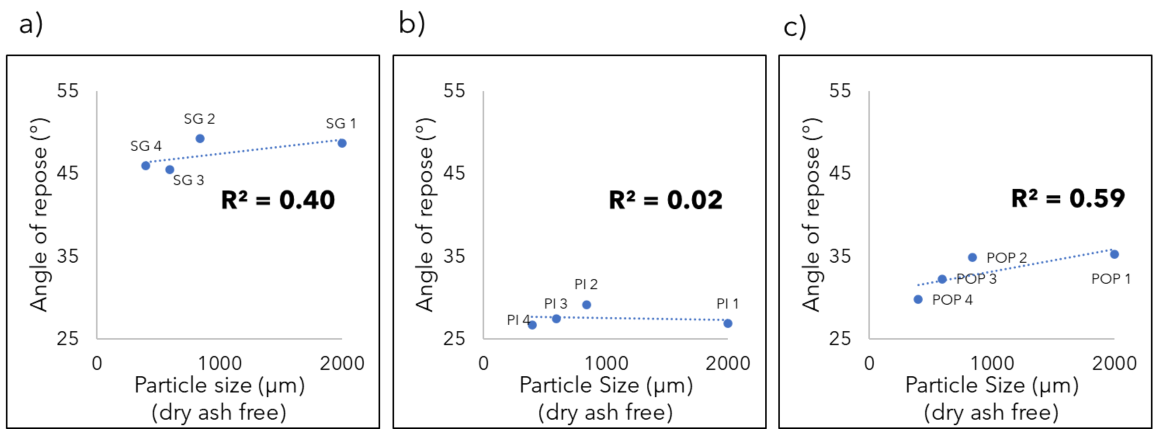

Figure 3.14. Angle of repose as a function of particle size for a) switchgrass, b) loblolly pine, and c) hybrid poplar samples.

for all cases. The magnitude of the angle of repose for hardwood and softwood materials is lower than for herbaceous materials.

Figure 3.15 presents the shear strength from the triaxial test as a function of particle size for our switchgrass, loblolly pine, and hybrid poplars of different sizes. Similar to the angle of repose results, we see that the R-square values are very low, and therefore, the size of sample particles does not correlate significantly with the shear strength for all cases. Interestingly, unlike the angle of repose results, the magnitude of the shear strength of hardwood, namely hybrid poplar, is significantly higher than the softwood and herbaceous material.

3.3.8. Conclusions

In this work, we present the findings of an investigation on the effect of the varying proportion of lignocellulosic biomass structural constituents on the frictional parameters and shear strength characteristics of herbaceous, softwood, and hardwood samples. We observed that lignocellulosic biomass materials with high levels of cellulose and hemicellulose exhibit higher shear strength characteristics and frictional parameters. In contrast, the lignin content and particle size do not strongly affect the shear strength characteristics and

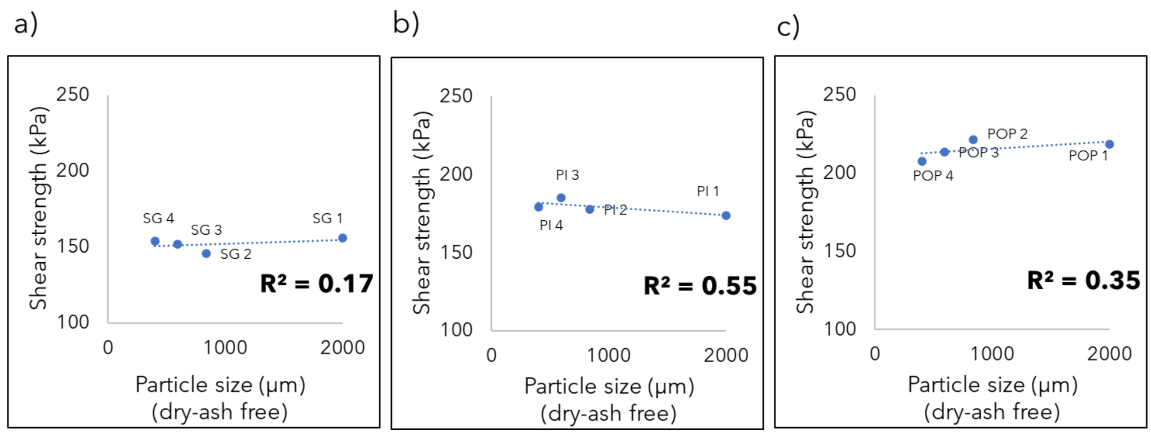

Figure 3.15. Shear strength as a function of particle size for a) switchgrass, b) loblolly pine, and c) hybrid poplar samples.

frictional parameters. On the other hand, the relation between shear strength and angle of repose and the biomass materials of different species requires further investigation. While we expected trends and relations between shear strength, angle of repose, and density with biomass components to be similar between different species, we did not see that in reality. Hardwood materials show higher shear strength but a lower angle of repose against herbaceous switchgrass. Our inference is that this phenomenon has to do with the different stress states the materials are in for different flow tests: compressed, densified in the triaxial test and compressibility test, and loose, free-flowing under gravity for the angle of repose test. Overall, we can conclude that lignocellulosic materials with lower shear strength characteristics and frictional parameters have better flowability and may be used to improve flow operation in biorefineries.

References

(1) Ehite, E. H.; Drumm, E.; Abdoulmoumine, N. The effect of hemicellulose on the interparticle frictional behavior of lignocellulosic biomass particulates. *Particuology* **2021**, *55*, 16-22. DOI: https://doi.org/10.1016/j.partic.2020.09.002.

(2) Taylor, G. Biofuels and the biorefinery concept. *Energy Policy* **2008**, *36* (12), 4406-4409.

(3) Cai, J.; He, Y.; Yu, X.; Banks, S. W.; Yang, Y.; Zhang, X.; Yu, Y.; Liu, R.; Bridgwater, A. V. Review of physicochemical properties and analytical characterization of lignocellulosic biomass. *Renew. Sust. Energ. Rev.* **2017**, *76*, 309-322.

(4) Yan, J.; Oyedeji, O.; Leal, J. H.; Donohoe, B. S.; Semelsberger, T. A.; Li, C.; Hoover, A. N.; Webb, E.; Bose, E.; Zeng, Y. Characterizing variability in lignocellulosic biomass-A review. *ACS Sustain. Chem. Eng.* **2020**, *8* (22), 8059–8085. DOI: https://doi.org/10.1021/acssuschemeng.9b06263.

(5) Miao, Z.; Shastri, Y.; Grift, T. E.; Hansen, A. C.; Ting, K. Lignocellulosic biomass feedstock transportation alternatives, logistics, equipment configurations, and modeling. *Biofuel Bioprod Biorefin* **2012**, *6* (3), 351-362.

(6) Narani, A.; Coffman, P.; Gardner, J.; Li, C.; Ray, A. E.; Hartley, D. S.; Stettler, A.; Konda, N. M.; Simmons, B.; Pray, T. R. Predictive modeling to de-risk bio-based manufacturing by adapting to variability in lignocellulosic biomass supply. *Bioresour. Technol.* **2017**, *243*, 676-685.

(7) Sun, Y.; Cheng, J. Hydrolysis of lignocellulosic materials for ethanol production: a review. *Bioresour. Technol.* **2002**, *83* (1), 1-11.

(8) Xu, F.; Yu, J.; Tesso, T.; Dowell, F.; Wang, D. Qualitative and quantitative analysis of lignocellulosic biomass using infrared techniques: a mini-review. *Appl. Energy* **2013**, *104*, 801-809.

(9) Yan, W.; Acharjee, T. C.; Coronella, C. J.; Vasquez, V. R. Thermal pretreatment of lignocellulosic biomass. *Environ. Prog. Sustain.* **2009**, *28* (3), 435-440.

(10) Oyedeji, O.; Gitman, P.; Qu, J.; Webb, E. Understanding the Impact of Lignocellulosic Biomass Variability on the Size Reduction Process: A Review. *ACS Sustain. Chem. Eng.* **2020**, *8* (6), 2327-2343. DOI: https://doi.org/10.1021/acssuschemeng.9b06698.

(11) Tomme, P.; Warren, R. A. J.; Gilkes, N. R. Cellulose hydrolysis by bacteria and fungi. *Adv. Microb. Physiol.* **1995**, *37*, 1-81.

(12) Dutta, S.; Pal, S. Promises in direct conversion of cellulose and lignocellulosic biomass to chemicals and fuels: Combined solvent–

nanocatalysis approach for biorefinary. *Biomass Bioenergy* **2014**, *62*, 182-197.
(13) Thota, S. P.; Badiya, P. K.; Yerram, S.; Vadlani, P. V.; Pandey, M.; Golakoti, N. R.; Belliraj, S. K.; Dandamudi, R. B.; Ramamurthy, S. S. Macro-micro fungal cultures synergy for innovative cellulase enzymes production and biomass structural analyses. *Renew. Energ.* **2017**, *103*, 766-773.
(14) Jiang, Z.; Hu, C. Selective extraction and conversion of lignin in actual biomass to monophenols: A review. *J. Energy Chem.* **2016**, *25* (6), 947-956.
(15) Pachón-Morales, J.; Perré, P.; Casalinho, J.; Do, H.; Schott, D.; Puel, F.; Colin, J. Potential of DEM for investigation of non-consolidated flow of cohesive and elongated biomass particles. *Adv. Powder Technol.* **2020**, *31* (4), 1500-1515.
(16) Hamawand, I.; Seneweera, S.; Kumarasinghe, P.; Bundschuh, J. Nanoparticle technology for separation of cellulose, hemicellulose and lignin nanoparticles from lignocellulose biomass: A short review. *Nano-Struct. Nano-Objects* **2020**, *24*, 100601.
(17) Zhang, K.; Johnson, L.; Nelson, R.; Yuan, W.; Pei, Z.; Wang, D. Chemical and elemental composition of big bluestem as affected by ecotype and planting location along the precipitation gradient of the Great Plains. *Ind. Crops Prod.* **2012**, *40*, 210-218.
(18) McKendry, P. Energy production from biomass (part 1): overview of biomass. *Bioresour. Technol.* **2002**, *83* (1), 37-46.
(19) Huber, G. W.; Dumesic, J. A. An overview of aqueous-phase catalytic processes for production of hydrogen and alkanes in a biorefinery. *Catal. Today* **2006**, *111* (1-2), 119-132.
(20) Bilba, K.; Savastano Junior, H.; Ghavami, K. Treatments of non-wood plant fibres used as reinforcement in composite materials. *Mater. Res.* **2013**, *16*, 903-923.
(21) Smit, A.; Huijgen, W. Effective fractionation of lignocellulose in herbaceous biomass and hardwood using a mild acetone organosolv process. *Green Chem.* **2017**, *19* (22), 5505-5514.
(22) Mann, D. G. J.; Labbé, N.; Sykes, R. W.; Gracom, K.; Kline, L.; Swamidoss, I. M.; Burris, J. N.; Davis, M.; Stewart, C. N. Rapid assessment of lignin content and structure in switchgrass (Panicum virgatum L.) grown under different environmental conditions. *Bioenergy Res.* **2009**, *2*, 246-256.
(23) Kim, P.; Johnson, A. M.; Essington, M. E.; Radosevich, M.; Kwon, W.-T.; Lee, S.-H.; Rials, T. G.; Labbé, N. Effect of pH on surface characteristics of switchgrass-derived biochars produced by fast pyrolysis. *Chemosphere* **2013**, *90* (10), 2623-2630.

(24) Kim, S. M.; Dien, B. S.; Singh, V. Promise of combined hydrothermal/chemical and mechanical refining for pretreatment of woody and herbaceous biomass. *Biotechnol. Biofuels* **2016**, *9* (1), 97. DOI: 10.1186/s13068-016-0505-2.
(25) Nhuchhen, D. R.; Basu, P.; Acharya, B. A comprehensive review on biomass torrefaction. *Int. J. Renew. Energy Biofuels* **2014**, *2014*, 1-56.
(26) Edmunds, C. W.; Reyes Molina, E. A.; André, N.; Hamilton, C.; Park, S.; Fasina, O.; Adhikari, S.; Kelley, S. S.; Tumuluru, J. S.; Rials, T. G. Blended feedstocks for thermochemical conversion: biomass characterization and bio-oil production from switchgrass-pine residues blends. *Front. Energy Res.* **2018**, *6*, 79.
(27) Rajan, K.; Djioleu, A.; Kandhola, G.; Labbé, N.; Sakon, J.; Carrier, D. J.; Kim, J.-W. Investigating the effects of hemicellulose pre-extraction on the production and characterization of loblolly pine nanocellulose. *Cellulose* **2020**, *27* (7), 3693-3706.
(28) Menon, V.; Rao, M. Trends in bioconversion of lignocellulose: biofuels, platform chemicals & biorefinery concept. *Prog. Energy Combust. Sci.* **2012**, *38* (4), 522-550.
(29) Stanton, B. J.; Bourque, A.; Coleman, M.; Eisenbies, M.; Emerson, R. M.; Espinoza, J.; Gantz, C.; Himes, A.; Rodstrom, A.; Shuren, R. The practice and economics of hybrid poplar biomass production for biofuels and bioproducts in the Pacific Northwest. *Bioenergy Res.* **2021**, *14*, 543-560.
(30) Wang, Y.; Radosevich, M.; Hayes, D.; Labbé, N. Compatible Ionic liquid-cellulases system for hydrolysis of lignocellulosic biomass. *Biotechnol. Bioeng.* **2011**, *108* (5), 1042-1048.
(31) Li, Y. Deep Learning based Prediction of Clogging Occurrences during Lignocellulosic Biomass Feeding in Screw Conveyors. M.S., The University of Tennessee, 2021.
(32) Yu, M.; Womac, A. R.; Igathinathane, C.; Ayers, P. D.; Buschermohle, M. J. Switchgrass ultimate stresses at typical biomass conditions available for processing. *Biomass Bioenergy* **2006**, *30* (3), 214-219.
(33) Stasiak, M.; Molenda, M.; Bańda, M.; Wiącek, J.; Parafiniuk, P.; Lisowski, A.; Gancarz, M.; Gondek, E. Mechanical characteristics of pine biomass of different sizes and shapes. *Eur. J. Wood Wood Prod.* **2019**, *77*, 593-608.
(34) Blau, P. Experimental aspects of friction research on the macroscale. In *Fundamentals of Tribology and Bridging the Gap Between the Macro- and Micro/Nanoscales*, Springer, 2001; pp 261-278.
(35) Mollon, G.; Quacquarelli, A.; Andò, E.; Viggiani, G. Can friction replace roughness in the numerical simulation of granular materials? *Granul. Matter* **2020**, *22*, 1-16.

(36) Wójcik, A.; Frączek, J.; Wota, A. K. The methodical aspects of the friction modeling of plant granular materials. *Powder Technol.* **2019**, *344*, 504-513.
(37) Stasiak, M.; Molenda, M.; Bańda, M.; Horabik, J.; Wiącek, J.; Parafiniuk, P.; Wajs, J.; Gancarz, M.; Gondek, E.; Lisowski, A. Friction and Shear Properties of Pine Biomass and Pellets. *Materials* **2020**, *13* (16), 3567.
(38) Jaeger, H. M.; Nagel, S. R.; Behringer, R. P. Granular solids, liquids, and gases. *Rev. Mod. Phys.* **1996**, *68* (4), 1259-1273. DOI: 10.1103/RevModPhys.68.1259.
(39) Jenike, A. Steady gravity flow of frictional-cohesive solids in converging channels. *J Appl Mech* **1964**, *31*, 5-11.
(40) Wang, X.; Zhang, Q.; Huang, Y.; Ji, J. An efficient method for determining DEM parameters of a loose cohesive soil modelled using hysteretic spring and linear cohesion contact models. *Biosys. Eng.* **2022**, *215*, 283-294.
(41) Yi, H.; J. Lanning, C.; Slosson, J. C.; Wamsley, M. J.; Puri, V. M.; Dooley, J. H. Determination of fundamental mechanical properties of biomass using the cubical triaxial tester to model biomass flow. *Biofuels* **2022**, *13* (8), 945-956.
(42) Miccio, F.; Barletta, D.; Poletto, M. Flow properties and arching behavior of biomass particulate solids. *Powder Technol.* **2013**, *235*, 312-321.
(43) Mudryk, K.; Hutsol, T.; Wrobel, M.; Jewiarz, M.; Dziedzic, B. Determination of friction coefficients of fast-growing tree biomass. *Eng. Rural. Dev.* **2019**, 1568-1573.
(44) Sanjeev, K. C.; Adhikari, S.; Jackson, R. L.; Jain, N. Friction and wear properties of biomass-derived oils via thermochemical conversion processes. *Biomass Bioenergy* **2021**, *155*, 106269.
(45) Zhou, Y.; Wright, B.; Yang, R.; Xu, B. H.; Yu, A.-B. Rolling friction in the dynamic simulation of sandpile formation. *Physica A* **1999**, *269* (2-4), 536-553.
(46) Stefanow, D.; Dudziński, P. A. Soil shear strength determination methods–State of the art. *Soil Tillage Res* **2021**, *208*, 104881.
(47) Aghaei, A. A.; Soroush, A.; Reyhani, M. Large-scale triaxial testing and numerical modeling of rounded and angular rockfill materials. *Sci. Iranica* **2010**, *17* (3).
(48) Teunou, E.; Fitzpatrick, J. J.; Synnott, E. C. Characterisation of food powder flowability. *J. Food Eng.* **1999**, *39* (1), 31-37.
(49) Juliano, P.; Barbosa-Cánovas, G. V. Food powders flowability characterization: theory, methods, and applications. *Annu. Rev. Food Sci. Technol.* **2010**, *1*, 211-239.

(50) Lajeunesse, E.; Mangeney-Castelnau, A.; Vilotte, J. Spreading of a granular mass on a horizontal plane. *Phys. Fluids* **2004**, *16* (7), 2371-2381.
(51) Briend, R.; Radziszewski, P.; Pasini, D. Virtual soil calibration for wheel–soil interaction simulations using the discrete-element method. *Can. Aeronaut. Space J.* **2011**, *57* (1), 59-64.
(52) Johnston, L. J.; Goihl, J.; Shurson, G. C. Selected additives did not improve flowability of DDGS in commercial systems. *Appl. Eng. Agric.* **2009**, *25* (1), 75-82.
(53) Al-Hashemi, H. M. B.; Al-Amoudi, O. S. B. A review on the angle of repose of granular materials. *Powder Technol.* **2018**, *330*, 397-417.
(54) Pitanga, H. N.; Gourc, J.-P.; Vilar, O. M. Interface shear strength of geosynthetics: evaluation and analysis of inclined plane tests. *Geotext. Geomembr.* **2009**, *27* (6), 435-446.
(55) Jian, F.; Jayas, D. S. *Grains: Engineering fundamentals of drying and storage*; CRC Press, 2021.
(56) Sung, W. C.; Kim, J. Y.; Chung, S. W.; Kim, D.; Park, A. H. A.; Lee, D. H. CPFD simulation on angle of repose with hopper geometries and particle properties. *Can. J. Chem. Eng.* **2023**, *101* (1), 147-159.
(57) Fu, J.-J.; Chen, C.; Ferellec, J.-F.; Yang, J. Effect of particle shape on repose angle based on hopper flow test and discrete element method. *Adv. Civ. Eng.* **2020**, 1-10.
(58) ASTM, I. *E871-82: Standard Test Method for Moisture Analysis of Particulate Wood Fuels*; West Conshohocken. PA, 2013.
(59) ASTM, I. *E1755-01: Standard Test Method for Ash in Biomass*; West Conshohocken. PA, 2020.
(60) ASTM, I. *E872-82: Standard test method for volatile matter in the analysis of particulate wood fuels*; West Conshohocken. PA, 2013.
(61) Sluiter, A.; Ruiz, R.; Scarlata, C.; Sluiter, J.; Templeton, D. Determination of extractives in biomass. *Laboratory Analytical procedure (LAP)* **2005**, *1617*, 1-9.
(62) López-Bascón, M. A.; De Castro, M. D. L. Soxhlet extraction. In *Liquid-phase extraction*, Elsevier, 2020; pp 327-354.
(63) Sluiter, A.; Hames, B.; Ruiz, R.; Scarlata, C.; Sluiter, J.; Templeton, D.; Crocker, D. Determination of structural carbohydrates and lignin in biomass. *Laboratory analytical procedure* **2010**, (TP-510-42618).
(64) ASTM, I. *E1131-08: Standard test method for compositional analysis by thermogravimetry*; West Conshohocken. PA, 2008.
(65) ASTM, I. *D5550-14: Standard test methods for specific gravity of soil solids by water pycnometer*; West Conshohocken. PA, 2014.

(66) ASTM, I. *D7891-15: Standard Test Method for Shear Testing of Powders Using the Freeman Technology FT4 Powder Rheometer Shear Cell*; Wes, 2020.
(67) Vasilenko, A.; Koynov, S.; Glasser, B. J.; Muzzio, F. J. Role of consolidation state in the measurement of bulk density and cohesion. *Powder Technol.* **2013**, *239*, 366-373.
(68) Astm, D. Standard Test Methods for Apparent Density, Bulk Factor, and Pourability of Plastic Materials. ASTM International West Conshohocken, PA, USA: 2017.
(69) Podlozhnyuk, A.; Pirker, S.; Kloss, C. Efficient implementation of superquadric particles in Discrete Element Method within an open-source framework. *Comput. Part. Mech.* **2017**, *4* (1), 101-118.
(70) Roessler, T.; Katterfeld, A. DEM parameter calibration of cohesive bulk materials using a simple angle of repose test. *Particuology* **2019**, *45*, 105-115.
(71) Sirisomboon, P.; Kitchaiya, P. Physical properties of Jatropha curcas L. kernels after heat treatments. *Biosys. Eng.* **2009**, *102* (2), 244-250.
(72) Cho, G.-C.; Dodds, J.; Santamarina, J. C. Particle shape effects on packing density, stiffness, and strength: natural and crushed sands. *J. Geotech. Geoenviron. Eng.* **2006**, *132* (5), 591-602.
(73) Tian, Y.; Zhou, M.-q.; Wu, Z.-k.; Wang, X.-c. A region-based active contour model for image segmentation. In *2009 International Conference on Computational Intelligence and Security*, 2009, 2009; IEEE: Vol. 1, pp 376-380.
(74) ASTM, I. *D7181-20: Standard test method for consolidated drained triaxial compression test for soils*; West Conshohocken, PA, 2020.
(75) Colliat-Dangus, J. L.; Desrues, J.; Foray, P. Triaxial testing of granular soil under elevated cell pressure. In *Advanced triaxial testing of soil and rock*, ASTM International, 1988.
(76) Hanley, K. J.; Huang, X.; O'Sullivan, C. Energy dissipation in soil samples during drained triaxial shearing. *Géotechnique* **2018**, *68* (5), 421-433.
(77) Kokusho, T. Cyclic triaxial test of dynamic soil properties for wide strain range. *Soils Found.* **1980**, *20* (2), 45-60.
(78) Taborda, D. M. G.; Pedro, A. M. G.; Pirrone, A. I. A state parameter-dependent constitutive model for sands based on the Mohr-Coulomb failure criterion. *Comput Geotech* **2022**, *148*, 104811.
(79) Lu, X.; Hsu, C. T. Tangent Poisson's ratio of high-strength concrete in triaxial compression. *Mag. Concr. Res.* **2007**, *59* (1), 69-77.

(80) Yokota, K.; Konno, M. Dynamic Poisson's ratio of soil. In *7th World Conference Earthquake Engineering*, Istanbul, 1980, 1980; Vol. 3, pp 418-475.
(81) Labuz, J. F.; Zang, A. Mohr–Coulomb failure criterion. In *The ISRM Suggested Methods for Rock Characterization, Testing and Monitoring: 2007-2014*, Springer, 2012; pp 227-231.
(82) Lemus, R.; Brummer, E. C.; Moore, K. J.; Molstad, N. E.; Burras, C. L.; Barker, M. F. Biomass yield and quality of 20 switchgrass populations in southern Iowa, USA. *Biomass Bioenergy* **2002**, *23* (6), 433-442.
(83) Lindsey, K.; Johnson, A.; Kim, P.; Jackson, S.; Labbé, N. Monitoring switchgrass composition to optimize harvesting periods for bioenergy and value-added products. *Biomass Bioenergy* **2013**, *56*, 29-37.
(84) Regmi, B.; Dutta, A.; Pradhan, R. R.; Arku, P. Physicochemical characteristics and pyrolysis kinetics of raw and torrefied hybrid poplar wood (NM6–Populus nigra). *Biofuels* **2020**, *11* (3), 329-338.
(85) Via, B. K.; Adhikari, S.; Taylor, S. Modeling for proximate analysis and heating value of torrefied biomass with vibration spectroscopy. *Bioresour. Technol.* **2013**, *133*, 1-8.
(86) Mante, O. D.; Agblevor, F. Catalytic pyrolysis for the production of refinery-ready biocrude oils from six different biomass sources. *Green Chem.* **2014**, *16* (6), 3364-3377.
(87) Edmunds, C. W.; Hamilton, C.; Kim, K.; Chmely, S. C.; Labbé, N. Using a chelating agent to generate low ash bioenergy feedstock. *Biomass Bioenergy* **2017**, *96*, 12-18.
(88) San Miguel, G.; Sánchez, F.; Pérez, A.; Velasco, L. One-step torrefaction and densification of woody and herbaceous biomass feedstocks. *Renew. Energ.* **2022**, *195*, 825-840.
(89) Tumuluru, J. S. Effect of pellet die diameter on density and durability of pellets made from high moisture woody and herbaceous biomass. *Carbon Resour. Convers.* **2018**, *1* (1), 44-54.
(90) Saha, B. C. Hemicellulose bioconversion. *J. Ind. Microbiol. Biotechnol.* **2003**, *30* (5), 279-291.
(91) Oberlerchner, J. T.; Rosenau, T.; Potthast, A. Overview of methods for the direct molar mass determination of cellulose. *Molecules* **2015**, *20* (6), 10313-10341.
(92) Lam, P. S.; Sokhansanj, S.; Bi, X.; Lim, C.; Naimi, L.; Hoque, M.; Mani, S.; Womac, A. R.; Narayan, S.; Ye, X. Bulk density of wet and dry wheat straw and switchgrass particles. *Appl. Eng. Agric.* **2008**, *24* (3), 351-358.

(93) Karamchandani, A.; Yi, H.; Puri, V. M. Fundamental mechanical properties of ground switchgrass for quality assessment of pellets. *Powder Technol.* **2015**, *283*, 48-56.
(94) Ogden, C. A.; Ileleji, K. E. Physical characteristics of ground switchgrass related to bulk solids flow. *Powder Technol.* **2021**, *385*, 386-395.
(95) Olatunde, G.; Fasina, O.; McDonald, T.; Adhikari, S.; Duke, S. Moisture effect on fluidization behavior of loblolly pine Wood grinds. *Biomass Convers. Biorefin.* **2017**, *7*, 207-220.
(96) Morales-Vera, R.; Bura, R.; Gustafson, R. Handling heterogeneous hybrid poplar particle sizes for sugar production. *Biomass Bioenergy* **2016**, *91*, 126-133.
(97) Lam, P. S.; Lam, P. Y.; Sokhansanj, S.; Bi, X.; Lim, C. J.; Sidders, D.; Melin, S. Evaluation of hybrid poplar and salix (Salix) biomass for pellet production. In *2010 ASABE Annual International Meeting*, Pittsburgh, Pennsylvania, June 20-June 23, 2010, 2010; American Society of Agricultural and Biological Engineers.
(98) Sundar, S.; Bergey, N. S.; Salamanca-Cardona, L.; Stipanovic, A.; Driscoll, M. Electron beam pretreatment of switchgrass to enhance enzymatic hydrolysis to produce sugars for biofuels. *Carbohydr. Polym.* **2014**, *100*, 195-201. DOI: https://doi.org/10.1016/j.carbpol.2013.04.103.
(99) Damartzis, T.; Vamvuka, D.; Sfakiotakis, S.; Zabaniotou, A. Thermal degradation studies and kinetic modeling of cardoon (Cynara cardunculus) pyrolysis using thermogravimetric analysis (TGA). *Bioresour. Technol.* **2011**, *102* (10), 6230-6238.
(100) Chinwan, D.; Castell-Perez, M. E. Effect of conditioner and moisture content on flowability of yellow cornmeal. *Food Sci. Nutr.* **2019**, *7* (10), 3261-3272.
(101) Lam, P. S.; Sokhansanj, S.; Bi, X.; Lim, C. J. Effect of particle size and shape on physical properties of biomass grinds. In *2008 ASABE Annual International Meeting*, Providence, Rhode Island, June 29–July 2, 2008; American Society of Agricultural and Biological Engineers.
(102) Hu, Z. Physical properties of leached and pelletized agricultural and woody biomass residues. Ph.D., University of British Columbia, 2023.
(103) Xu, G.; Li, M.; Lu, P. Experimental investigation on flow properties of different biomass and torrefied biomass powders. *Biomass Bioenergy* **2019**, *122*, 63-75.
(104) Solarte-Toro, J. C.; González-Aguirre, J. A.; Giraldo, J. A. P.; Alzate, C. A. C. Thermochemical processing of woody biomass: A review focused on energy-driven applications and catalytic upgrading. *Renew. Sust. Energ. Rev.* **2021**, *136*, 110376.

(105) Vo, T. T.; Nezamabadi, S.; Mutabaruka, P.; Delenne, J.-Y.; Radjai, F. Additive rheology of complex granular flows. *Nat. Commun.* **2020**, *11* (1), 1476.
(106) Nzokou, P.; Kamdem, D. P. J. W.; Science, F. Influence of wood extractives on moisture sorption and wettability of red oak (Quercus rubra), black cherry (Prunus serotina), and red pine (Pinus resinosa). *Wood Fiber Sci.* **2007**, *36* (4), 483-492.
(107) Ashok Kumar, M.; Ramachandra Reddy, G.; Siva Bharathi, Y.; Venkata Naidu, S.; Naga Prasad Naidu, V. Frictional coefficient, hardness, impact strength, and chemical resistance of reinforced sisal-glass fiber epoxy hybrid composites. *J. Compos. Mater.* **2010**, *44* (26), 3195-3202.
(108) Adapa, P. K.; Tabil, L. G.; Schoenau, G. J. Compression characteristics of selected ground agricultural biomass. *Agric. Eng.* **2009**, *XI*.
(109) Kaleem, M. A.; Alam, M. Z.; Khan, M.; Jaffery, S. H. I.; Rashid, B. An experimental investigation on accuracy of Hausner Ratio and Carr Index of powders in additive manufacturing processes. *Met. Powder Rep.* **2020**.
(110) Carr, R. *Powder and granule properties and mechanics*; Marcel Dekker, 1976.
(111) Ogden, C. A. Flow mechanics of switchgrass bulk solid in hoppers under gravity discharge. Ph.D., Purdue University, 2010.
(112) Berdychowski, M.; Talaśka, K.; Malujda, I.; Kukla, M. Application of the Mohr-Coulomb model for simulating the biomass compaction process. In *IOP Conference Series: Materials Science and Engineering*, 2020; IOP Publishing: Vol. 776, p 012066.
(113) Carr, R. *Gas–solids handling in the processing industries: Powder and granule properties and mechanics*; Marcel Dekker, 1976.
(114) Vaid, Y. P.; Chern, J. C. Mechanism of deformation during cyclic undrained loading of saturated sands. *Soil Dyn. Earthquake Eng.* **1983**, *2* (3), 171-177.
(115) Lambe, T. W.; Whitman, R. V. *Soil Mechanics, SI Version (Series in Soil Engineering)*; John Wiley & Sons, 1969.
(116) Helmerius, J.; von Walter, J. V.; Rova, U.; Berglund, K. A.; Hodge, D. B. Impact of hemicellulose pre-extraction for bioconversion on birch Kraft pulp properties. *Bioresour. Technol.* **2010**, *101* (15), 5996-6005.
(117) Karumuri, S.; Hiziroglu, S.; Kalkan, A. K. Thermoset-cross-linked lignocellulose: A moldable plant biomass. *ACS Appl. Mater. Interfaces* **2015**, *7* (12), 6596-6604.
(118) Zong, P.; Jiang, Y.; Tian, Y.; Li, J.; Yuan, M.; Ji, Y.; Chen, M.; Li, D.; Qiao, Y. Pyrolysis behavior and product distributions of biomass six group

components: Starch, cellulose, hemicellulose, lignin, protein and oil. *Energy Convers. Manage.* **2020**, *216*, 112777.
(119) Zhang, N.; Li, S.; Xiong, L.; Hong, Y.; Chen, Y. Cellulose-hemicellulose interaction in wood secondary cell-wall. *Modell. Simul. Mater. Sci. Eng.* **2015**, *23* (8), 085010.
(120) Khodayari, A.; Thielemans, W.; Hirn, U.; Van Vuure, A. W.; Seveno, D. Cellulose-hemicellulose interactions-a nanoscale view. *Carbohydr. Polym.* **2021**, *270*, 118364.
(121) Houfani, A. A.; Anders, N.; Spiess, A. C.; Baldrian, P.; Benallaoua, S. Insights from enzymatic degradation of cellulose and hemicellulose to fermentable sugars–a review. *Biomass Bioenergy* **2020**, *134*, 105481.
(122) Filomena, D.; Ehite, E.; Houston, R.; Li, Y.; Abdoulmoumine, N. The Natural Physical and Chemical Variability of Hardwood Woody Biomass Across the SE Region. In *ASABE 2020 Annual International Meeting*, Virtual, 2020; ASABE. DOI: 10.13140/RG.2.2.14387.86568.
(123) Yan, H.-L.; Li, Z.-K.; Wang, Z.-C.; Lei, Z.-P.; Ren, S.-B.; Pan, C.-X.; Tian, Y.-J.; Kang, S.-G.; Yan, J.-C.; Shui, H.-F. Characterization of soluble portions from cellulose, hemicellulose, and lignin methanolysis. *Fuel* **2019**, *246*, 394-401.
(124) Jakob, M.; Mahendran, A. R.; Gindl-Altmutter, W.; Bliem, P.; Konnerth, J.; Mueller, U.; Veigel, S. The strength and stiffness of oriented wood and cellulose-fibre materials: A review. *Prog. Mater Sci.* **2022**, *125*, 100916.
(125) Yano, H.; Hirose, A.; Collins, P. J.; Yazaki, Y. Effects of the removal of matrix substances as a pretreatment in the production of high strength resin impregnated wood based materials. *J. Mater. Sci. Lett.* **2001**, *20* (12), 1125-1126.
(126) Song, J.; Chen, C.; Zhu, S.; Zhu, M.; Dai, J.; Ray, U.; Li, Y.; Kuang, Y.; Li, Y.; Quispe, N. Processing bulk natural wood into a high-performance structural material. *Nature* **2018**, *554* (7691), 224-228.
(127) Chen, D.; Cen, K.; Zhuang, X.; Gan, Z.; Zhou, J.; Zhang, Y.; Zhang, H. Insight into biomass pyrolysis mechanism based on cellulose, hemicellulose, and lignin: Evolution of volatiles and kinetics, elucidation of reaction pathways, and characterization of gas, biochar and bio-oil. *Combust. Flame* **2022**, *242*, 112142.
(128) Dai, L.; Zhu, W.; Lu, J.; Kong, F.; Si, C.; Ni, Y. A lignin-containing cellulose hydrogel for lignin fractionation. *Green Chem.* **2019**, *21* (19), 5222-5230.
(129) Ye, D.; Chang, C.; Zhang, L. High-strength and tough cellulose hydrogels chemically dual cross-linked by using low-and high-molecular-weight cross-linkers. *Biomacromolecules* **2019**, *20* (5), 1989-1995.

CHAPTER 4.

EXPERIMENTAL AND COMPUTATIONAL INVESTIGATION OF LIGNOCELLULOSIC BIOMASS PARTICLE MORPHOLOGY AND FLOW BEHAVIOR

Disclaimer: This chapter is a draft version of the following article:

Ehite, E. H.; Abdoulmoumine, N. Realistic Representation of Lignocellulosic Biomass Morphology and Flow Behavior Using Spherical and Superquadric Discrete Element Models. In preparation for submission to *Chemical Engineering Science*.

4.1. Introduction

This chapter details the high-fidelity computational modeling of particle assemblies that capture the morphological characteristics of lignocellulosic biomass materials and examine their flow behavior.

Computational modeling techniques, such as the discrete element method (DEM), provide an economical and convenient option for investigating diverse granular particulate systems [1]. A robust computational model can reproduce particle attributes with high accuracy, run physical flow characterization tests using appropriate computing resources, and generate results that can be validated by comparing them with experimental measurements. We can use validated computational models to study the flow of diverse biomass materials, identify potential flow issues, and apply corrective actions at the design stage to optimize the feedstock flow and improve the performance of commercial-scale biorefineries.

The application of DEM modeling techniques to lignocellulosic biomass materials is not straightforward. In early concept applications of discrete element models to materials such as the modeling of pharmaceutical tablets [2], the material attributes, e.g., the morphological (shape factors, size distributions), material, and mechanical properties of the particles, are uniform. On the other hand, lignocellulosic materials exhibit large natural variability in their material attributes, especially non-uniform shapes and wide-ranging size distributions [3]. This variability in size distribution and irregular shapes is exemplified by Figure 4.1, which shows the macro-scale and micro-scale view of a group of switchgrass particles. Capturing the variability in particle morphology is a major challenge in the computational investigation of lignocellulosic biomass materials.

The critical component of developing a DEM model for lignocellulosic biomass particles is the high-fidelity reproduction of real particles in the computational environment. Since real biomass feedstocks can have thousands of particles, the exact recreation is impractical and computationally expensive [4]. Therefore, the DEM process represents real particles by simpler artificial shapes and calculates surface contact forces using specific shape models [5]. The selection of an appropriate particle model must fulfill two criteria: a) suitability, i.e., the ability to visually and geometrically represent the interacting particles, b) computational efficiency, i.e., the ability to analyze the surface functions of the

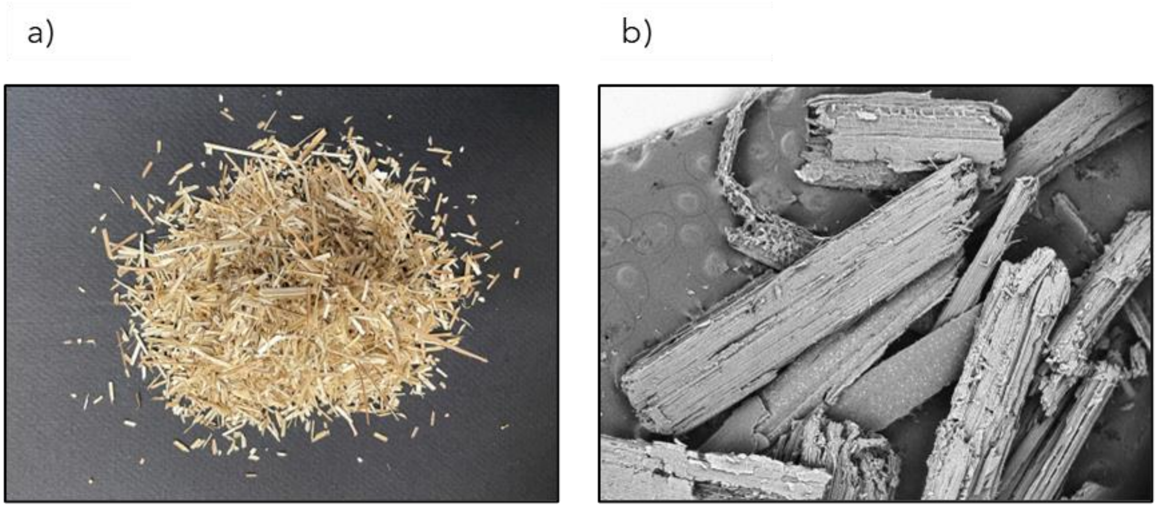

Figure 4.1. a) Macro-scale and b) micro-scale view (scanning electron microscopy images) of switchgrass particles.

particles using available computing power [6].

The most common approach to represent non-uniform DEM particles is the multisphere method, which represents real particles as an agglomeration of interconnected spheres [7]. This method has been prevalent due to its simplicity, well-specified contact models [8], and efficient computational process [9]. In the early application of DEM, real biomass particles were represented by a number of soft, smooth spheres in contact with one another [10-12]. However, granular materials like lignocellulosic biomass are mostly non-spherical. Additionally, non-spherical particle assemblies are more compact and have higher shear and rolling resistance than spherical particles [13]. Thus, the multisphere assumption is not always suitable for granular materials, and complex materials like lignocellulosic biomass materials require a more sophisticated particle model beyond the spherical assumptions [14]. Researchers have considered more complex shapes for non-spherical particles, including sphero-cylinders [15], sphero-polyhedrons [16, 17], and composite-polygons [18]. The efficiency and scalability of these models depend on the number of segments being considered (e.g., faces of the polyhedrons, spherical joints of the sphero-cylinders, and smoothed edges and corners for the polygons) [19].

Additionally, they require specially developed contact detection algorithms. Solving the particle interactions for particulate biomass systems using iterative contact detection models can be extremely time-consuming. As a result, these complex particle representations have very high computational costs [20]. Therefore, finding a shape representation process that can suitably reproduce the particles with high fidelity is necessary while ensuring reasonable computational efficiency.

The superquadric particle shape representation method, postulated by Barr [21], has been a potential solution for modeling non-spherical particles. Superquadrics are polynomials with non-negative real exponents, and they have associated geometric parameters that influence the shape factors, dimensions, and curvature of the surfaces [22]. A superquadric particle is expressed in three-dimensional space as a set of points (x, y, z), which satisfies the superquadric equation (Equation 4.1) [21, 23].

$$\left(\left|\frac{x}{a}\right|^{n_2} + \left|\frac{y}{b}\right|^{n_2}\right)^{\frac{n_1}{n_2}} + \left|\frac{z}{c}\right|^{n_1} \leq 1, \tag{4.1}$$

where, a, b, c = particle half-lengths along the principal axes, n_1, n_2 = blockiness parameters ($n_i = 1,2,3, \ldots$).

By changing these five parameters ($a, b, c, n_1, and\ n_2$), the equation can provide a variety of shapes. For example, $a = b = c, n_1 = n_2 = 2$ provides a sphere, $a = b = c, n_1$"$2, n_2 = 2$ provides a cylinder, and $a = b = c, n_1$"$2, n_2$"2 provides a box. A well-calibrated superquadric particle simulation can provide similar results to a multi-sphere model in equal or less computational time [24-26]. Thus, the superquadric particle assumption can provide an optimum balance between the model accuracy and capturing the realistic particle shape [27].

Superquadric particle representation has been successfully applied to discrete element modeling by computational scientists to model diverse sets of particles [23, 24, 28-30]. Furthermore, the developed superquadric model can be validated using experimental measurements and for predicting material behavior in particle scale, including their flow in various conveyance systems.

A major limitation of state-of-the-art superquadric models is the absence of a standardized method for determining superquadric parameters, i.e., the length of half axes and the blockiness parameters. Traditional size measurement techniques are unsuitable for finding the particle shape parameters in three dimensions [31]. Alternative digital imaging techniques such as using a digital scanner [32], scanning electron microscope [33, 34], or dynamic image analysis [35, 36] provide high-fidelity particle images, but the selection of the appropriate particle size and shape parameters from these images becomes important. Among the different parameters used for the analysis of particle size and its distribution, e.g., in a powder or a polycrystalline solid, Feret parameters are popular for relating the projections of three-dimensional objects on a two-dimensional plane [37]. Feret length, width, and thickness of granular particles can represent the shape or form along principal axes and can provide the length of half axes of the superquadric particles. Similarly, the corner curvatures, represented by roundness and sphericity, can be translated into blockiness parameters [38, 39]. Therefore, we can use existing digital imaging technologies to capture the particle morphological parameters and render realistic particle shapes in a superquadric DEM model.

This study aims to capture the real lignocellulosic biomass morphology and flow behaviors by experimental morphological parameter measurements and superquadric discrete element computational models. We hypothesize that if we can experimentally approximate the necessary particle parameters and combine them with superquadric particle assumptions, we can reasonably represent real particle morphology and model lignocellulosic biomass flow comparable with complex particle approximation. We will test our hypothesis by i) determining the appropriate morphological, material, and mechanical properties of switchgrass, loblolly pine, and hybrid poplar feedstocks, ii) developing computational models with appropriate particle shapes and size distribution to represent the biomass particle assemblies, and iii) examining the flow behavior of particle assemblies during an angle of repose test.

4.2. Materials and Methods

4.2.1. Sample Particle Selection

We chose the three groups of lignocellulosic biomass particle batches (same as Objective 1) for this computational research study: switchgrass (herbaceous), hybrid poplar (hardwood), and loblolly pine (softwood), as they represent different bioenergy-relevant feedstocks commonly used in lignocellulosic biorefineries. Additionally, these particles show non-spherical characteristics (sphericity <0.5), representing "real" or "irregularly shaped" particles.

Figure 4.2 illustrates the herbaceous and woody biomass samples used in our research.

4.2.2. Sample Material Characterization

We conducted an extensive literature review to ascertain the material and interaction properties that previous DEM researchers deemed critical for particulate systems. First, we conducted experimental measurements of the bulk and particle density of the sample materials using the method described in Chapter 3, Section 3.2.2. Next, we selected appropriate values based on available DEM literature for the rest of the particle-particle and wall material

Figure 4.2. Herbaceous and woody biomass sample materials.

properties. Finally, we calculated the particle-wall interaction properties by taking an average of the experimentally measured particle and wall material properties from the literature.

Table 4.1 lists the material and interaction properties values for the different sample batches used for generating our baseline model.

4.2.3. Particle Morphology Representation

We performed a particle image analysis of the samples from each batch to quantify the particle size distribution and its external shape characteristics.

We analyzed the dynamic particle in a dynamic, quasi-3D particle image analyzer (PartAn3D Pro, Microtrac, York, PA, USA). The dynamic image analysis method involves loading particle samples into the vibratory funnel that induces particles to fall through the instrument's opening. As these particles fall along the measurement field of high-resolution digital cameras, they capture the particle shadows' projection at a high frame rate providing quasi-3D reconstructed images. The built-in software processes the camera feeds to generate particle images at different orientations; size distribution-based predefined bins, and size and shape parameters.

Figure 4.3 describes the particle tracking and image capture process by the dynamic particle analyzer.

Table 4.1. Material and interaction properties used in baseline DEM model for switchgrass, loblolly pine, and hybrid poplar samples.

Parameter	Switchgrass	Loblolly Pine	Hybrid Poplar
Density of particles (kg/m^3)	135	214	165
Young's modulus wall [MPa]	1.93×10^8	1.93×10^8	1.93×10^8
Young's modulus particles [MPa]	3.24×10^8	3.24×10^8	3.24×10^8
Poisson's ratio wall [-]	0.25	0.25	0.25
Poisson's ratio particle-particle [-]	0.4	0.4	0.4
Coefficient of restitution wall [-]	0.6	0.6	0.6
Coefficient of restitution particle-particle [-]	0.6	0.6	0.6
Coefficient of sliding friction wall [-]	0.3	0.3	0.3
Coefficient of sliding friction particle-particle [-]	0.36	0.36	0.36
Coefficient of rolling friction wall [-]	0.8	0.8	0.8
Coefficient of rolling friction particle-particle [-]	0.8	0.8	0.8
Coefficient of restitution particle-wall [-]	0.6	0.6	0.6
Coefficient of sliding friction particle-wall [-]	0.36	0.36	0.36
Coefficient of rolling friction particle-wall [-]	5×10^{-4}	5×10^{-4}	5×10^{-4}
Time step [s]	10^{-5}	10^{-5}	10^{-5}

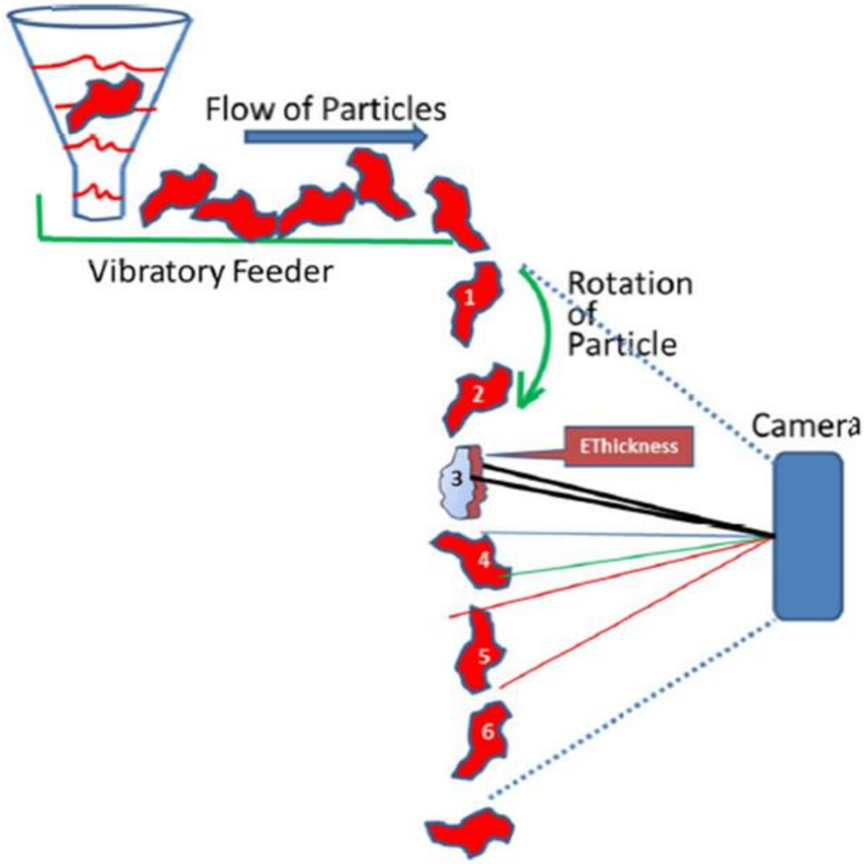

Figure 4.3. Particle tracking process for the dynamic particle analyzer (PartAn3D Pro) used for particle shape and size distribution analysis.

We measured the following parameters using this approach:

i) Size distribution (percentage of particles in each size bin),

ii) Area equivalent diameter ($D_a = (4Area/\pi)1/2$),

iii) Feret length (FL),

iv) Feret width (FW),

v) Feret thickness (FT),

vi) Roundness ($Rp = (4Area/\pi(FL)^2)$), and

vii) Sphericity ($Sp = \frac{D_a}{D_p}$,

where, $D_p = Perimeter\ equivalent\ diameter\ =\ Perimeter/\pi$).

We used approximately 10g of material (~50,000 particles) for each image analysis experiment and conducted our analysis in triplicates of the sample batch. We measured three imaging replicates for each particle group and reported the averages. After the particle dynamic analysis, we selected the particle size bins covering the majority (~99%) of the total particle size distribution. We then used the Feret length (FL_{PA}) and Feret width (FW_{PA}) to calculate the average particle area for each particle bin ($Area_{PA} = FL_{PA} \times FW_{PA}$).

Next, we conducted a digital image scanning of the particle bins with an Epson Perfection V39 high-resolution scanner (Epson America, Inc., Long Beach, CA) at a resolution of 300 dpi (dots per inch). Before scanning, we scattered the particles without overlapping on an opaque white sheet. We analyzed the captured images with a custom-built program in the MATLAB software (The MathWorks Inc., Natick, MA), which determines their area ($Area_{IS}$) and Feret length (FL_{IS}), from which we can calculate the Feret width ($FW_{IS} = \frac{Area_{IS}}{FL_{IS}}$). We then determined the initial error between the image scanning and dynamic particle analysis using Equation 4.2.

$$y'_{ini} = \frac{Area_{PA} - Area_{IS}}{Area_{IS}}, \tag{4.2}$$

We then conducted an optimization process to minimize the error. For this purpose, we considered the FW_{IS} while adjusting the FL_{IS} value until the y'_{corr} is minimum. We then use the corrected Feret length (FL_{corr}) and the image scanned Feret length value (FW_{IS}) to be the half-length axes in the x and y direction for the superquadric particles ($a\ and\ b\ in\ Equation\ 4.1$). We used the Feret thickness from particle analysis FT to be the final half-length parameter (c).

Finally, we used the roundness, Rp, and sphericity, Sp values to determine the blockiness parameters ($n_1\ and\ n_2$). We repeated the process for each particle bin and used the superquadric particle parameters in the DEM model's input script in LIGGGHTS.

Figure 4.4 shows a superquadric particle generated in MATLAB using size and shape parameters from the dynamic particle analysis and error minimization and the DEM particle assembly in LIGGHTS with same size parameters.

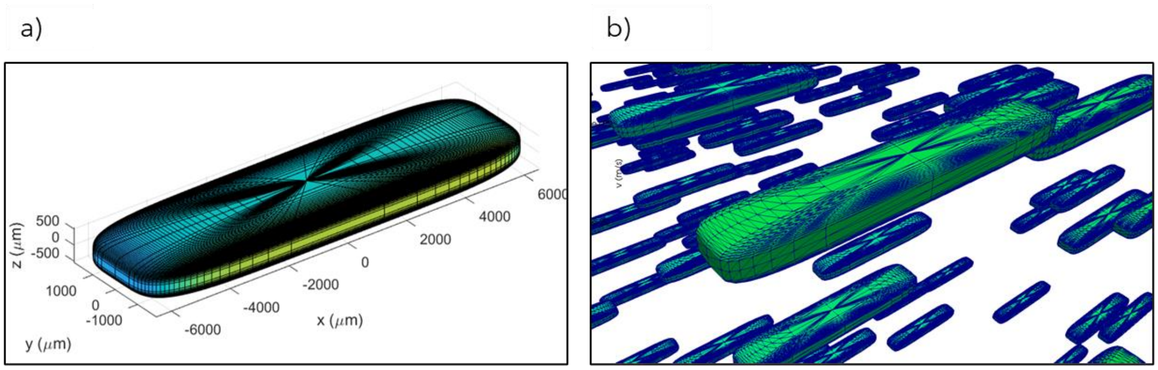

Figure 4.4. Particle image from a) dynamic image analysis and error minimization, b) Particle assembly in DEM model.

4.2.4. Computational Model Generation

We conducted our flow simulations of the batches using the open-source DEM software LIGGGHTS (LAMMPS improved for general granular and granular heat transfer simulations) (version: LIGGGHTS-PUBLIC 3.8, DCS Computing GmbH, Linz, Austria). In addition, we conducted the post-processing of the simulations from the LIGGGHTS using the analysis and visualization software ParaView (version: 5.8.0 64-bit, Kitware Inc., New York, NY, USA). We performed the LIGGGHTS simulations on the University of Tennessee's HPC cluster ISAAC, which has a 40-core Intel Skylake computing node with 192 GB RAM (Intel Gold 6148, Intel Corporation, Santa Clara, CA, USA. We ran the simulations in LIGGGHTS in batch mode using four cores, each consisting of 16GB RAM. Our simulations used a critical time step value of 20% of the Rayleigh time.

We used the default superquadric contact model in LIGGGHTS-DEM (based on the Hertz-Mindlin contact theory) for particle-particle and particle-wall interactions [40].

We characterized the flow of the particle assemblies using a hollow cylinder angle of repose test [41]. The computational domain is a quasi-3d plane hopper with the same dimensions as the experimental setup, i.e., i.e., inner diameter, ID = 0.04 m, and cylinder height, CH = 0.20m. The particles are generated in an insertion face located vertically above the top of the cylinder and then fill inside the cylinder (m_{fill}), allowing them to settle under gravity. Then, the cylinder travels vertically at a velocity of 0.1 m/s, and the material flows from the lifting cylinder on the flat surface, forming a material pile.

After completing the final simulation, we calculated several quantitative parameters from the model and compared them with the experimental outcomes, namely bulk density, pile diameter, and angle of repose.

We measured the fill height of the particles inside the hopper (h_{fill}) after the particles had settled inside the cylinder and before the vertical motion was initiated. We then calculated the bulk density of the material using Equation 4.3.

$$\rho_{bulk} = \frac{m_{fill}}{\pi(ID/4)^2 h_{fill}} \tag{4.3}$$

We captured two-dimensional images of the pile in the XY plane at the end of our simulation. We then processed the same MATLAB image and segmentation process as described in the image processing section of 3.2.3.1 to calculate the angle of repose. We also captured two-dimensional images of the pile in the YZ plane and circumscribed a circle to the area covered by the pile. The circle's radius represents the particles' spread after the test.

Figure 4.5 shows the isometric and front views of the computational domain used for the hollow cylinder angle of repose test.

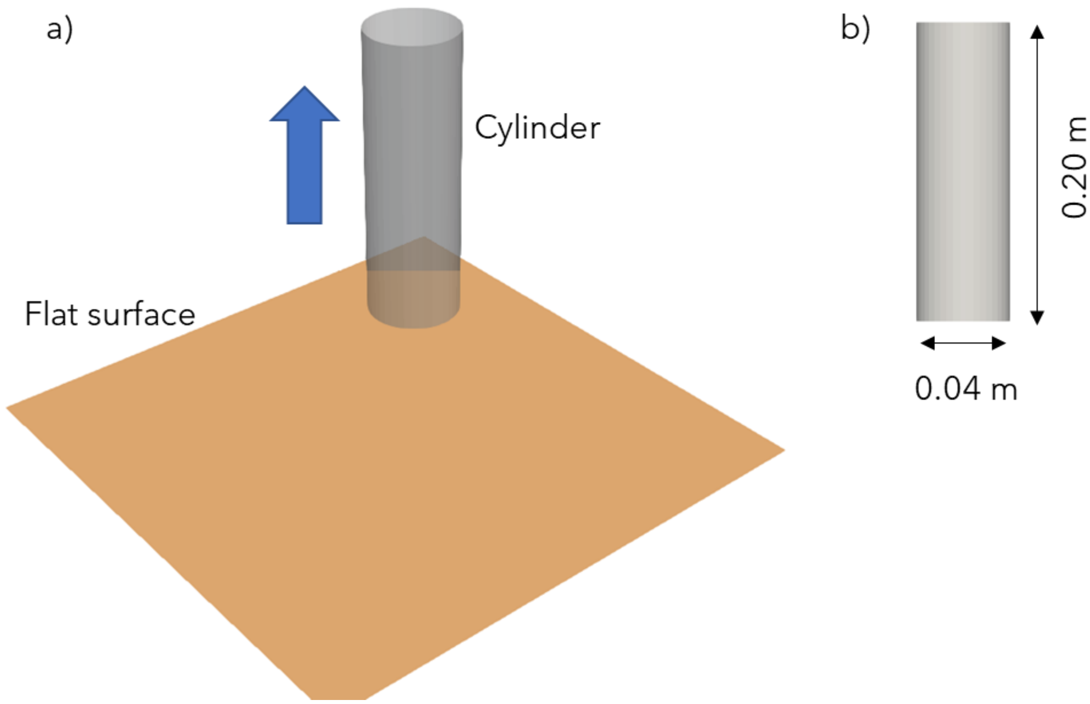

Figure 4.5. Computational domain of the hollow cylinder angle of repose test. a) isometric view, b) front view.

4.3. Results

4.3.1. Particle Morphology Representation

Table 4.2 summarizes the results after the morphological feature extraction by dynamic particle size analysis and error minimization process for switchgrass, loblolly pine, and hybrid poplar samples. The results show that five particle size bins constitute nearly 99% of their total particle batch by volume.

We used only these five bins for the particle distribution in LIGGGHTS and used their related Feret dimensions (as the length of half-axes, a, b, and c) and the roundness and sphericity values (for blockiness parameters, n1, and n2) for creating the superquadric particles.

4.3.2. Computational Model Output: Fill Parameters

We show still images from the angle of repose tests from the computational model and physical experiment for switchgrass, loblolly pine, and hybrid poplar samples in Figure 4.6 and Figure 4.7. The visual results indicate that we can achieve similarity in the particle shape and size distribution for both experiments and simulations.

Table 4.3 provides quantitative parameters from DEM simulations and physical experiments for switchgrass, loblolly pine, and hybrid poplar samples.

Table 4.2. Dynamic particle analysis results for the switchgrass, loblolly pine, and hybrid poplar samples.

Material: Switchgrass

Particle size	Volume	Feret length, FL	Feret width, FW	Feret thickness, FT	Roundness	Sphericity	n1	n2
mm	%	mm	mm	mm				
40	36	3	19.2	5	0.41	0.34	6	6
30	33	3	31.9	5	0.52	0.49	5	5
20	17	3	23.1	5	0.56	0.15	5	5
10	9	3	18.9	4	0.37	0.29	6	6
5	5	2.5	5.25	5	0.44	0.41	5	5

Material: Loblolly Pine

Particle size	Volume	Feret length, FL	Feret width, FW	Feret thickness, FT	Roundness	Sphericity	n1	n2
mm	%	mm	mm	mm				
20	34	2.5	3.5	5	0.46	0.29	6	6
16	28	2.5	12.3	5	0.52	0.49	5	5
12	22	2.5	7.5	4	0.51	0.31	5	5
8	11	2.5	9.8	3	0.39	0.28	6	6
4	5	2.5	5.25	5	0.49	0.55	5	5

Material: Hybrid Poplar

Particle size	Volume	Feret length, FL	Feret width, FW	Feret thickness, FT	Roundness	Sphericity	n1	n2
mm	%	mm	mm	mm				
20	40	3.5	9.4	5	0.32	0.41	6	6
16	26	3.5	15.0	5	0.58	0.49	5	5
12	22	3.5	12.1	3	0.5	0.47	5	5
8	7	3.5	9.2	3	0.37	0.29	6	6
4	5	3.5	15.6	4	0.55	0.49	5	5

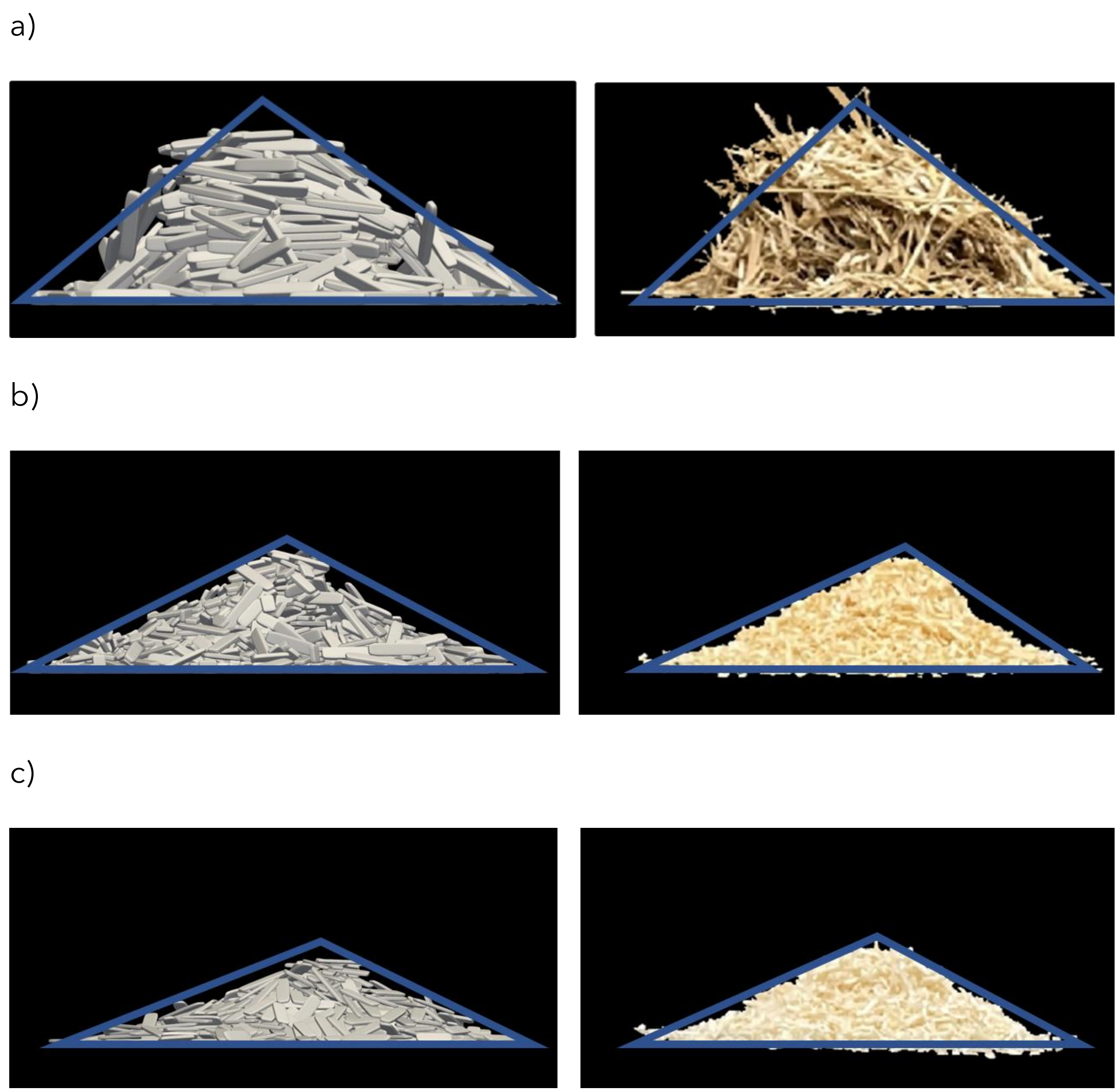

Figure 4.6. Front view of material piles from simulation and experiment after image processing for a) switchgrass, b) loblolly pine, and c) hybrid poplar.

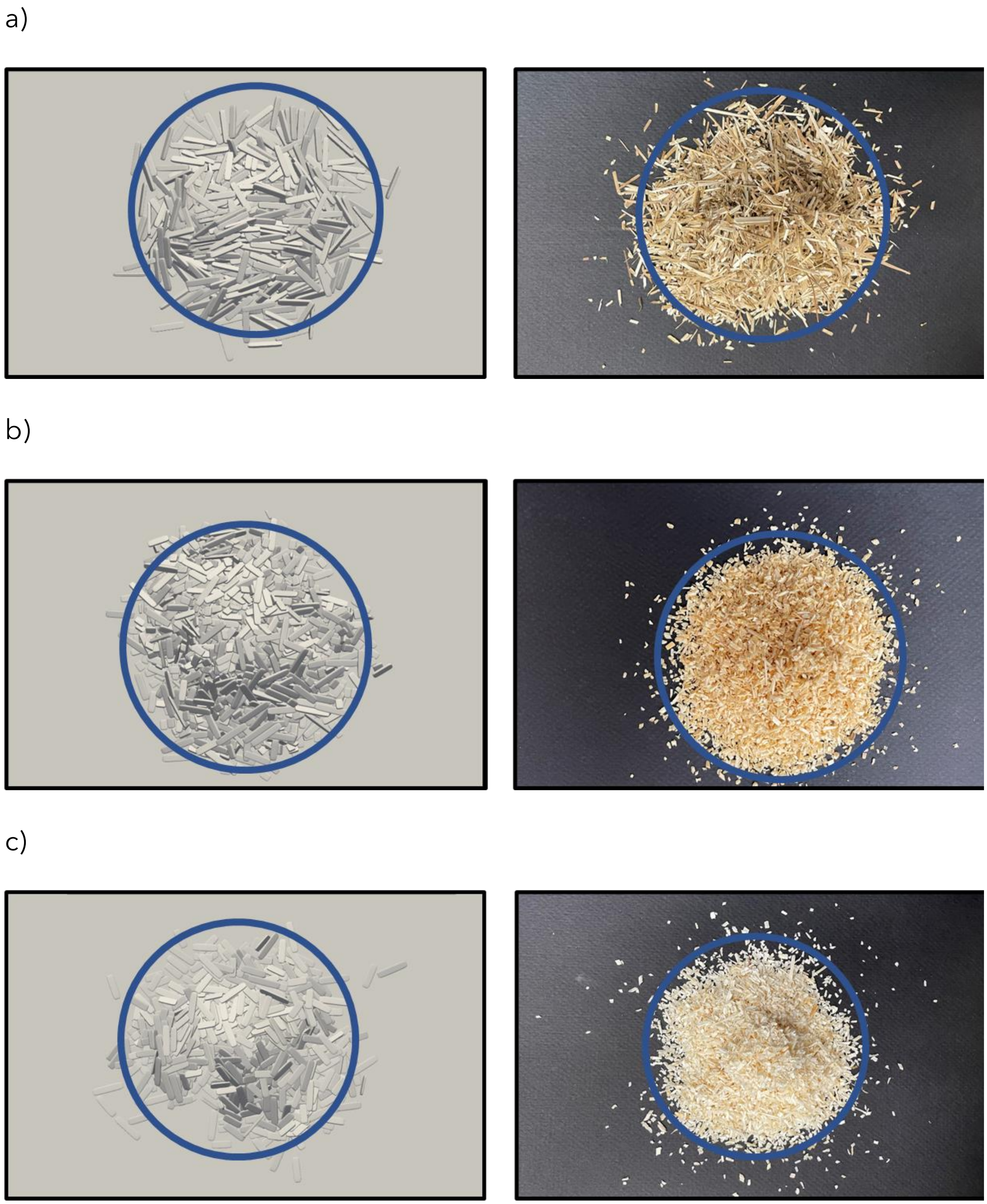

Figure 4.7. Top view of material piles from simulation and experiment after image processing for a) switchgrass, b) loblolly pine, and c) hybrid poplar.

Table 4.3. Computational and experimental outputs from the angle of repose tests for switchgrass, loblolly pine, and hybrid poplar samples.

Material	Switchgrass		Loblolly Pine		Hybrid Poplar	
Parameter	Comp.	Expt.	Comp.	Expt.	Comp.	Expt.
Mean aspect ratio	7.7	7.9	3.0	3.1	3.5	3.4
Fill mass (kg)	0.50	0.53	0.50	0.51	0.50	0.51
Fill height (m)	0.18	0.17	0.25	0.25	0.20	0.19
Bulk density (kg/m^3)	140.80 (±0.51)	138.82 (±1.86)	200.12 (±1.55)	198.12 (±1.21)	155.57 (±1.75)	152.17 (±2.11)
Pile diameter (m)	0.167 (±0.006)	0.185 (±0.011)	0.210 (±0.007)	0.195 (±0.015)	0.185 (±0.009)	0.199 (±0.019)
Angle of repose (°)	41.30 (±0.95)	40.10 (±0.79)	26.10 (±0.51)	27.30 (±1.05)	29.10 (±0.51)	30.50 (±1.29)

We conducted both DEM simulations and physical experiments in triplicate and averaged the results.

For all cases, the fill mass is similar between experiments and simulations. The fill height is highest for the loblolly pine, resulting in the highest bulk density value. The bulk density value is not significantly different from values obtained using the bulk density apparatus as described in Chapter 3, indicating that the simulation's particle packing represents the real biomass particles. We saw a larger degree of variation between the computational and experimental spread of the particle piles. We believe a potential reason for this might be the presence of smaller particles in the samples for the experimental materials that were not completely removed from our desired particle-sieving process. Finally, the angle of repose values is not significantly different from our experimental measurements. The similarity between experimental and computational results indicates that the model captures the real particle flow characteristics well.

4.3.3. Computational Model Output: Contact Forces

We used the validated model for investigating micro-scale forces. Prior research on granular material flow found a correlation between particle aspect ratio (AR) and the total contact force between the particles [41-43]. Therefore, we conducted an investigation of the relationship between the total particle contact force and aspect ratios for our loblolly pine (AR = 3), hybrid poplar (AR = 4), and switchgrass (AR = 8) particles.

Figure 4.8 shows the change in magnitude of the total particle contact force with a change in aspect ratios for the different assemblies. With an increased particle aspect ratio, the contact forces between the particles initially sharply decrease and become almost constant. This is comparable with the results of prior research with particles with different aspect ratios, with the normal force becoming constant after a certain aspect ratio [44-46].

We theorize that at higher aspect ratios, i.e., higher degree of elongation of particles, the number of contact points between them is also high. However, the overall load stays the same. Thus, the particle assembly's average contact force (contact force/load) decreases until the preferential orientation is fully achieved. This constant contact force indicates the fact that the structuring of the particles within the flow reaches a stable layered state and becomes independent of the elongation of particles [44].

4.4. Conclusions

In this study, we combined a dynamic particle analysis method with a custom image feature extraction process and determined important morphological parameters for herbaceous, softwood, and hardwood materials.

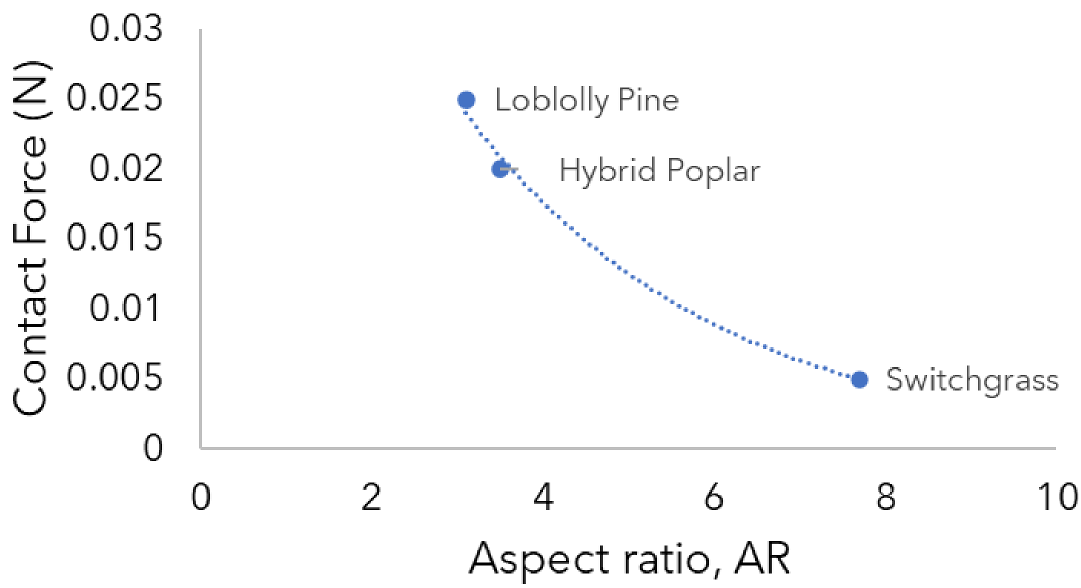

Figure 4.8. The magnitude of total contact force within particle assemblies of different aspect ratios.

Then we developed a DEM model to study their flow behavior during a hollow cylinder angle of repose test. The developed model can realistically capture biomass particles' shapes and macro-scale flow using a superquadric particle assumption. Next, we quantitatively validated the model by comparing the bulk density, angle of repose, and pile diameter from the simulation with physical tests performed using geometrically identical experimental setups. Finally, we examined the distribution of forces for the particles, providing a unique insight into the flow mechanism for the biomass particle assemblies of different aspect ratios. The overall contact force decreases with an increased aspect ratio (i.e., more elongated superquadric particles) until the contact force achieves a state beyond which the uniformity in force distribution becomes nearly constant and independent of the aspect ratio.

Overall, our particle morphology analysis, coupled with the computational model, can be used to predict the flow behavior of different biomass materials without running expensive physical tests.

References

(1) Zhong, W.; Yu, A.; Liu, X.; Tong, Z.; Zhang, H. DEM/CFD-DEM modelling of non-spherical particulate systems: theoretical developments and applications. *Powder Technol.* **2016**, *302*, 108-152.

(2) Ketterhagen, W. R.; am Ende, M. T.; Hancock, B. C. Process modeling in the pharmaceutical industry using the discrete element method. *J. Pharm. Sci.* **2009**, *98* (2), 442-470.

(3) Oyedeji, O.; Gitman, P.; Qu, J.; Webb, E. Understanding the Impact of Lignocellulosic Biomass Variability on the Size Reduction Process: A Review. *ACS Sustain. Chem. Eng.* **2020**, *8* (6), 2327-2343. DOI: https://doi.org/10.1021/acssuschemeng.9b06698.

(4) Ferellec, J.-F.; McDowell, G. R. A method to model realistic particle shape and inertia in DEM. *Granul. Matter* **2010**, *12* (5), 459-467.

(5) Shen, Z.; Jiang, M.; Thornton, C. DEM simulation of bonded granular material. Part I: contact model and application to cemented sand. *Comput Geotech* **2016**, *75*, 192-209.

(6) Lin, X.; Ng, T. T. Contact detection algorithms for three-dimensional ellipsoids in discrete element modelling. *Int. J. Numer. Anal. Methods Geomech.* **1995**, *19* (9), 653-659.

(7) Markauskas, D.; Kačianauskas, R.; Džiugys, A.; Navakas, R. Investigation of adequacy of multi-sphere approximation of elliptical particles for DEM simulations. *Granul. Matter* **2010**, *12* (1), 107-123.

(8) Mindlin, R. D. Elastic spheres in contact under varying oblique forces. *J Appl Mech* **1953**, *20*, 327-344.

(9) Burns, S. J.; Piiroinen, P. T.; Hanley, K. J. Critical time step for DEM simulations of dynamic systems using a Hertzian contact model. *Int. J. Numer. Methods Eng.* **2019**, *119* (5), 432-451.

(10) Plassiard, J.-P.; Belheine, N.; Donzé, F.-V. A spherical discrete element model: calibration procedure and incremental response. *Granul. Matter* **2009**, *11* (5), 293.

(11) Abbaspour-Fard, M. H. Theoretical validation of a multi-sphere, discrete element model suitable for biomaterials handling simulation. *Biosys. Eng.* **2004**, *88* (2), 153-161.

(12) Kruggel-Emden, H.; Rickelt, S.; Wirtz, S.; Scherer, V. A study on the validity of the multi-sphere Discrete Element Method. *Powder Technol.* **2008**, *188* (2), 153-165.

(13) Cleary, P. W. DEM prediction of industrial and geophysical particle flows. *Particuology* **2010**, *8* (2), 106-118.

(14) Jiang, Z.; Du, J.; Rieck, C.; Bück, A.; Tsotsas, E. PTV experiments and DEM simulations of the coefficient of restitution for irregular particles impacting on horizontal substrates. *Powder Technol.* **2020**, *360*, 352-365.
(15) Guo, Y.; Wassgren, C.; Curtis, J. S.; Xu, D. A bonded sphero-cylinder model for the discrete element simulation of elasto-plastic fibers. *Chem. Eng. Sci.* **2018**, *175*, 118-129.
(16) Fraige, F. Y.; Langston, P. A.; Chen, G. Z. Distinct element modelling of cubic particle packing and flow. *Powder Technol.* **2008**, *186* (3), 224-240.
(17) Alonso-Marroquin, F. Spheropolygons: A new method to simulate conservative and dissipative interactions between 2D complex-shaped rigid bodies. *Europhys. Lett.* **2008**, *83* (1), 14001.
(18) Liu, Z.; Zhao, Y. Multi-super-ellipsoid model for non-spherical particles in DEM simulation. *Powder Technol.* **2020**, *361*, 190-202.
(19) Xia, Y.; Stickel, J. J.; Jin, W.; Klinger, J. A review of computational models for the flow of milled biomass I: Discrete-particle models. *ACS Sustain. Chem. Eng.* **2020**, *8* (16), 6142–6156. DOI: https://doi.org/10.1021/acssuschemeng.0c00402.
(20) Chen, W.; Donohue, T.; Katterfeld, A.; Williams, K. Comparative discrete element modelling of a vibratory sieving process with spherical and rounded polyhedron particles. *Granul. Matter* **2017**, *19* (4), 1-12.
(21) Barr, A. H. Superquadrics and angle-preserving transformations. *IEEE Comput. Graph. Appl.* **1981**, *1* (1), 11-23.
(22) Lopes, D. S.; Silva, M. T.; Ambrósio, J. A.; Flores, P. A mathematical framework for rigid contact detection between quadric and superquadric surfaces. *Multibody Syst. Dyn.* **2010**, *24* (3), 255-280.
(23) Williams, J. R.; Pentland, A. P. Superquadrics and modal dynamics for discrete elements in interactive design. *Eng. Comput.* **1992**, *9*, 115-127. DOI: https://doi.org/10.1108/eb023852.
(24) Soltanbeigi, B.; Podlozhnyuk, A.; Papanicolopulos, S.-A.; Kloss, C.; Pirker, S.; Ooi, J. Y. DEM study of mechanical characteristics of multi-spherical and superquadric particles at micro and macro scales. *Powder Technol.* **2018**, *329*, 288-303.
(25) Soltanbeigi, B.; Podlozhnyuk, A.; Ooi, J. Y.; Kloss, C.; Papanicolopulos, S.-A. Comparison of multi-sphere and superquadric particle representation for modelling shearing and flow characteristics of granular assemblies. In *EPJ Web of Conferences*, 2017, 2017; EDP Sciences: Vol. 140, p 06015.
(26) Song, Y.; Turton, R.; Kayihan, F. Contact detection algorithms for DEM simulations of tablet-shaped particles. *Powder Technol.* **2006**, *161* (1), 32-40.

(27) Lu, G.; Third, J. R.; Müller, C. R. Critical assessment of two approaches for evaluating contacts between super-quadric shaped particles in DEM simulations. *Chem. Eng. Sci.* **2012**, *78*, 226-235.
(28) Podlozhnyuk, A.; Pirker, S.; Kloss, C. Efficient implementation of superquadric particles in Discrete Element Method within an open-source framework. *Comput. Part. Mech.* **2017**, *4* (1), 101-118.
(29) Peng, D.; Hanley, K. J. Contact detection between convex polyhedra and superquadrics in discrete element codes. *Powder Technol.* **2019**, *356*, 11-20.
(30) Wang, S.; Marmysh, D.; Ji, S. Construction of irregular particles with superquadric equation in DEM. *Theor. Appl. Mech. Lett.* **2020**, *10* (2), 68-73.
(31) Lyu, F.; Thomas, M.; Hendriks, W. H.; Van der Poel, A. F. B. Size reduction in feed technology and methods for determining, expressing and predicting particle size: A review. *Anim. Feed Sci. Technol.* **2020**, *261*, 114347.
(32) Tannous, K.; Lam, P.; Sokhansanj, S.; Grace, J. Physical properties for flow characterization of ground biomass from douglas fir wood. *Part. Sci. Technol.* **2013**, *31* (3), 291-300.
(33) Guo, Q.; Chen, X.; Liu, H. J. F. Experimental research on shape and size distribution of biomass particle. *Fuel* **2012**, *94*, 551-555.
(34) Igathinathane, C.; Melin, S.; Sokhansanj, S.; Bi, X.; Lim, C.; Pordesimo, L.; Columbus, E. Machine vision based particle size and size distribution determination of airborne dust particles of wood and bark pellets. *Powder Technol.* **2009**, *196* (2), 202-212.
(35) Fu, J.; Cheong, Y.; Reynolds, G.; Adams, M.; Salman, A.; Hounslow, M. An experimental study of the variability in the properties and quality of wet granules. *Powder Technol.* **2004**, *140* (3), 209-216.
(36) Oliver, M.; Matúš, Č.; Ľudmila, G.; Martin, J.; Radovan, R.; Peter, P. Dynamic Image Analysis to Determine Granule Size and Shape, for Selected High Shear Granulation Process Parameters. *Stroj. Cas.* **2019**, *69* (4), 57-64.
(37) Xu, R.; Di Guida, O. A. Comparison of sizing small particles using different technologies. *Powder Technol.* **2003**, *132* (2-3), 145-153.
(38) Aela, P.; Wang, J.; Yousefian, K.; Fu, H.; Yin, Z.-Y.; Jing, G. Prediction of crushed numbers and sizes of ballast particles after breakage using machine learning techniques. *Constr. Build. Mater.* **2022**, *337*, 127469.
(39) Hoang, U. T.; Nguyen, N. H. T. Particle shape effects on granular column collapse using superquadric DEM. *Powder Technol.* **2023**, *424*, 118559.

(40) Zhao, S.; Evans, T. M.; Zhou, X. Effects of curvature-related DEM contact model on the macro-and micro-mechanical behaviours of granular soils. *Géotechnique* **2018**, *68* (12), 1085-1098.
(41) Tangri, H.; Guo, Y.; Curtis, J. S. Hopper discharge of elongated particles of varying aspect ratio: Experiments and DEM simulations. *Chem. Eng. Sci.: X* **2019**, *4*, 100040.
(42) Deng, X. L.; Davé, R. N. Dynamic simulation of particle packing influenced by size, aspect ratio and surface energy. *Granul. Matter* **2013**, *15*, 401-415.
(43) Gan, J.; Yu, A. DEM simulation of the packing of cylindrical particles. *Granul. Matter* **2020**, *22*, 1-19.
(44) Hossain, M.; Zhu, H. P.; Yu, A. B. Numerical investigation on effect of particle aspect ratio on the dynamical behaviour of ellipsoidal particle flow. *J. Phys.: Condens. Matter* **2021**, *33* (45), 455102.
(45) Yang, J.; Buettner, K. E.; DiNenna, V. L.; Curtis, J. S. Computational and experimental study of the combined effects of particle aspect ratio and effective diameter on flow behavior. *Chem. Eng. Sci.* **2022**, *255*, 117621.
(46) Kildashti, K.; Dong, K.; Samali, B.; Zheng, Q.; Yu, A. Evaluation of contact force models for discrete modelling of ellipsoidal particles. *Chem. Eng. Sci.* **2018**, *177*, 1-17.

CHAPTER 5.

RELATIVE INFLUENCE OF LIGNOCELLULOSIC BIOMASS PROPERTIES ON THE FLOW BEHAVIOR OF BIOMASS PARTICULATES

Disclaimer: This chapter is a draft version of the following article:

Ehite, E. H.; Abdoulmoumine, N. Analysis of Relative influence of Lignocellulosic Biomass Properties on the Flow Behavior Using Classical and Modern Statistical Techniques. In preparation for submission to *Journal of Computational and Applied Mathematics.*

5.1. Introduction

This chapter details the investigation of the relative influence of the morphological, material, and mechanical properties of lignocellulosic biomass assemblies on the macro-scale flow behavior.

The morphological, material, and mechanical properties of lignocellulosic biomass materials significantly affect their flow behavior. However, it is computationally impractical to capture the contribution of every single biomass property when modeling the flow behavior of lignocellulosic biomass particle assemblies. Instead, it is more practical to identify the properties with the most influence and focus our attention on them. In the previous chapter, we developed a high-fidelity discrete element computational model that captures real biomass morphology and flow processes. However, the output from computational modeling techniques, such as the discrete element method (DEM), of solid particulate systems is highly dependent on the appropriate values of the model input parameters representing the morphological, material, and mechanical properties of the particle assembly [1]. While we can validate DEM by accounting for numerical accuracy and comparative analysis with experimental results, it is only conditionally valid for that specific set of input parameters. Therefore, DEM researchers follow the development of baseline models by conducting parametric studies that vary the input parameters' values [2-4]. The parametric study allows the examination of the effect of individual input parameters on the model outputs and establishes the robustness of the model for a wide range of particle properties [5]. Additionally, it allows the development and selection of simpler models that include only the most influential parameters. The principle of Occam's Razor suggests that simpler models are preferred to more complex ones for a given level of accuracy and can be more easily validated using experimental outcomes [6].

A common approach to parametric study involves conducting a design of experiments (DOE)-based sensitivity analysis to analyze the relative effect of the input parameters on model responses and the cross-relation between the input parameters [7-9]. The DOE approach initially involves establishing a "full" statistical model with all the possible factors influencing the output. Our model consists of a response variable y_i and multiple explanatory variables x_i, and for a general case of k variables can be described by Equation 5.1.

$$y_i = \beta_o + \beta_1 x_{i1} + \beta_1 x_{i2} + \cdots + \beta_k x_{ik} + \varepsilon_i\,, \qquad for\ i = 1,2,\ldots,n \qquad (5.1)$$

Then, instead of performing experiments for all combinations of factors, which can be expensive and time-consuming, a selected, systematic set of experiments is conducted for specific values of the selected factors. Afterward, the best approximating model is chosen among competing models by suitable model evaluation criteria for the given data set [10, 11]. DEM researchers have successfully implemented the sensitivity analysis-based approach for evaluating particle velocity trajectories in a convective mixing system [12], powder flowability in rheometers [9], and particle aggregations for single-particle crushing tests of railway ballast stones [13].

The choice of the statistical model evaluation and selection technique is a great area of interest in the statistical literature [14]. Classical model selection involves the use of the least square estimates method, which consists of determining the linear regression parameters, such as the regression coefficients and standard error, and then testing for significance using analysis of variance (ANOVA) and t-statistic, with a target of finding the minimum p values [15, 16]. However, the modern field of statistical data modeling prefers using "information-theoretic" criteria for identifying an optimal and parsimonious model in data analysis from a class of competing models, considering the model complexity [14]. This approach is also known as "quantile modeling." These kinds of model selection criteria act as figures of merits, or performance measures for competing models [17, 18]. A model with more parsimony, i.e., a lower number of parameters or variables, rather than a complex, i.e., a high dimensional model, is preferable as it minimizes the cost of measuring the models required to implement the model [15, 19].

Information-theoretic model selection criteria include Akaike's Information Criterion (AIC) [20], Takeuchi's Information Criterion (TIC) [21], Schwarz Bayesian Information Criterion (BIC, also known as SBC) [22], as well as Bozdogan's Consistent AIC (CAIC) and Consistent AIC with Fisher Information (CAICF) [14]. Bozdogan and Ueno [23] extended the CAICF criterion further, developing a dimension-consistent criterion called ICOMP. Most of the above information criteria select a model by maximizing the log-likelihood of a model and penalizing it by some scalar value [24]. AIC penalizes a model based on the number of parameters in a model. In contrast, BIC, CAIC, CAICF, and ICOMP all penalize a model as a function of both the sample size and the number of parameters in the model. These penalty functions aim to penalize more complex and overparameterized models [25].

Therefore, we can use a DOE-based approach in combination with classical and modern model selection techniques to determine the influence of the biomass properties (the predictor variables) on the flow parameters (response variables) and develop simpler models that can be validated more easily with experimental results.

In this study, we take the computational model for the hollow cylinder angle of repose test in Chapter 4 and conduct a sensitivity analysis of the biomass assembly's properties to analyze their relative influence on the macroscale flow behavior. The research question in this objective is: How to determine the relative influence of biomass properties on flow behavior and develop statistically efficient models to capture their relationship?

We hypothesize that we can take a design of experiments (DoE) approach, reduce the number of experiments required for the statistical analysis, and then use classical and modern model selection criteria to develop simpler models to represent the relation between the flow behavior and biomass properties. We will test our hypothesis by i) Developing a 2-level, 5-factor, half-fractional experimental design for the angle of repose DEM model, ii) Constructing a linear regression model to describe the relationship between the response variable, namely the angle of repose and the most significant predictor variables, and iii) Optimize the validated regression model to determine the minimum value of the angle of repose.

5.2. Materials and Methods

5.2.1. Design of Simulations (DoS)

We employed a design of experiments (DoE) method to analyze the interaction between the DEM parameters and the parametric effect on the simulation outputs. This approach ensures maximum orthogonal variance, encompasses the entire experimental space, and reduces the number of required experiments [26]. Additionally, unlike the traditional one-at-a-time approach (variance of one parameter at a time while keeping the others constant), we can produce a large dataset for multivariate analysis [27]. Since, in our case, the experiments involve conducting DEM simulations, we refer to this approach more accurately as the "design of simulations" (DoS) [28, 29]. We used the DoS approach to create a matrix of simulations and determined the number of simulations required using Equation 5.2.

$$L^{x-n}, \tag{5.2}$$

where L = Number of levels (typically 2), x = Number of variables, n = optional fractional reduction.

Our simulation plan involves using a fractional factorial design (2^{x-n}, reduced experimental space with a lower number of tests), namely a half-factorial design [30, 31].

5.2.2. Input Parameters in the Design of Simulations (DoS)

In this study, we selected the five particle-particle properties as variable input parameters for the design of simulations, namely Young's modulus (Y_p), Poisson's ratio (ν_p), coefficient of restitution (ε_{pp}), coefficient of sliding friction ($\mu_{s,pp}$), and coefficient of rolling friction ($\mu_{r,pp}$).

We considered the experimentally measured values as their base values and then changed them by an amount of ±15% to calculate a low (-1) and a high value (+1). Therefore, we have two levels of values for each input parameter, and thus it is a two-level, five-factor design. Since in our DEM model, the particle-wall interaction properties are an average of the particle properties and the value of the wall material properties from literature; their values will also assume three levels in response to the change in particle properties. We used the wall properties based on literature and kept them constant to reduce the required number of iterations.

With our 5 factors to run a full factorial set of experiments, we would need $2^5 = 32$ experiments. We selected a half-fraction design to reduce time and computational cost, reducing the number of simulations to 16 [26, 32]. We added 2 replicate tests with all the parameters having the average value. Therefore, the total number of simulations is 18. We constructed the design matrices and the related analyses using the statistical toolbox in MATLAB.

Table 5.1 shows the low (-1), high (+1), and base (0) values used for the variable input parameters, and Table 5.2 shows the values used for the constant input parameters for the DEM simulations.

5.2.3. Statistical Analysis

After running the simulation experiments in the LIGGGHTS DEM environment for the half-factorial design, we determine the angle of repose (AOR) values using the steps outlined in Chapter 3. Then, we conducted a multiple linear regression on the dataset using the "glmfit" function in MATLAB.

Afterward, we determine the linear regression statistics, including R-square and adjusted R-square values. If the R square values are high (≥0.90), we consider that our full linear regression model fits the data well. Next, we construct a reduced regression model using the most significant factors and their interactions (p-value < 0.05). Then, we conduct a process optimization (using the "fitrauto" function in MATLAB) to find the optimal value of the model response, i.e., the angle of repose. As we have established in Chapters 2 and 3, a material with a lower angle of repose has a lower potential energy [33]. Therefore, it provides the lowest resistance to flow and highest flowability when motion is induced. Therefore, the value of the angle of repose is optimum for flow when it is minimum.

Table 5.1. DEM input parameters varied in the DoS.

Parameter	Symbols	Low (-1)	Base (0)	High (+1)
Young's modulus, particle [MPa]	YM	0.85	1	1.15
Poisson's ratio, particle [-]	PR	0.26	0.30	0.35
Coefficient of sliding friction, particle-particle [-]	sf	0.31	0.36	0.41
Coefficient of rolling friction particle-particle [-]	rf	0.68	0.80	0.92
Coefficient of restitution, particle-particle [-]	CoR	0.51	0.60	0.69
Coefficient of sliding friction, particle-wall [-]	sf_{pw}	0.33	0.36	0.39
Coefficient of rolling friction, particle-wall [-]	rf_{pw}	0.49	0.55	0.61
Coefficient of restitution, particle-wall [-]	CoR_{pw}	0.56	0.60	0.65

Table 5.2. DEM input parameters considered constant in the DoS.

Parameter	Symbols	Values
Young's modulus, wall [MPa] [a]	YM_w	1
Poisson's ratio, wall [-] [a]	PR_w	0.25
Coefficient of sliding friction, wall [-] [a]	sf_w	0.30
Coefficient of rolling friction, wall [-] [b]	rf_w	0.30
Coefficient of restitution, wall [-] [a]	CoR_w	0.65

Finally, we conducted a residuals analysis to ensure the normality assumption of our reduced model.

In addition to the classical statistical parameters, we improved the robustness of our data analysis process by conducting quantile modeling for the angle of repose data. We scored several information criteria, namely Akaike's Information Criterion (AIC) [20], Bozdogan's Consistent AIC (CAIC) [14], Schwarz Bayesian criterion (SBC) [22], and Bozdogan's information complexity criterion (ICOMP) [23], which are described by Equation 5.3.

$$
\begin{gathered}
AIC = -2logL(\hat{\theta}) + 2k, \\
CAIC = -2logL(\hat{\theta}) + k[log(n) + 1] \\
SBC = -2logL(\hat{\theta}) + k[log(n), \\
ICOMP(IFIM) = -2logL(\hat{\theta}) + 2C_{1F}\left(\hat{F}^{-1}(\hat{\theta})\right), \\
where\ IFIM\ is\ the\ inverse\ Fisher\ information\ matrix, and \\
C_{1F}\left(\hat{F}^{-1}(\hat{\theta})\right) = \frac{1}{4\overline{\bar{\lambda}_a}^2}\sum_{j=1}^{s}\left(\lambda - \bar{\lambda}_a\right)^2, \\
where, \bar{\lambda}_a\ is\ the\ arithmetic\ mean\ of\ the\ eigen\ values\ \lambda_j\ ,
\end{gathered}
\tag{5.3}
$$

We used the information criteria to determine the best-fitting distribution for the dataset for each material under the test. The best-fitting distribution provides the lowest score for each information criterion. Then, we generate a Q-Q plot to check the suitability of the selected distribution in a graphical manner. We conducted quantile modeling using the statistical toolbox in MATLAB (The MathWorks, Natick, MA, USA).

5.3. Results

5.3.1. Half-Factorial Design

Table 5.3 shows the input parameters ($YM, PR, sf, rf, CoR, and\ AoR$) and response parameters for our half-factorial design for the switchgrass, loblolly pine, and hybrid poplar particles. In addition to the 16 simulations, we added 2 additional experiments with the values called central points (represented by all zeros), corresponding to the average value of the high and low levels in each factor.

5.3.2. Multiple Linear Regression

Table 5.4 shows the regression statistics from the multiple linear regression.

We see that the R-square and adjusted R-square values are > 0.90, validating our mathematical model, i.e., the input parameters we chose to have some degree of correlation with the response variable (AOR). From the Probability column (p), we selected the factors and interactions with p-value<0.05 to be the most significant. While factors PR and rf have a p-value>0.05, their interaction p-value is 0.02; therefore, we must keep them.

Table 5.3. Inputs and outputs of the angle of repose simulation studies for switchgrass (SG), loblolly pine (PI), and hybrid poplar (POP) particles.

Run	Young's modulus, YM (MPa)	Poisson's ratio, PR	Coeff. of sliding friction, sf	Coeff. of rolling friction, rf	Coeff. of restitution, CoR	Angle of repose, (º)		
						SG	PI	POP
1	0.85	0.26	0.31	0.68	0.69	29.00	17.85	14.33
2	1.15	0.26	0.31	0.68	0.51	29.19	21.77	18.41
3	0.85	0.35	0.31	0.68	0.51	26.60	27.28	21.13
4	1.15	0.35	0.31	0.68	0.69	34.18	28.77	27.99
5	0.85	0.26	0.41	0.68	0.51	36.65	26.01	20.72
6	1.15	0.26	0.41	0.68	0.69	34.96	32.06	21.09
7	0.85	0.35	0.41	0.68	0.69	41.70	17.79	17.52
8	1.15	0.35	0.41	0.68	0.51	39.77	25.04	21.69
9	0.85	0.26	0.31	0.92	0.51	24.75	18.44	15.93
10	1.15	0.26	0.31	0.92	0.69	42.10	24.28	23.32
11	0.85	0.35	0.31	0.92	0.69	23.36	23.14	14.76
12	1.15	0.35	0.31	0.92	0.51	33.21	20.70	15.44
13	0.85	0.26	0.41	0.92	0.69	14.54	28.88	19.58
14	1.15	0.26	0.41	0.92	0.51	28.71	18.39	17.11
15	0.85	0.35	0.41	0.92	0.51	35.01	21.59	20.87
16	1.15	0.35	0.41	0.92	0.69	45.46	19.15	17.67
17	1.00	0.31	0.36	0.80	0.60	22.85	18.05	14.81
18	1.00	0.31	0.36	0.80	0.60	19.57	20.07	17.37

Table 5.4. Multiple linear regression statistics for switchgrass particles.

Regression Statistics	
Multiple R	0.99
R Square	0.98
Adjusted R Square	0.80
Standard Error	3.31
Observations	18

ANOVA

	df	*SS*	*MS*	*F*	*Significance F*
Regression	15	968.97	64.60	0.56	0.80
Residual	2	230.02	115.01		
Total	17	1198.99			

	Coefficients	*Standard Error*	*t Stat*	*P-value*	*Lower 95%*	*Upper 95%*
Intercept	31.20	2.53	12.34	**0.01**	20.33	42.08
YM	3.50	2.68	1.30	**0.02**	-8.04	15.03
PR	2.46	2.68	0.92	0.46	-9.07	14.00
sf	2.15	2.68	0.80	0.51	-9.38	13.69
rf	-1.56	2.68	-0.58	0.62	-13.09	9.98
CoR	0.71	2.68	0.27	0.82	-10.82	12.25
*YM*PR*	-0.26	2.68	-0.10	0.93	-11.79	11.28
*YM*sf*	-0.87	2.68	-0.33	0.78	-12.41	10.66
*YM*rf*	2.98	2.68	1.11	0.38	-8.56	14.52
*YM*CoR*	2.52	2.68	0.94	0.45	-9.02	14.05
*PR*sf*	3.42	2.68	1.28	0.33	-8.11	14.96
*PR*rf*	0.91	2.68	0.34	**0.04**	-10.63	12.44
*PR*CoR*	0.55	2.68	0.21	0.86	-10.98	12.09
*sf*rf*	-2.11	2.68	-0.79	0.51	-13.65	9.42
*sf*CoR*	-1.15	2.68	-0.43	0.71	-12.68	10.39
*rf*CoR*	-0.24	2.68	-0.09	0.94	-11.78	11.30

Hence, we find a reduced formula for estimating the angle of repose of switchgrass as a function of three factors out of the original five we thought relevant.

Equation 5.4 shows the reduced estimation model for switchgrass.

$$AoR_{SG} = 31.20 + 3.50\,YM + 2.46\,PR - 1.56\,rf + 0.91\,(PR * rf)\,, \qquad (5.4)$$

We conducted similar multiple linear regression modeling for loblolly pine and hybrid poplar samples, and Table 5.5 and Table 5.6 shows their regression statistics. The reduced models for loblolly pine and hybrid poplar also contained $YM, PR, and\ rf$ as the most significant parameters. The reduced models for loblolly pine and hybrid poplar are given by Equations 5.5 and 5.6.

$$AoR_{PI} = 22.74 + 0.58\,YM - 0.26\,PR - 1.38\,rf - 0.24\,(PR * rf)\,, \qquad (5.5)$$

$$AoR_{POP} = 18.87 + 1.12\,YM + 0.41\,PR - 1.14\,rf - 1.31\,(PR * rf)\,, \qquad (5.6)$$

5.3.3. Process Optimization

We took the reduced linear regression model for each material and conducted an optimization process in MATLAB to find the minimum value for the angle of repose (which provides the maximum flowability within out experimental space). Figure 5.1 shows the heat map for the reduced model for switchgrass. The greener portion represents the lower value of the angle of repose. We can identify the minimum angle value of repose to be 22.78^0, corresponding to $rf = 1$ and $PR = -1$.

Table 5.5. Multiple linear regression statistics for loblolly pine particles.

Regression Statistics	
Multiple R	0.95
R Square	0.90
Adjusted R Square	0.88
Standard Error	4.03
Observations	18

ANOVA

	df	*SS*	*MS*	*F*	*Significance F*
Regression	15	301.93	20.13	1.24	0.53
Residual	2	32.41	16.21		
Total	17	334.34			

	Coefficients	*Standard Error*	*t Stat*	*P-value*	*Lower 95%*	*Upper 95%*
Intercept	22.74	0.95	23.96	**0.00**	18.65	26.82
YM	0.58	1.01	0.57	**0.03**	-3.76	4.91
PR	-0.26	1.01	-0.26	0.82	-4.59	4.07
sf	0.42	1.01	0.41	0.72	-3.91	4.75
rf	-1.38	1.01	-1.37	**0.01**	-5.71	2.95
CoR	0.79	1.01	0.79	0.51	-3.54	5.12
*YM*PR*	-0.09	1.01	-0.09	0.94	-4.42	4.24
*YM*sf*	-0.53	1.01	-0.52	0.65	-4.86	3.80
*YM*rf*	-1.76	1.01	-1.75	0.22	-6.09	2.57
*YM*CoR*	1.50	1.01	1.49	0.27	-2.83	5.83
*PR*sf*	-2.46	1.01	-2.44	0.13	-6.79	1.87
*PR*rf*	-0.24	1.01	-0.41	**0.04**	-4.74	3.92
*PR*CoR*	-1.51	1.01	-1.50	0.27	-5.84	2.82
*sf*rf*	-0.41	1.01	-0.24	0.72	-4.57	4.09
*sf*CoR*	0.06	1.01	0.06	0.96	-4.27	4.39
*rf*CoR*	1.25	1.01	1.24	0.34	-3.08	5.58

Table 5.6. Multiple linear regression statistics for hybrid poplar particles.

Regression Statistics	
Multiple R	0.95
R Square	0.90
Adjusted R Square	0.87
Standard Error	3.22
Observations	18

ANOVA

	df	*SS*	*MS*	*F*	*Significance F*
Regression	15	191.43	12.76	1.23	0.54
Residual	2	20.73	10.37		
Total	17	212.16			

	Coefficients	*Standard Error*	*t Stat*	*P-value*	*Lower 95%*	*Upper 95%*
Intercept	18.87	0.76	24.87	**0.00**	15.61	22.14
YM	1.12	0.80	1.39	**0.03**	-2.35	4.58
PR	0.41	0.80	0.51	0.06	-3.05	3.87
sf	0.31	0.80	0.38	0.14	-3.16	3.77
rf	-1.14	0.80	-1.41	0.29	-4.60	2.33
CoR	0.31	0.80	0.38	0.74	-3.15	3.77
*YM*PR*	-0.05	0.80	-0.07	0.95	-3.52	3.41
*YM*sf*	-1.26	0.80	-1.56	0.26	-4.72	2.20
*YM*rf*	-0.82	0.80	-1.02	0.42	-4.28	2.64
*YM*CoR*	1.87	0.80	2.32	0.15	-1.60	5.33
*PR*sf*	-0.51	0.80	-0.63	0.59	-3.97	2.96
*PR*rf*	-1.31	0.80	-1.63	**0.03**	-4.77	2.15
*PR*CoR*	-0.46	0.80	-0.57	0.63	-3.92	3.01
*sf*rf*	0.41	0.80	0.51	0.24	-3.05	3.88
*sf*CoR*	-0.88	0.80	-1.09	0.39	-4.34	2.59
*rf*CoR*	0.44	0.80	0.54	0.64	-3.03	3.90

YM -1

	rf																				
PR	-1	-0.9	-0.8	-0.7	-0.6	-0.5	-0.4	-0.3	-0.2	-0.1	0	0.1	0.2	0.3	0.4	0.5	0.6	0.7	0.8	0.9	1
1	31	31	30.9	30.8	30.8	30.7	30.6	30.6	30.5	30.4	30	30	30	30	30	30	30	30	30	30	30
0.9	31	30.8	30.7	30.6	30.6	30.5	30.4	30.3	30.3	30.2	30	30	30	30	30	30	30	30	30	29	29
0.8	31	30.6	30.5	30.4	30.3	30.3	30.2	30.1	30	29.9	30	30	30	30	30	29	29	29	29	29	29
0.7	30	30.4	30.3	30.2	30.1	30	29.9	29.9	29.8	29.7	30	29	29	29	29	29	29	29	29	29	29
0.6	30	30.2	30.1	30	29.9	29.8	29.7	29.6	29.5	29.4	29	29	29	29	29	29	29	29	28	28	28
0.5	30	30	29.9	29.8	29.7	29.6	29.5	29.4	29.3	29.2	29	29	29	29	29	28	28	28	28	28	28
0.4	30	29.8	29.7	29.6	29.5	29.4	29.3	29.1	29	28.9	29	29	29	28	28	28	28	28	28	28	28
0.3	30	29.7	29.5	29.4	29.3	29.1	29	28.9	28.8	28.6	29	28	28	28	28	28	28	28	27	27	27
0.2	30	29.5	29.3	29.2	29.1	28.9	28.8	28.6	28.5	28.4	28	28	28	28	28	28	27	27	27	27	27
0.1	29	29.3	29.1	29	28.8	28.7	28.6	28.4	28.3	28.1	28	28	28	28	27	27	27	27	27	27	26
0	29	29.1	28.9	28.8	28.6	28.5	28.3	28.2	28	27.9	28	28	27	27	27	27	27	27	26	26	26
-0.1	29	28.9	28.8	28.6	28.4	28.3	28.1	27.9	27.8	27.6	27	27	27	27	27	27	26	26	26	26	26
-0.2	29	28.7	28.6	28.4	28.2	28	27.9	27.7	27.5	27.3	27	27	27	27	26	26	26	26	26	26	25
-0.3	29	28.5	28.4	28.2	28	27.8	27.6	27.4	27.3	27.1	27	27	27	26	26	26	26	26	25	25	25
-0.4	29	28.4	28.2	28	27.8	27.6	27.4	27.2	27	26.8	27	26	26	26	26	26	25	25	25	25	25
-0.5	28	28.2	28	27.8	27.6	27.4	27.2	27	26.8	26.6	26	26	26	26	26	25	25	25	25	25	24
-0.6	28	28	27.8	27.6	27.4	27.1	26.9	26.7	26.5	26.3	26	26	26	25	25	25	25	25	24	24	24
-0.7	28	27.8	27.6	27.4	27.1	26.9	26.7	26.5	26.3	26	26	26	25	25	25	25	25	24	24	24	24
-0.8	28	27.6	27.4	27.2	26.9	26.7	26.5	26.2	26	25.8	26	25	25	25	25	24	24	24	24	23	23
-0.9	28	27.4	27.2	27	26.7	26.5	26.2	26	25.8	25.5	25	25	25	25	24	24	24	24	23	23	23
-1	27	27.2	27	26.7	26.5	26.3	26	25.8	25.5	25.3	25	25	25	24	24	24	24	23	23	23	23

Figure 5.1. Heat map of the reduced model of the angle of repose simulation study for switchgrass.

We conducted a similar optimization process for loblolly pine and hybrid poplar. Figure 5.2 and Figure 5.3 show the heat map for the reduced model for loblolly pine and hybrid poplar, respectively. We found the minimum angle of repose value for loblolly pine and hybrid poplar to be 20.29^0 (corresponds to $rf = 1$ and $PR = 1$) and 15.72^0 (corresponds to $rf = 1$ and $PR = 1$), respectively.

Figure 5.4 shows the relationship between the factors and the angle of repose in the three-dimensional space. We can see that despite this shape's curvature, each factor's behavior is linear. The shape twists due to the interaction between $PR\, and\, rf$. The minimum angle of repose value of 22.78^0 can be obtained with $YM = 0.85\, MPa$, $PR = 0.26$, and $rf = 0.92$.

Figure 5.5 and Figure 5.6 show a 3D correlation plot for the reduced models of loblolly pine and hybrid poplar, respectively. For both loblolly pine and hybrid poplar, the minimum angle of repose value of 20.29^0 and 15.72^0 can be obtained with $YM = 0.85\, MPa$, $PR = 0.35$, and $rf = 0.92$.

5.3.4. Residuals Analysis for Normality

Figure 5.7 shows the angle of repose values and estimates using the reduced model and residuals vs. estimates plot for switchgrass. We obtained the residuals by subtracting the actual AOR values from the estimates of our

YM -1

PR \ rf	-1	-0.9	-0.8	-0.7	-0.6	-0.5	-0.4	-0.3	-0.2	-0.1	0	0.1	0.2	0.3	0.4	0.5	0.6	0.7	0.8	0.9	1
1	24	23.4	23.2	23	22.9	22.7	22.5	22.4	22.2	22.1	22	22	22	21	21	21	21	21	21	20	20
0.9	24	23.4	23.2	23	22.9	22.7	22.6	22.4	22.2	22.1	22	22	22	21	21	21	21	21	21	20	20
0.8	24	23.4	23.2	23.1	22.9	22.7	22.6	22.4	22.3	22.1	22	22	22	21	21	21	21	21	21	21	20
0.7	24	23.4	23.2	23.1	22.9	22.8	22.6	22.4	22.3	22.1	22	22	22	22	21	21	21	21	21	21	20
0.6	24	23.4	23.2	23.1	22.9	22.8	22.6	22.5	22.3	22.2	22	22	22	22	21	21	21	21	21	21	20
0.5	24	23.4	23.2	23.1	22.9	22.8	22.6	22.5	22.3	22.2	22	22	22	22	21	21	21	21	21	21	21
0.4	24	23.4	23.2	23.1	22.9	22.8	22.6	22.5	22.4	22.2	22	22	22	22	21	21	21	21	21	21	21
0.3	24	23.4	23.2	23.1	23	22.8	22.7	22.5	22.4	22.2	22	22	22	22	22	21	21	21	21	21	21
0.2	24	23.4	23.3	23.1	23	22.8	22.7	22.5	22.4	22.3	22	22	22	22	22	21	21	21	21	21	21
0.1	24	23.4	23.3	23.1	23	22.8	22.7	22.6	22.4	22.3	22	22	22	22	22	21	21	21	21	21	21
0	24	23.4	23.3	23.1	23	22.9	22.7	22.6	22.4	22.3	22	22	22	22	22	21	21	21	21	21	21
-0.1	24	23.4	23.3	23.1	23	22.9	22.7	22.6	22.5	22.3	22	22	22	22	22	22	21	21	21	21	21
-0.2	24	23.4	23.3	23.1	23	22.9	22.7	22.6	22.5	22.3	22	22	22	22	22	22	21	21	21	21	21
-0.3	24	23.4	23.3	23.2	23	22.9	22.8	22.6	22.5	22.4	22	22	22	22	22	22	21	21	21	21	21
-0.4	24	23.4	23.3	23.2	23	22.9	22.8	22.6	22.5	22.4	22	22	22	22	22	22	21	21	21	21	21
-0.5	24	23.4	23.3	23.2	23	22.9	22.8	22.7	22.5	22.4	22	22	22	22	22	22	22	21	21	21	21
-0.6	24	23.4	23.3	23.2	23.1	22.9	22.8	22.7	22.6	22.4	22	22	22	22	22	22	22	21	21	21	21
-0.7	24	23.4	23.3	23.2	23.1	22.9	22.8	22.7	22.6	22.5	22	22	22	22	22	22	22	21	21	21	21
-0.8	24	23.4	23.3	23.2	23.1	23	22.8	22.7	22.6	22.5	22	22	22	22	22	22	22	22	21	21	21
-0.9	24	23.4	23.3	23.2	23.1	23	22.9	22.7	22.6	22.5	22	22	22	22	22	22	22	22	21	21	21
-1	24	23.4	23.3	23.2	23.1	23	22.9	22.8	22.6	22.5	22	22	22	22	22	22	22	22	22	21	21

Figure 5.2. Heat map of the reduced model of the angle of repose simulation study for loblolly pine.

YM -1

		rf																				
		-1	-0.9	-0.8	-0.7	-0.6	-0.5	-0.4	-0.3	-0.2	-0.1	0	0.1	0.2	0.3	0.4	0.5	0.6	0.7	0.8	0.9	1
	1	21	20.4	20.1	19.9	19.6	19.4	19.1	18.9	18.7	18.4	18	18	18	17	17	17	17	16	16	16	16
	0.9	20	20.2	20	19.7	19.5	19.3	19	18.8	18.6	18.4	18	18	18	17	17	17	17	16	16	16	16
	0.8	20	20	19.8	19.6	19.4	19.2	19	18.7	18.5	18.3	18	18	18	17	17	17	17	17	16	16	16
	0.7	20	19.9	19.7	19.5	19.3	19.1	18.9	18.7	18.4	18.2	18	18	18	17	17	17	17	17	16	16	16
	0.6	20	19.7	19.5	19.3	19.2	19	18.8	18.6	18.4	18.2	18	18	18	17	17	17	17	17	16	16	16
	0.5	20	19.6	19.4	19.2	19	18.9	18.7	18.5	18.3	18.1	18	18	18	17	17	17	17	17	17	16	16
	0.4	20	19.4	19.2	19.1	18.9	18.7	18.6	18.4	18.2	18.1	18	18	18	17	17	17	17	17	17	16	16
	0.3	19	19.3	19.1	18.9	18.8	18.6	18.5	18.3	18.2	18	18	18	18	17	17	17	17	17	17	16	16
	0.2	19	19.1	19	18.8	18.7	18.5	18.4	18.3	18.1	18	18	18	18	17	17	17	17	17	17	17	16
PR	0.1	19	18.9	18.8	18.7	18.6	18.4	18.3	18.2	18	17.9	18	18	18	17	17	17	17	17	17	17	17
	0	19	18.8	18.7	18.5	18.4	18.3	18.2	18.1	18	17.9	18	18	18	17	17	17	17	17	17	17	17
	-0.1	19	18.6	18.5	18.4	18.3	18.2	18.1	18	17.9	17.8	18	18	18	17	17	17	17	17	17	17	17
	-0.2	19	18.5	18.4	18.3	18.2	18.1	18	17.9	17.8	17.8	18	18	17	17	17	17	17	17	17	17	17
	-0.3	18	18.3	18.2	18.1	18.1	18	17.9	17.9	17.8	17.7	18	18	17	17	17	17	17	17	17	17	17
	-0.4	18	18.1	18.1	18	18	17.9	17.8	17.8	17.7	17.6	18	18	17	17	17	17	17	17	17	17	17
	-0.5	18	18	17.9	17.9	17.8	17.8	17.7	17.7	17.6	17.6	18	17	17	17	17	17	17	17	17	17	17
	-0.6	18	17.8	17.8	17.8	17.7	17.7	17.6	17.6	17.6	17.5	18	17	17	17	17	17	17	17	17	17	17
	-0.7	18	17.7	17.6	17.6	17.6	17.6	17.6	17.5	17.5	17.5	17	17	17	17	17	17	17	17	17	17	17
	-0.8	18	17.5	17.5	17.5	17.5	17.5	17.5	17.4	17.4	17.4	17	17	17	17	17	17	17	17	17	17	17
	-0.9	17	17.3	17.3	17.4	17.4	17.4	17.4	17.4	17.4	17.4	17	17	17	17	17	17	17	17	17	17	17
	-1	17	17.2	17.2	17.2	17.2	17.3	17.3	17.3	17.3	17.3	17	17	17	17	17	17	17	17	17	17	18

Figure 5.3. Heat map of the reduced model of the angle of repose simulation study for hybrid poplar.

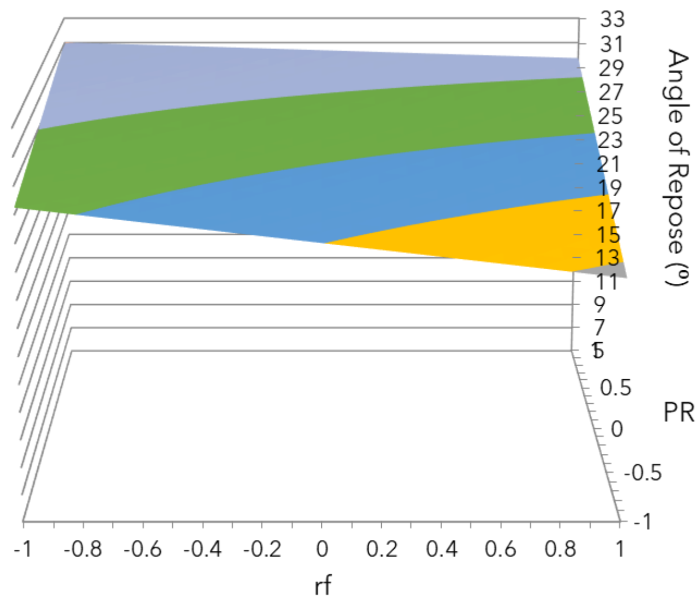

Figure 5.4. 3D correlation plot for the reduced model for switchgrass.

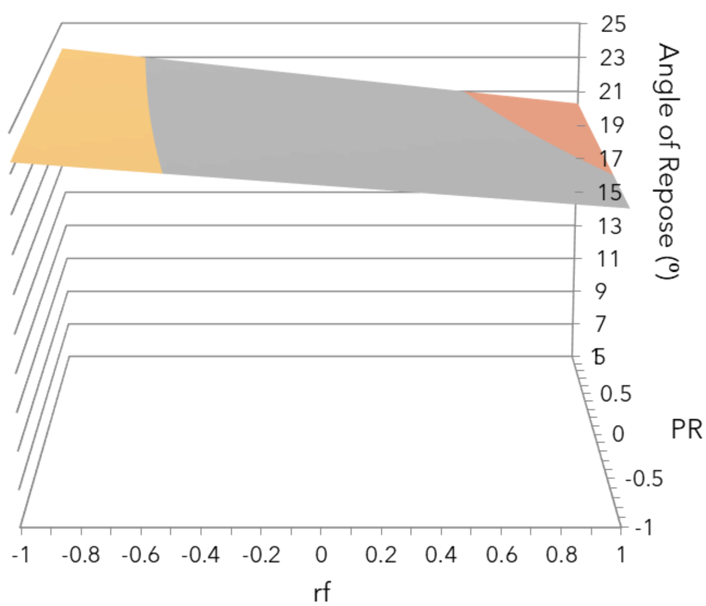

Figure 5.5. 3D correlation plot for the reduced model for loblolly pine.

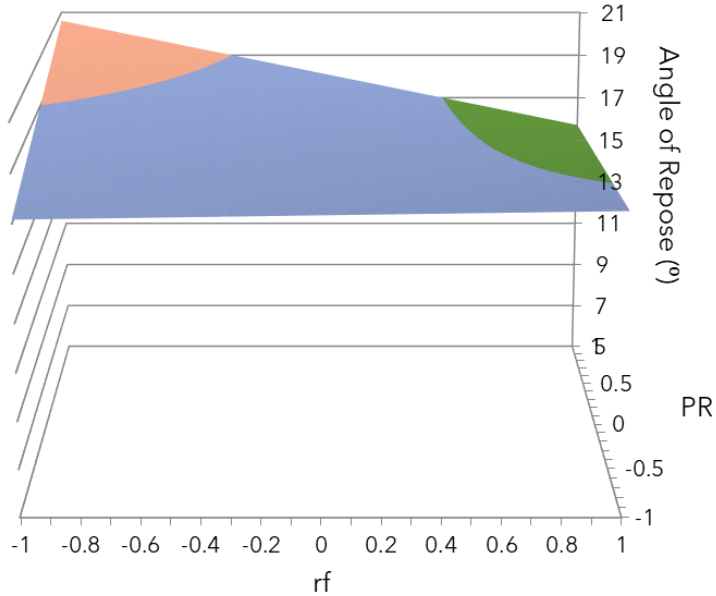

Figure 5.6. 3D correlation plot for the reduced model for hybrid poplar.

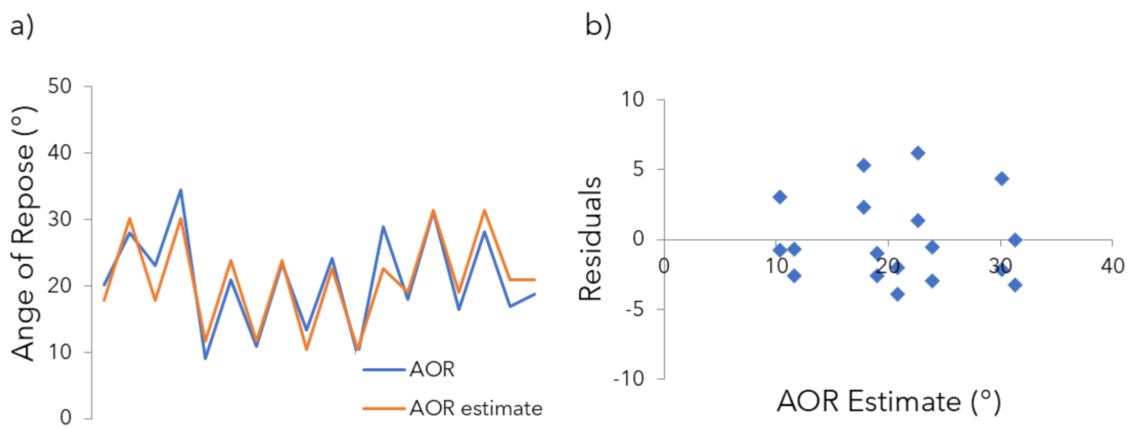

Figure 5.7. a) Angle of repose (AOR) values for switchgrass – actual vs. estimated using the reduced model, b) residuals vs. estimates plot.

formula. Additionally, we checked whether the average of the residuals is close to zero and if they follow a normal distribution by examining the p-value.

The residuals are symmetrically distributed, tending to cluster towards the middle of the plot and clustered around the lower digits of the y-axis. We see no trends of the residuals along the estimate range. Additionally, the p-value for the normality is 0.983, which is higher than the critical p-value (0.05).

Therefore, the residuals pass the normality check, and our reduced model has an elevated level of accuracy. We see similar normality observations for loblolly pine and hybrid poplar, shown in Figure 5.8 and Figure 5.9.

5.3.5. Information Criteria

Table 5.7 shows the information criteria for the switchgrass angle of repose study. Normal distribution best fits the switchgrass angle of repose as it shows the lowest values for all information criteria parameters.

Figure 5.10 shows the Q-Q plot for the angle of repose values of switchgrass. The Q-Q plots indicate that residuals fall along the middle of the line, with a higher deviation near the lower bounds, and therefore the normal distribution fits the switchgrass dataset well.

Table 5.8 shows the information criteria for the loblolly angle of repose study. We see that lognormal distribution best fits the loblolly angle of repose

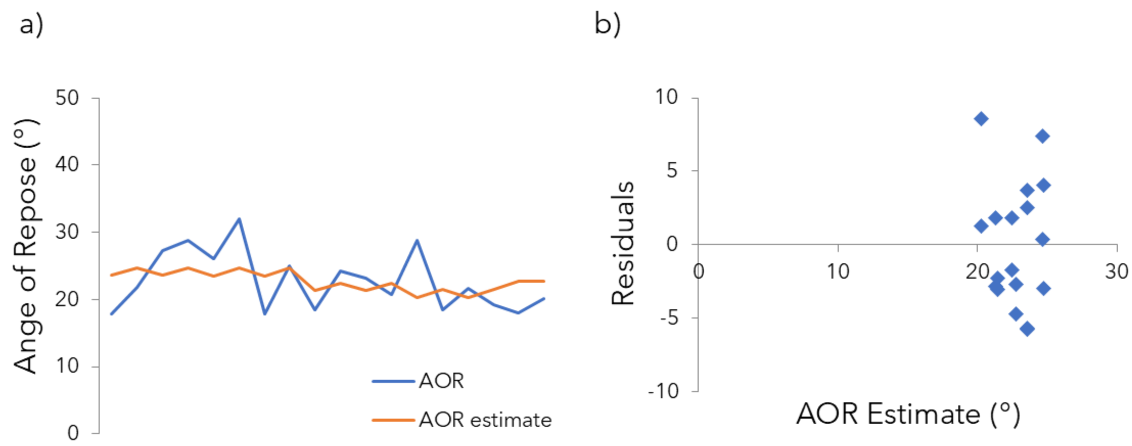

Figure 5.8. a) Angle of repose (AOR) values for loblolly pine – actual vs. estimated using the reduced model, b) residuals vs. estimates plot.

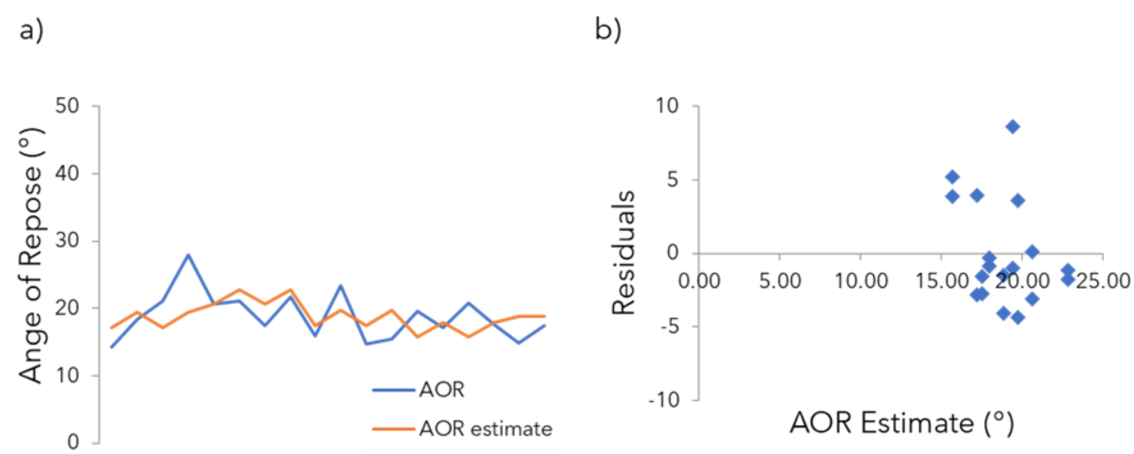

Figure 5.9. a) Angle of repose (AOR) values for hybrid poplar – actual vs. estimated using the reduced model, b) residuals vs. estimates plot.

Table 5.7. Information criteria for switchgrass simulation dataset.

Distribution	AIC	CAIC	BIC	ICOMP
Normal	**-46.9**	**-43.1**	**-45.1**	**-47.1**
Lognormal	-46.3	-42.6	-44.6	-46.7
Student t	-44.9	-39.2	-42.2	-47.1
Exponential	-41.7	-39.8	-40.8	-40.5
Gamma	-46.7	-42.9	-44.9	-47
Weibull	-46	-42.2	-44.2	-46.5

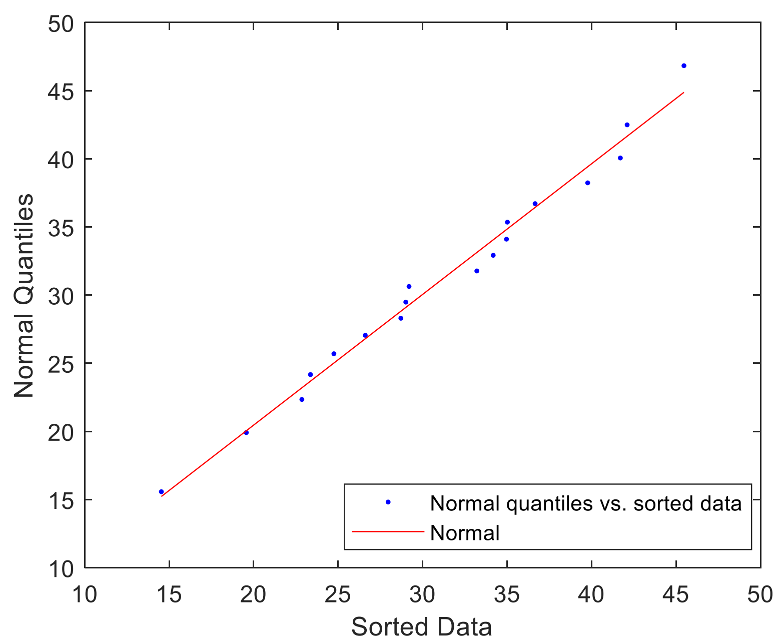

Figure 5.10. Q-Q plot for the switchgrass simulation dataset.

Table 5.8. Information criteria for loblolly pine simulation dataset.

Distribution	AIC	CAIC	BIC	ICOMP
Normal	61.3	65.0	63.0	58.4
Lognormal	**51.2**	**55.0**	**53.0**	**47.8**
Student t	63.3	68.9	65.9	58.4
Exponential	57.4	59.3	58.3	55.8
Gamma	53.9	57.7	55.7	50.7
Weibull	67.9	71.7	69.7	65.1

as it shows the lowest values for all information criteria parameters. This conclusion is supported by the Q-Q plot in Figure 5.11, which shows the residuals falling along the middle of the line, with a higher deviation near the lower bounds. Therefore, the lognormal distribution fits the loblolly pine dataset well.

Table 5.9 shows the information criteria for the loblolly angle of repose study. We see that lognormal distribution best fits the hybrid poplar angle of repose as it shows the lowest values for all information criteria parameters. This conclusion is supported by the Q-Q plot shown in Figure 5.12, which shows the residuals falling along the middle of the line, with a higher deviation near the lower bounds. Therefore, the lognormal distribution is suitable for the hybrid poplar.

5.4. Conclusions

In this study, we took a design of experiments approach to investigate the relative effects of select input parameters on the output of a discrete computational model for the hollow cylinder angle of repose study for different lignocellulosic biomass feedstock materials. We used a half-factorial design with two levels and five factors and determined the angle of repose values for flow models representing switchgrass, loblolly pine, and hybrid poplar. Next, we

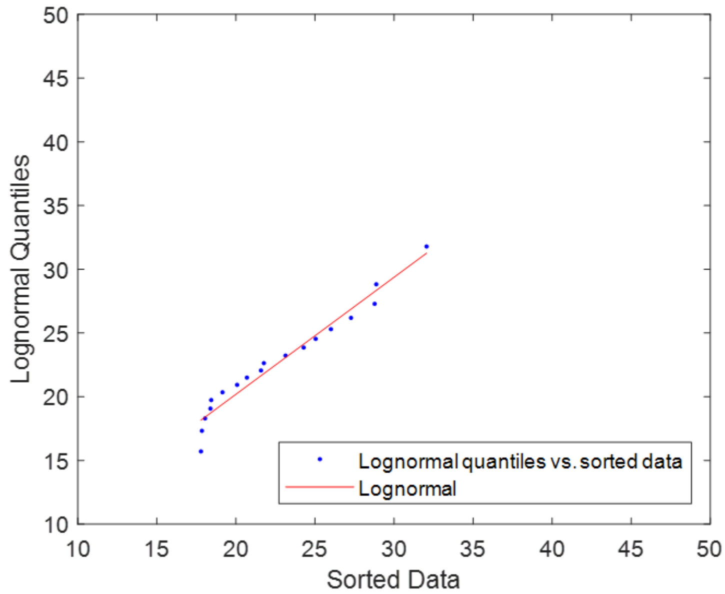

Figure 5.11. Q-Q plot for the loblolly pine simulation dataset.

Table 5.9. Information criteria for hybrid poplar simulation dataset.

Distribution	**AIC**	**CAIC**	**BIC**	**ICOMP**
Normal	52.4	56.2	54.2	49.6
Lognormal	**42.0**	**45.7**	**43.7**	**38.3**
Student t	54.4	60.1	57.1	49.5
Exponential	46.2	48.1	47.1	44.3
Gamma	45.3	49.1	47.1	41.9
Weibull	59.1	62.8	60.8	56.7

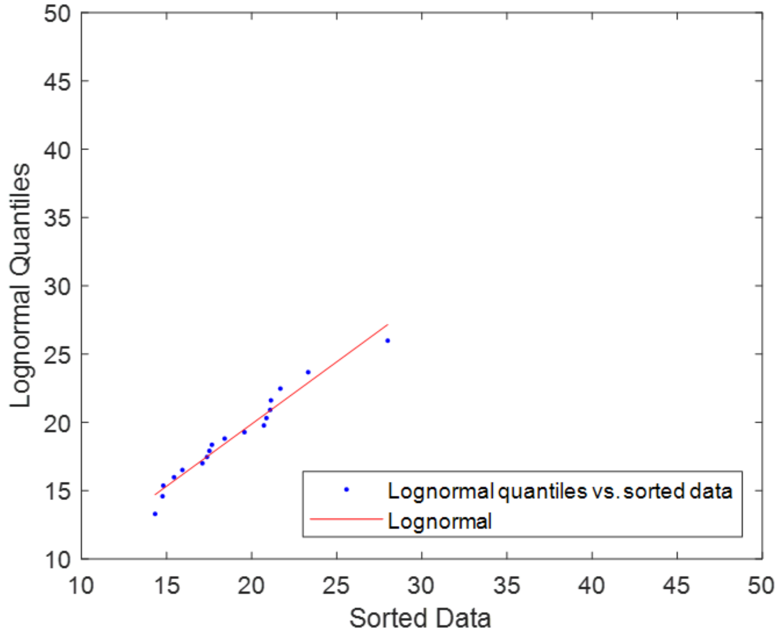

Figure 5.12. Q-Q plot for the hybrid poplar simulation dataset.

a multiple linear regression model on the angle of repose dataset and validated our choice of input parameters using regression statistics. We then identified Young's modulus, Poisson's ratio, and the coefficient of rolling friction as the most critical factors for the angle of repose and developed a reduced regression model to describe their relationship. We then conducted an optimization process to determine the model input parameters required to obtain the minimum value for the angle of repose. We checked the normality of the reduced model using residuals analysis to ensure the linear regression approach was suitable for our suitable model. Finally, we conducted a quantile modeling process using information criteria to determine the best-fitting distribution for the dataset obtained for the different lignocellulosic biomass materials. Overall, our results indicate that our statistical analysis process combining the design of experiments with classical and modern model selection process can be used to determine the level of influence of DEM model input parameters on model outputs and, therefore, build better models to capture the flow behavior of different biomass particulate assemblies computationally.

References

(1) Benvenuti, L.; Kloss, C.; Pirker, S. Identification of DEM simulation parameters by Artificial Neural Networks and bulk experiments. *Powder Technol.* **2016**, *291*, 456-465.

(2) Johnstone, M. W. Calibration of DEM models for granular materials using bulk physical tests. Ph.D., The University of Edinburgh, 2010.

(3) González-Montellano, C.; Ayuga, F.; Ooi, J. Y. Discrete element modelling of grain flow in a planar silo: influence of simulation parameters. *Granul. Matter* **2011**, *13* (2), 149-158.

(4) Nakashima, H.; Fujii, H.; Oida, A.; Momozu, M.; Kawase, Y.; Kanamori, H.; Aoki, S.; Yokoyama, T. Parametric analysis of lugged wheel performance for a lunar microrover by means of DEM. *J. Terramech.* **2007**, *44* (2), 153-162.

(5) Xu, Y.; Xu, C.; Zhou, Z.; Du, J.; Hu, D. 2D DEM simulation of particle mixing in rotating drum: A parametric study. *Particuology* **2010**, *8* (2), 141-149.

(6) Bozdogan, H.; Howe, J. A. Misspecified multivariate regression models using the genetic algorithm and information complexity as the fitness function. *Eur. J. Pure Appl. Math.* **2012**, *5* (2), 211-249.

(7) Marchelli, F.; Moliner, C.; Bosio, B.; Arato, E. A CFD-DEM sensitivity analysis: The case of a pseudo-2D spouted bed. *Powder Technol.* **2019**, *353*, 409-425.

(8) Wang, S.; Luo, K.; Fan, J. CFD-DEM coupled with thermochemical sub-models for biomass gasification: Validation and sensitivity analysis. *Chem. Eng. Sci.* **2020**, *217*, 115550.

(9) Wilkinson, S. K.; Turnbull, S. A.; Yan, Z.; Stitt, E. H.; Marigo, M. A parametric evaluation of powder flowability using a Freeman rheometer through statistical and sensitivity analysis: A discrete element method (DEM) study. *Comput. Chem. Eng.* **2017**, *97*, 161-174.

(10) Kartal Koc, E.; Bozdogan, H. Model selection in multivariate adaptive regression splines (MARS) using information complexity as the fitness function. *Mach. Learn.* **2015**, *101*, 35-58.

(11) Lin, T. H.; Dayton, C. M. Model selection information criteria for non-nested latent class models. *J. Educ. Behav. Stat.* **1997**, *22* (3), 249-264.

(12) Rogers, A.; Ierapetritou, M. G. Discrete element reduced-order modeling of dynamic particulate systems. *AIChE J.* **2014**, *60* (9), 3184-3194.

(13) Wang, B.; Martin, U.; Rapp, S. Discrete element modeling of the single-particle crushing test for ballast stones. *Comput Geotech* **2017**, *88*, 61-73. DOI: https://doi.org/10.1016/j.compgeo.2017.03.007.

(14) Bozdogan, H. Model selection and Akaike's information criterion (AIC): The general theory and its analytical extensions. *Psychometrika* **1987**, *52* (3), 345-370.
(15) Raykov, T.; Marcoulides, G. A. On desirability of parsimony in structural equation model selection. *Struct. Equ. Modeling* **1999**, *6* (3), 292-300.
(16) Bro, R.; Smilde, A. K. Principal component analysis. *Anal. Methods* **2014**, *6* (9), 2812-2831.
(17) Mac Nally, R.; Duncan, R. P.; Thomson, J. R.; Yen, J. D. L. Model selection using information criteria, but is the "best" model any good? *J. Appl. Ecol.* **2018**, *55* (3), 1441-1444.
(18) Bozdogan, H. Akaike's information criterion and recent developments in information complexity. *J. Math. Psychol.* **2000**, *44* (1), 62-91.
(19) Falk, C. F.; Muthukrishna, M. Parsimony in model selection: Tools for assessing fit propensity. *Psychol. Methods* **2021**.
(20) Akaike, H. A new look at the statistical model identification. *IEEE Trans. Autom. Control* **1974**, *19* (6), 716-723.
(21) Lumley, J. L.; Takeuchi, K. Application of central-limit theorems to turbulence and higher-order spectra. *J. Fluid Mech.* **1976**, *74* (3), 433-468.
(22) Schwarz, G. Estimating the dimension of a model. *Ann. Stat.* **1978**, 461-464.
(23) Bozdogan, H.; Ueno, M. A unified approach to information-theoretic and Bayesian model selection criteria. In *6th World Meeting of the International Society for Bayesian Analysis (ISBA)*, 2000, 1999.
(24) Bozdogan, H. *Statistical data mining and knowledge discovery*; CRC Press, 2003.
(25) Konishi, S.; Kitagawa, G. *Information criteria and statistical modeling*; Springer, 2008. DOI: https://doi.org/10.1007/978-0-387-71887-3.
(26) Kleijnen, J. P. C. An overview of the design and analysis of simulation experiments for sensitivity analysis. *Eur. J. Oper. Res.* **2005**, *164* (2), 287-300.
(27) Freireich, B.; Litster, J.; Wassgren, C. Using the discrete element method to predict collision-scale behavior: a sensitivity analysis. *Chem. Eng. Sci.* **2009**, *64* (15), 3407-3416.
(28) Kelton, W. D.; Barton, R. R. Experimental design for simulation. In *2003 Winter Simulation Conference*, 2003; IEEE: Vol. 1, pp 59-65.
(29) Barton, R. R. Designing simulation experiments. In *2013 Winter Simulations Conference (WSC)*, Washington D.C., 2013; IEEE: pp 342-353.
(30) Galvanin, F.; Barolo, M.; Bezzo, F.; Macchietto, S. A backoff strategy for model-based experiment design under parametric uncertainty. *AIChE J.* **2010**, *56* (8), 2088-2102.

(31) Giunta, A.; Wojtkiewicz, S.; Eldred, M. Overview of modern design of experiments methods for computational simulations. In *41st Aerospace Sciences Meeting and Exhibit*, 2003, 2003; p 649.
(32) Jankovic, A.; Chaudhary, G.; Goia, F. Designing the design of experiments (DOE)–An investigation on the influence of different factorial designs on the characterization of complex systems. *Energy Build.* **2021**, *250*, 111298.
(33) Al-Hashemi, H. M. B.; Al-Amoudi, O. S. B. A review on the angle of repose of granular materials. *Powder Technol.* **2018**, *330*, 397-417.

CHAPTER 6.

DISSERTATION CONCLUSIONS

AND RECOMMENDATIONS

6.1. Overall Conclusions

The overall objective of this dissertation research was to develop a fundamental understanding of the relationship between structural constituents of lignocellulosic biomass, i.e., cellulose, hemicellulose, and lignin, their, morphology, and the impact of the structure and morphology on their flow behavior. We carried out three different studies to achieve the objectives of this dissertation and reached the following conclusions.

1) We presented a comprehensive experimental investigation of three lignocellulosic biomass feedstock materials (switchgrass, loblolly pine, and hybrid poplar), examining the effect of variable proportions of cellulose, hemicellulose, and lignin on their flow behavior in Chapter 3. Our research shows that the magnitude of angle repose for switchgrass is higher than loblolly pine and hybrid poplar. In contrast, the shear strength value increases from switchgrass to loblolly pine to hybrid poplar. We conclude that the angle of repose and shear strength positively correlate with cellulose and hemicellulose and no significant correlation with lignin. Additionally, we conclude that the shear strength and angle of repose values are independent of the particle sizes of the feedstock.

2) We provide a combination of experimental morphological parameters and superquadric discrete element computational modeling techniques to capture the real lignocellulosic biomass morphology and flow behaviors in Chapter 4. The developed experimental method (involving dynamic particle analysis and error minimization) and computational models can reliably and accurately capture switchgrass, loblolly pine, and hybrid poplar materials morphologies. We conclude that the bulk density, pile diameter, and angle of repose from DEM simulations are validated by the results from geometrically identical physical experiments. Additionally, we conclude that the overall contact force between particles decreases with an increased aspect ratio until the contact force achieves a state beyond which the uniformity in force distribution becomes nearly constant and independent of the aspect ratio.
3) We demonstrate a design of an experiments-based statistical analysis process approach to investigate the relative effects of select input parameters on the output of a discrete computational model for a hollow cylinder angle of repose study in Chapter 5. We conclude that the relationship between the model input parameters (Young's modulus, Poisson's ratio, coefficient of static friction, coefficient of

rolling friction, and coefficient of restitution) and the response variable (angle of repose) can be fitted using a linear regression model. We also conclude that the regression model can be simplified by selecting the most critical input parameters, namely Young's modulus, Poisson's ratio, and the coefficient of rolling friction, and the minimum value of angle of repose for a particular feedstock material can be determined by optimizing the critical input parameters.

6.2. Contributions

The main contribution of this dissertation research is the development of an experimental and computational framework for quantitatively examining the effect of lignocellulosic biomass materials' structural composition and morphology on their flow properties. We built a comprehensive database of shear strength and angle of repose for different lignocellulosic biomass materials, covering herbaceous, softwood, and hardwood, as well as hardwood materials of different compositions. We also established and validated a method for realistically capturing irregularly shaped biomass particle morphologies and generating discrete element computational models using the morphological parameters. Finally, we provided a statistical analysis process combining both classical and modern statistical model evaluation techniques to determine the relative influence of DEM model input parameters on model outputs and develop simpler and more efficient models for determining important flow parameters.

6.3. Recommendations

The different studies presented in this dissertation provide highly relevant information and tools for understanding the fundamental relationship between lignocellulosic biomass structural composition, morphology, and flow behavior. However, specific research questions require more conclusive answers, and certain research gaps require further investigation. We will highlight these research gaps and opportunities in the interest of future researchers in this subject area.

Examining the microstructural composition of different lignocellulosic biomass materials

For our objective 1, we qualitatively and quantitatively determined the cellulose, hemicellulose, and lignin composition by means of structural analysis and thermogravimetric analysis. However, we need to explore the lignocellulose matrix at the fiber level and the chemical bonds between the principal constituents to make more informed decisions. We suggest examining biomass structural constituents using advanced technologies such as X-ray diffraction

(XRD), Fourier transform infrared spectroscopy (FTIR), and nuclear magnetic resonance (NMR) [1-5].

Capturing the particle surface texture of lignocellulosic biomass materials

For our objective 2, we presented an experimental pathway for accurately capturing particle shape and size distribution using dynamic image analysis and processing. However, particle surface texture is an essential component to completely describe the particle morphology [6], potentially affecting the interaction forces between the particles. Therefore, we need an experimental quantitative method for determining the particle surface conditions. We suggest conducting a surface texture analysis using techniques such as atomic force microscopy (AFM) [7]. This technique conducts the imaging by monitoring the position of a sharpened tip attached to a micro-cantilever as it scans over a sample surface [8]. The AFM provides three-dimensional surface visualization and measurement of the sample's nanomechanical properties [9, 10]. We believe that the AFM technique will provide a quantitative way of examining the surface texture expressed in terms of surface roughness parameters.

Additionally, The discrete element model developed in our research using the state-of-the-art superquadric particle model assumes the contacting particles to be completely smooth [11]. However, real biomass particles are highly textured, and the irregularities on the particle surface significantly influence their interlocking nature, frictional properties, and, ultimately, their macro-scale flow behavior [12]. Therefore, we need a new superquadric particle model that can capture the effect of the biomass particle's surface texture. We propose that the new contact model considers the surface roughness, measured using AFM or a similar surface analysis technique to calculate interaction forces between the particles.

Experimentally measuring lignocellulosic biomass material properties

For our objective 3, we conducted a design of experiments-based sensitivity analysis to determine the relative effects of different biomass morphological, material, and mechanical properties on the angle of repose. For this purpose, we used the values of input parameters, such as Young's modulus, Poisson's ratio, coefficient of restitution, coefficient of static friction, and coefficient of rolling friction, as described in the literature. However, to achieve a robust and accurate model applicable to diverse biomass materials, we recommend the use of experimentally determined values for each parameter for the material under test. For example, we can determine the interparticle coefficient of restitution of the beechwood sample materials using the double-pendulum-based experimental method developed by Wong et al. and utilized for restitution coefficient measurement by Ramírez-Gómez et al. [13, 14]. Similarly, we can determine the coefficient of rolling friction by using the contact eccentricity method [15]. This method assumes that the rolling friction of a non-spherical particle is equal to the ratio of the ensemble-averaged contact eccentricity (e) to the equivalent partial diameter (d_p) [16]. Therefore, the rolling friction can be found by determining the ensemble average of the contact eccentricity and projected diameter of particles using image analysis and post-processing.

References

(1) Xu, F.; Yu, J.; Tesso, T.; Dowell, F.; Wang, D. Qualitative and quantitative analysis of lignocellulosic biomass using infrared techniques: a mini-review. *Appl. Energy* **2013**, *104*, 801-809.

(2) Vu, H. P.; Nguyen, L. N.; Vu, M. T.; Johir, M. A. H.; McLaughlan, R.; Nghiem, L. D. A comprehensive review on the framework to valorise lignocellulosic biomass as biorefinery feedstocks. *Sci. Total Environ.* **2020**, *743*, 140630.

(3) Xu, F.; Shi, Y.-C.; Wang, D. X-ray scattering studies of lignocellulosic biomass: a review. *Carbohydr. Polym.* **2013**, *94* (2), 904-917.

(4) Samuel, R.; Pu, Y.; Foston, M.; Ragauskas, A. J. Solid-state NMR characterization of switchgrass cellulose after dilute acid pretreatment. *Biofuels* **2010**, *1* (1), 85-90.

(5) Lu, F.; Ralph, J. Solution-state NMR of lignocellulosic biomass. *J Biobased Mater Bioenergy* **2011**, *5* (2), 169-180.

(6) Tafesse, S.; Robison Fernlund, J. M.; Sun, W.; Bergholm, F. Evaluation of image analysis methods used for quantification of particle angularity. *Sedimentology* **2013**, *60* (4), 1100-1110.

(7) Tetard, L.; Passian, A.; Farahi, R. H.; Kalluri, U. C.; Davison, B. H.; Thundat, T. Spectroscopy and atomic force microscopy of biomass. *Ultramicroscopy* **2010**, *110* (6), 701-707.

(8) Otsubo, M.; O'Sullivan, C.; Hanley, K. J.; Sim, W. W. The influence of particle surface roughness on elastic stiffness and dynamic response. *Géotechnique* **2017**, *67* (5), 452-459.

(9) Giessibl, F. J. Advances in atomic force microscopy. *Rev. Mod. Phys.* **2003**, *75* (3), 949.

(10) Konopinski, D.; Hudziak, S.; Morgan, R.; Bull, P.; Kenyon, A. Investigation of quartz grain surface textures by atomic force microscopy for forensic analysis. *Forensic Sci. Int.* **2012**, *223* (1-3), 245-255.

(11) Ramírez-Aragón, C.; Ordieres-Meré, J.; Alba-Elías, F.; González-Marcos, A. Comparison of cohesive models in EDEM and LIGGGHTS for simulating powder compaction. *Materials* **2018**, *11* (11), 2341.

(12) Gryczka, U.; Migdal, W.; Chmielewska, D.; Antoniak, M.; Kaszuwara, W.; Jastrzebska, A.; Olszyna, A. Examination of changes in the morphology of lignocellulosic fibers treated with e-beam irradiation. *Radiat. Phys. Chem.* **2014**, *94*, 226-230.

(13) Wong, C. X.; Daniel, M. C.; Rongong, J. A. Energy dissipation prediction of particle dampers. *J. Sound Vibrat.* **2009**, *319* (1), 91-118. DOI: https://doi.org/10.1016/j.jsv.2008.06.027.

(14) Ramírez-Gómez, Á.; Gallego, E.; Fuentes, J. M.; González-Montellano, C.; Ayuga, F. Values for particle-scale properties of biomass briquettes made from agroforestry residues. *Particuology* **2014**, *12*, 100-106.
(15) Agarwal, A.; Tripathi, A.; Tripathi, A.; Kumar, V.; Chakrabarty, A.; Nag, S. Rolling friction measurement of slightly non-spherical particles using direct experiments and image analysis. *Granul. Matter* **2021**, *23* (3), 1-14.
(16) Wensrich, C. M.; Katterfeld, A.; Sugo, D. Characterisation of the effects of particle shape using a normalised contact eccentricity. *Granul. Matter* **2014**, *16* (3), 327-337.

VITA

Ekramul Haque Ehite was born in Mymensingh, Bangladesh, and grew up in Chittagong, Bangladesh. He passed the Secondary School Certificate (SSC) examination in June 2006 from the Chittagong Cantonment Public College, Chittagong, and passed the Higher Secondary Certificate (HSC) examination in September 2008 from the Chittagong Cantonment Public College, Chittagong. He then entered the Bangladesh University of Engineering and Technology (BUET) in Dhaka, Bangladesh, and received a Bachelor of Science in Mechanical Engineering degree in October 2014. He entered the Michigan Technological University in September 2014 and completed a Master of Science in Mechanical Engineering degree in April 2016. He then joined the Tennessee Technological University in August 2016 and received a Master of Science in Mechanical Engineering degree in May 2018. He entered the University of Tennessee Knoxville in Aug 2018 to pursue a Ph.D. in Biosystems Engineering degree with a concentration in Energy Science and Engineering. His research interests include the transportation and conversion of lignocellulosic biomass and advanced computational modeling techniques. Ekramul is a member of the American Society of Agricultural and Biological Engineers (ASABE) and the American Institute of Chemical Engineers (AIChE).